

SILICON MICROMACHINED RESONANT ACCELEROMETER WITH CMOS INTERFACE CIRCUITS

HE LIN

(B. Sc. Southeast Univ. 1999)
(M. Eng. Southeast Univ. 2002)

**A THESIS SUBMITTED
FOR THE DEGREE OF DOCTOR OF
PHILOSOPHY**

**DEPARTMENT OF ELECTRICAL AND
COMPUTER ENGINEERING**

NATIONAL UNIVERSITY OF SINGAPORE

2008

Acknowledgement

I would like to thank Professor Yong Ping Xu for his continuous support, guidance and encouragement and for giving me the independence to follow my ideas wherever they led. His constant but constructive criticisms were keys in the successful outcome of this study.

I would like to thank Professor Moorthi Palaniapan for listening to my ideas and providing me with critical feedback. His expertise in MEMS actuators and sensors is indispensable to the success of this research. I would like to thank Professor Libin Yao and Professor Chunhuat Heng for helping me in the layout and phase-noise measurement.

I would also like to thank Professor Wai-Kin Wang for the vacuum setup.

Throughout my PHD study, I work closely with Jiangzhong Chen. We did designs together, shared the know-hows together, and solved the problems for each other. I would like to especially thank him for his friendship and wish him all the best.

I received tremendous help from Mrs. Huanqun Zheng and Mr. Seow Miang Teo, who helped me to install the design tools, and to setup the measurement environment. I extend special thanks to them all.

I thank my friends and colleagues in the Signal processing and VLSI Lab: Jianghong Yu, Yajun Yu, Chunzhu Yang, Xinbo Qian, Jiang Xie, Zhenjiang Su, Rui Yu, Licun Shao, Kine Lynn, Leung Chee, Xiaohua Tian, Ying Wei, Zhenglin Yang, Heng Yu, Wenjuan Zhang, Xiaodan Zou, Xiaolei Chen, Junle Pan and others, for their help in my work and moral support.

I am very grateful to my parents and my brother for their love, support, encouragement,

and understanding. I fully realize how lucky I am to born into such an amazing family.

This research was funded by the National university of Singapore under project R-263-000-289-112.

Table of Contents

Acknowledgement	i
Table of Contents	iii
Summary	vi
List of Tables.....	vii
List of Figures	viii
Chapter 1. Introduction	1
1.1 Background.....	1
1.1.1 MEMS reference oscillator	1
1.1.2 MEMS resonant accelerometer	2
1.2 Motivation	3
1.2.1 Problem statement.....	3
1.2.2 Objective and overview	7
Chapter 2. Review of silicon resonant accelerometer.....	11
2.1 Accelerometer Applications and Performance Expectations.....	11
2.1.1 Inertial navigation system (INS).....	12
2.1.2 GPS/INS	12
2.1.3 Automotive	13
2.2 Literature review on silicon resonant accelerometer	13
Chapter 3 Silicon resonant accelerometer.....	20
3.1 Sense principle.....	20
3.2 Mechanical analysis of resonant beam	22

3.3	Mechanical leverage-force amplifier.....	25
3.4	Electrostatic Actuation.....	26
3.5	Damping	31
3.6	Equivalent electrical network	33
3.7	Parasitic electrical coupling.....	34
3.8	Fabrication process	37
3.9	Our resonant accelerometer design.....	39
Chapter 4 Resonator nonlinearities		44
4.1	Origin of nonlinearities.....	44
4.1.1	Geometrical.....	44
4.1.2	Nonlinear Young's Modulus.....	48
4.1.3	Capacitive transduction.....	49
4.2	Nonlinear forced vibration.....	50
Chapter 5 MEMS oscillator and phase noise theory		54
5.1	MEMS oscillator and automatic amplitude control.....	54
5.2	Existing phase noise theory	57
5.2.1	Phase noise basics.....	57
5.2.2	Linear time-invariant model	58
5.2.3	Linear time-variant model	61
5.2.4	Limitation of LTV model.....	65
5.3	State-space theory	65
5.3.1	Unperturbed oscillator trajectory in state-space	66
5.3.2	Velocity observation noise and gain variation.....	68

5.3.3	Orbital and phase perturbation	69
5.3.4	Cycling speed correction factor	71
5.3.5	Amplitude limiting-Automatic amplitude control (AAC)	73
5.3.6	Phase noise discussion	77
5.4	Numerical simulation	78
Chapter 6	Circuit design	84
6.1	System overview	84
6.2	Low noise capacitive sense interface	86
6.3	Offset-free differentiator	89
6.4	Linear VGA and buffer	92
6.5	CHS peak detector and error amplifier	93
6.6	Chip floorplan and microphotograph	94
Chapter 7	Experimental result	96
7.1	MEMS oscillator	96
7.2	SOI resonant accelerometer	100
Chapter 8	Conclusions and future work	105
8.1	Conclusion	105
8.2	Future work	106
References	108
Appendix	118

Summary

This research focused on the design of a low noise, high stability silicon resonant accelerometer. It covered a range from the theory to the system implementation. First, the mechanisms that give rise to the unexpected phase noise and bias instability were explored with a theoretical study. In this theoretical study, state-space theory is applied to an ideal nonlinear oscillator with an ideal position sensor, an ideal velocity sensor, and an automatic amplitude control (AAC) loop. A quantitative phase noise model is thus derived. It soundly proved that despite of the nonlinearities in a MEMS resonator, the resultant phase noise is still governed by a linear transfer function to the noise sources in the oscillator loop and amplitude control loop.

Guided by the derive model, a fully-differential MEMS oscillator circuit was designed for SOI resonant accelerometer. A differential sense resonator is proposed to facilitate fully-differential circuit topology and improves the SNR under a 3.3-V supply. The oscillator circuit consisted of an oscillation loop and a low noise automatic amplitude control (AAC) loop. The noise inside the oscillation loop was kept minimum by a low-noise capacitive sense interface. The AAC loop contained a high-order loop filter and a novel chopper stabilized rectifier to remove the 1/f noise, and to minimize the phase noise caused by the noise aliasing. The complete resonant accelerometer operates under a 3.3-V supply and achieves 140-Hz/g scaling factor, $20 \mu\text{g}/\sqrt{\text{Hz}}$ resolution and $4 \mu\text{g}$ bias stability, which was the state of the art. The readout circuit draws 7-mA under 3.3-V supply.

List of Tables

4.1 Nonlinear Young's modulus for single-crystal silicon	50
5.1 Parameters for the simulation setup	79
7.1 Parameters of the sense resonator	97
7.2 Comparison of this work with previous capacitive MEMS accelerometer....	104
7.3 Comparison of this work with previous silicon resonant accelerometer	104

List of Figures

1.1 Illustration of phase noise in a nonlinear MEMS oscillator	6
3.1 Schematic diagram of a typical differential resonant accelerometer	22
3.2 Beam model used for vibration analysis	23
3.3 Illustration of a mechanical leverage	26
3.4 Electrostatic actuation	27
3.5 (a) Comb drive actuator and (b) parallel plate actuator	29
3.6 Illustration of (a) Couette flow damping and (b) Squeeze film damping	32
3.7 Transformation of a MEMS resonator to an equivalent RLC model	34
3.8 Illustration of parasitic electrical coupling paths in a MEMS resonator built from SOI substrate	35
3.9 Illustration of the frequency response of a MEMS resonator (a) without parasitic electrical coupling and (b) with parasitic electrical coupling	36
3.10 SOI process flow	38
3.11 Schematic diagram of the resonant accelerometer based on SOIMUMPs process	40
3.12 Microphotograph of a mechanical leverage in the resonant accelerometer	40
3.13 (a) Double-ended tuning fork for single-ended operation and (b) modified structure for fully-differential operation	42
3.14 Measured sense resonator frequency response (a) at 3.3 V polarization voltage and (b) at 25 V polarization voltage	44

4.1 Geometrical effect that leads to the nonlinearity in the clamped-clamped beam resonator.....	46
4.2 Spring softening due to change in the cross section area in the bulk acoustic wave (BAW) resonator	49
4.3 The amplitude-frequency response of (a) a linear resonator; (b) a nonlinear resonator that has a negative frequency shift; (c) a nonlinear resonator that has a positive frequency shift; (d) a nonlinear resonator excited below and beyond the bifurcation points.....	54
5.1 Schematic diagram of direct feedback MEMS oscillator	57
5.2 Schematic diagram of MEMS oscillator with AAC loop and gain control performed on the sense amplifier.....	58
5.3 Oscillator structure with fixed gain sense amplifier and AAC performed on a separate linear VGA.....	59
5.4 A linear oscillator system.....	62
5.5 LC oscillator showing charge injection	63
5.6 Impulse response of LC oscillator	64
5.7 Waveform and ISF for a LC oscillator	65
5.8 The equivalent block diagram of the LTV model	66
5.9 Noise folding due to ISF decomposition.....	66
5.10 Unperturbed oscillation trajectory $y_0(t)$ and perturbation decomposition	69
5.11 Macro model of second order nonlinear oscillator with noise in the observed velocity and feedback gain. Inside the dash box is the macro model of nonlinear resonator	70

5.12 Illustration of $\Gamma(y)$, $H(y)$, $\dot{x}\Gamma(y)$ and $\dot{x}H(y)$	72
5.13 Equivalent models of a perturbed free running nonlinear oscillator described by Equation 5.18.....	74
5.14 (a) Nonlinear MEMS oscillator with ideal position and velocity sensor and AAC loop; and (b) its equivalent linear model	76
5.15 Amplitude-frequency responses of resonator 1 (black) and resonator 2 (blue) in Table I	80
5.16 the state-space trajectories of the oscillator built from resonator 1, resonator 2 and an ideal linear resonator	81
5.17 Simulated two-tone spectrum sidebands for resonator 1 and resonator 2 ..	82
5.18 Simulated phase noise sideband versus LTI model and State-space model.....	83
6.1 Block diagram of the proposed readout circuit with automatic amplitude control.....	85
6.2 Block diagram of the proposed readout circuit with automatic amplitude control.....	85
6.3 Simplified schematic of fast-settling opamp with feedforward path	88
6.4 (a) Schematic of offset-free differentiator and (b) its associated clock diagram (FBND is delayed version of FBN and FBNDD is delayed version of FBND).....	89
6.5 Schematic diagram of VGA with transimpedance amplifier as the output buffer.....	91
6.6 Chopper stabilized peak detector and error amplifier.....	93

6.7 Chip floorplan.....	94
6.8 Chip microphotograph.....	95
7.1 Microphotograph of CMOS readout circuit chip and SOI resonator interconnected	97
7.2 The oscillator phase noise deduced from the measured PLL phase noise ...	98
7.3 A sample of measured frequency at PLL output versus elapsed time and its compensated result.....	99
7.4 Measured Allan Variance	100
7.5 system block diagram of the SOI resonant accelerometer.....	101
7.6 Microphotograph of the interconnected CMOS readout circuit chip and SOI resonant accelerometer	101
7.7 The measured Allan variance of the resonant accelerometer	102
7.8 Static acceleration testing result.....	103

Chapter 1. Introduction

1.1 Background

1.1.1 MEMS reference oscillator

Oscillators are widely used in modern communication systems, including voltage-controlled oscillators and timing reference (or clock). A timing reference is almost a must for every practical electronic system. Currently, the timing references for commercial products are dominantly provided by crystal oscillators, which have a market volume exceeding 4 billion dollars a year. Although a crystal oscillator is able to provide stable and clean oscillation, it is not compatible with any mainstream IC process. The timing reference is thus the bottleneck for a more compact and cheaper system. Additionally, crystal oscillators are relatively more expensive and dissipate significant power in portable systems.

The primary concern of a timing reference is its spectrum cleanness. The spectrum cleanness is the defining factor for the fidelity of a communication system, which determines the maximum bit rate and the minimum power consumption. The cleanness of oscillation is usually characterized by its phase noise, which is defined by the ratio of noise to carrier power at certain frequency offset. Phase Noise near the carrier is particularly important in communication systems with narrow channel spacing. In fact, the allowable channel spacings are frequently constrained by the amount of the phase noise.

Oscillators based on high quality factor resonators are well-known for their ability to produce a stable, low-noise output frequency. An overwhelmingly high quality factor can be achieved in a MEMS resonator, from 10, 000s to 100, 000s, compared with only 1000s in a crystal resonator. This property makes MEMS oscillators attractive as alternative timing references in the near future. The drawbacks of crystal oscillators could also be avoided by MEMS oscillators, as it has the potential to be fully-integrated with other building blocks into a single chip and the MEMS resonator itself consumes negligible power.

Startups such as Discera, and SiTime Corporation are manufacturing silicon MEMS oscillators. The first products from these two companies were two-chip solutions with limited phase noise performance, thus were limited to the low-end applications in Notebook PCs, digital cameras, DVD players, and other portable consumer electronic devices. Cell phones are also likely to witness the penetration of MEMS oscillators, as long as the next generation MEMS oscillators satisfy the tough phase noise specifications.

1.1.2 MEMS resonant accelerometer

The same properties mentioned above also make MEMS oscillators attractive in the sensing application. They are used in sensors such as MEMS vibratory gyroscopes, where an oscillation is established to produce a Coriolis acceleration, and resonant sensors, where the value of the frequency itself is the sensor output. Resonant sensors are superior to other type of sensors in a

number of aspects. Firstly, the phase noise of the oscillation output can be made very small [1], due to the high quality factor achievable in the sense resonator. Secondly, the quasi-digital nature of the output signal allows the sensor to easily interface digital systems. Thirdly, large input is allowed because the sensing element is generally a vibrating beam under an axial load, giving the sensor a very wide dynamic range [2].

Generally speaking, resonant sensing techniques are used when precision is the primary concern in the sensor application. Taking inertial navigation as an example, it requires accelerometers with extremely high precision at dc and low frequencies, as the positioning error is a double integral of the acceleration measurement error. In such applications, quartz resonant accelerometers, which are capable of detecting the tidal gravitational pull of the moon (10s of ng) [3], are frequently used [4].

Combining the powerful resonant sensing technique with micromachining could result in a high performance alternative for the expensive and bulky quartz resonant accelerometer but with much smaller size and lower cost.

1.2 Motivation

1.2.1 Problem statement

As mentioned in the previous section, to be used as timing references, the

MEMS oscillators have to produce output signal with very low phase noise. Furthermore, to be used in resonant accelerometers for navigation application, the MEMS oscillators need not only to be low noise, but also to have low bias stability. Bias stability refers to the bias (offset) change during a certain period. Poor bias change can be caused by environmental factors such as temperature or by random factors such as $1/f$ noise. Since the temperature effect can be compensated in a number of ways, the ultimate precision of accelerometer is determined by the random bias change, such as $1/f$ noise in the frequency reading, or $1/f^3$ phase noise. Therefore, both the MEMS oscillators for timing reference application and for sensing application need to suppress the $1/f^3$ phase noise in the close-in region.

At the first glance, it looks that MEMS oscillators should be able to achieve extremely low phase noise due to the extremely high quality factor achievable with the MEMS resonators. In practice, however, a MEMS oscillator always exhibits phase noise much worse than expected. A lot of experimental works have been done to find out the clues of this unexpected phase noise generation. T. A. Roessig [5] suggested that the nonlinearities in the mechanical component caused the $1/f^3$ noise through $1/f$ noise aliasing. S. Lee and C. T.-C. Nguyen [6] claimed that neither the $1/f$ noise in the sustaining circuitry nor the noise aliasing mechanism should be responsible for the measured $1/f^3$ phase noise. Instead, they speculated a link between the Duffing behavior and the unexpected phase noise and hence suggested that the oscillation amplitude should not exceed the Duffing bifurcation point. However, this link hasn't been soundly proven yet.

Nevertheless, all the works highlighted a concrete link between the undesirable phase noise with the nonlinearities.

Although there are ways to cancel the nonlinearities in a MEMS resonator, either through mechanical compensation, like folded suspension [7], or through nonlinear electrostatic stiffness [8], both of them work well only for low frequency resonators with natural frequency below hundreds of kHz. For MEMS resonators with higher natural frequencies, their mechanical stiffness are so high that the cancellation strategies mentioned above are no longer effective. Resonant accelerometers, although have a natural frequency around hundreds of kHz, are not applicable to these cancellation strategies either, as the same mechanism that causes nonlinearity is employed to cause the frequency shift under applied acceleration [2].

The constant scaling of the feature length in the CMOS technology and the resulting scaling down of supply voltage makes this nonlinearity problem even worse. Under a reduced polarization voltage, the output signal strength is compromised. To maintain the same signal-noise-ratio (SNR), a large oscillation-amplitude is preferred, which in turn increases the resonator nonlinearity and the $1/f^3$ phase noise.

Fortunately, the nonlinearities will reduce as the oscillation amplitude decreases. It is therefore a common practice to introduce automatic amplitude control (AAC) to prevent a resonator from entering strong nonlinear region [5, 6]. The reduction of oscillation amplitude, however, will cause the linear phase noise to increase. A trade-off has to be made to reach optimum phase noise at specific

frequency offset, as shown in Fig.1. It is therefore desirable to maximize the oscillation amplitude without causing the nonlinear phase noise to dominate. However, there is a widely held belief that the maximum allowable oscillation amplitude is limited by the Duffing bifurcation point, otherwise a chaotic behavior will be triggered which abruptly deteriorates the phase noise [6]. Due to the high quality factor, the bifurcation limit of a MEMS resonator is extremely small [10], far smaller than the intrinsic material limit, which seems to doom the future of MEMS reference oscillator. It is thus crucial to understand the details of the interaction between the various noise sources and the nonlinearities in a MEMS oscillator and establish a reliable phase noise model for nonlinear MEMS oscillator so as to guide a low noise design.

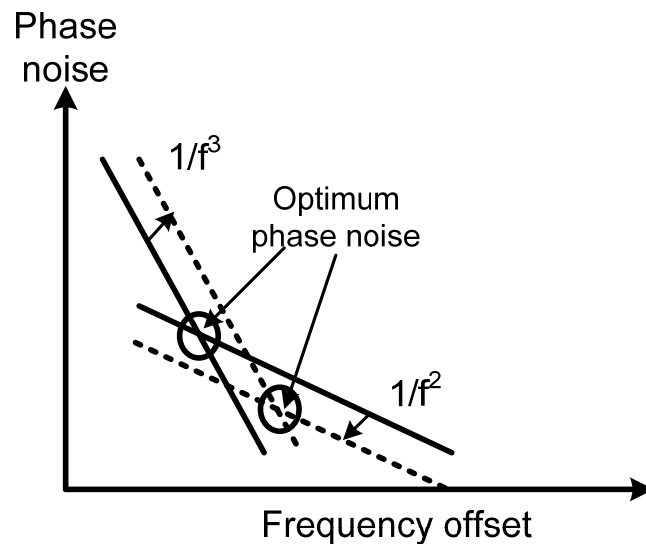


Figure 1.1 Illustration of phase noise in a nonlinear MEMS oscillator, the dotted line shows the changes of $1/f^3$ and $1/f^2$ phase noise at an increased amplitude.

However, the well-known linear time variant (LTV) model, which is widely used to analyze nonlinear electronic oscillators, fails to predict the phase noise in a nonlinear MEMS oscillator. In the LTV model, the oscillation frequency is explicitly assumed to be insensitive to the oscillation amplitude, which is in conflict with the A-S effect. Therefore, the phase noise mechanism in nonlinear MEMS oscillators needs to be studied with a different approach. It poses a challenge since a nonlinear oscillator with AAC loop is a complicated dynamic system which contains nonlinear building blocks such as amplitude detector, variable gain amplifier, and especially a nonlinear resonator. This prevents any ordinary linear analysis. To the author's knowledge, a reliable quantitative phase noise model for a nonlinear mechanical oscillator has not been published yet.

From the implementation point of view, low noise circuit level solutions need to be explored in both the oscillation loop and the AAC loop. The noise inside the AAC loop requires specific attention, as any additive noise introduced in this loop will appear as a noise in the oscillation amplitude and cause an extra phase noise through the A-S effect. The low noise design of the nonlinear building blocks in the AAC loop, such as amplitude detectors or rectifiers needs to be explored.

1.2.2 Objective and overview

This research aimed to suppress the $1/f^3$ phase noise and the bias stability caused by the nonlinear effect in the MEMS oscillators. Unlike many other colleagues in the area of MEMS oscillator, this work spent little effort on the

resonator design to minimize its nonlinearity, instead, it focused mainly on the system level solutions and circuit-level implementations to directly suppress the $1/f^3$ phase noise caused by nonlinearity.

The phase noise in a nonlinear MEMS oscillator employing automatic amplitude control is analyzed based on a state-space theory. From this analysis, a linear deterministic model was derived that quantitatively relates various noise sources to the resultant phase noise through the nonlinear terms.

With the guide from the linear deterministic model, a robust AAC loop structure for nonlinear MEMS oscillators is used for better temperature stability and control of amplitude noise. A prototype low-noise low-drift MEMS oscillator with an integrated self-oscillation circuitry was presented in this research. This circuitry features a low-noise switched-cap capacitive sense front-end, a novel low-noise switched-cap differentiator, a linear variable-gain amplifier, a high-efficiency trans-impedance buffer, a novel chopped rectifier, and an off-chip AAC loop filter. A prototype resonant accelerometer achieving $4\text{-}\mu\text{g}$ bias stability and $20\text{-}\mu\text{g}/\sqrt{\text{Hz}}$ resolution is presented as well.

The rest of the thesis is organized as follows:

In chapter 2, an overview of resonant accelerometers will be presented. A brief description of accelerometer applications and their respective performance requirement is followed by a review of silicon resonant accelerometer as a possible low-cost high performance solution for high end application.

Chapter 3 describes the operation principle and the design consideration of the silicon MEMS resonant accelerometer. In this chapter, the sensing

mechanism, force amplification, common-mode rejection, temperature effect, actuation mechanism, and readout principle are covered to give the reader an overview picture of MEMS resonant accelerometer.

In Chapter 4, the fundamentals of nonlinear resonator are introduced. The dynamic behavior of a nonlinear resonator is described by a general nonlinear mass-damper-spring model and its amplitude-frequency response. The amplitude-stiffening effect as well as the Duffing bifurcation point is quantitatively studied.

Chapter 5 reviews the previous works on MEMS oscillator structures and proposes a robust AAC loop structure for nonlinear MEMS oscillators for better temperature stability and control of amplitude noise. It was followed by the analysis of the phase noise in a nonlinear MEMS oscillator. Two of the widely recognized phase noise models, the linear time invariant (LTI) model and the linear time variant (LTV) model, are reviewed with their limitations on nonlinear MEMS oscillator examined. After that, a state-space analysis is performed on the nonlinear oscillator with the proposed AAC loop. A linear deterministic model is derived to quantitatively predict the phase noise. Low noise oscillator design guidelines are also developed in this chapter. Numerical simulation results are given to verify the model's linear deterministic property and to compare the simulated phase noise power spectrum density with the model prediction.

Chapter 6 discusses the implementation of the oscillator system, including the oscillator loop and the AAC loop. The capacitive sense interface makes extensive use of correlated-double-sampling to remove the opamp offset, the

charge injection and the kT/C noise. High speed switched-capacitor circuit design techniques are intentionally included to minimize the power consumption. In the AAC loop, a novel chopping technique is applied to the full-wave rectifier to chop away the $1/f$ noise component inside an ordinary rectifier.

Chapter 7 presents experimental results from the prototyping oscillator and the resonant accelerometer developed during the course of this research. A resonant accelerometer with $4\mu\text{g}$ bias stability and $20\mu\text{g}/\sqrt{\text{Hz}}$ noise floor is achieved.

Chapter 8 concludes the thesis and describes the future work.

Chapter 2. Review of silicon resonant accelerometer

In the following section, an overview of resonant accelerometers will be presented. A brief description of accelerometer applications and their respective performance requirement is followed by a review of silicon resonant accelerometer as a possible low-cost high performance solution for high end application.

2.1 Accelerometer Applications and Performance Expectations

Accelerometers can be used in any application that requires the measurement of acceleration. Since micromachined accelerometers are used in a wide range of applications, their required specifications are also application dependent and cover a rather broad spectrum. For instance, for microgravity measurements, a full-scale input range of ± 0.1 g and a resolution of less than $1\mu\text{g}$ in a frequency range from dc to 1 Hz are typical specifications. For navigation application where the accelerometer output needs to be double integrated to calculate the position information, the systematic accuracy is extremely sensitive to the dc and low frequency error in the measured acceleration. Therefore, in such an application, parameters like offset, long term bias stability, and scale factor stability are of primary concern.

Summarized below are a few well established applications and their

associated performance expectations.

2.1.1 Inertial navigation system (INS)

Probably the most widely recognized accelerometer application is inertial navigation where accelerometers and gyroscopes are used to retrieve position information. Gyroscopes give the information of the orientation while a triad of accelerometers measures the acceleration vector. Performance requirements for accelerometers in these applications are very demanding and depend on systematic accuracy and the length of time over which the inertial sensor outputs are integrated. Tactical grade inertial navigation typically requires accelerometer resolution and drift to be below $100\mu\text{g}$ while strategic grade inertial navigation requires accelerometers with an order of magnitude or better resolution and drift. [11]

2.1.2 GPS/INS

The requirements for inertial navigation can be considerably relaxed with the aid of GPS. GPS provides periodic position information which not only shortens the required integration interval in an inertial navigation system but also provide information useful for characterizing and correcting errors in the inertial sensors.

Tactical grade GPS/INS anticipate GPS signal jamming and hence the position is mainly determined by INS. In these cases, accelerometers with 0.1-

1mg resolution are required. The bandwidth required for these sensors is usually application dependent but is generally in the 10 to 100-Hz range. [11]

2.1.3 Automotive

Automotive applications are diverse ranging from demanding GPS-assisted INS to crude collision detection in the event of a accident. Automotive GPS assisted inertial navigation and the associated accelerometer performance are similar to tactical grade GPS/INS, which is 0.1-1mg resolution with a bandwidth in the 10 to 100Hz range. On the contrary, accelerometers used in air bags require a quick response and hence a bandwidth above 400Hz, but the resolution can be greatly relaxed. [11]

2.2 Literature review on silicon resonant accelerometer

MEMS accelerometers, or silicon micromachined accelerometers, are one of the most important types of silicon-based sensors. They alone have the second largest market share after pressure sensors. In the last 20years, they have gradually replaced the conventional accelerometers in automotive and consumer application due to the low cost achieved through high-volume manufacturing, automated assembly and test methods and the relative ease of monolithic integration of CMOS electronics. They are used in automotive applications, such as safety systems, air bags, and electronic suspensions; in consumer applications, such as platform stabilization in camcorders, digital

camera, virtual reality, and sport equipment; in industrial applications, such as robotics and vibration monitoring.

Despite the success of MEMS accelerometer in automatic and consumer applications, until very recently, the demands in high-end applications like aerospace and inertial navigation were still satisfied by the conventional bulky (and often expensive) accelerometers because of the demanding requirements. Due to the progress in the sensor fabrication and the interface circuit design, the performance of MEMS accelerometer keeps improving and is expected to step into traditional inertial navigation applications and emerging applications.

In the past decade, though different detection mechanisms have been proposed, MEMS accelerometer development has been dominated by capacitive sensing [12-14], in which the acceleration is measured by the capacitance change, due to its good dc response, low temperature sensitivity [15]. However, capacitive accelerometer suffers from uncertain drift [16] in the presence of radiation, preventing them from the applications in harsh environment such as space exploration. Compared with capacitive MEMS accelerometer, resonant accelerometer is radiation resistant [17] as it measures the frequency shift of the resonant beams. Furthermore, the resonant beams are axially loaded during operation, which allow large input and wide dynamic range [2]. Historically, quartz resonant accelerometer is favored in high-precision, navigation quality sensors [3]. It is capable of detecting the tidal gravitational pull of the moon (10s of ng) [4]. However, quartz micromachining requires specific fabrication process which does not integrate well with IC process.

Combining the powerful resonant sensing technique with micromachining could result in a high performance alternative for the expensive and bulky quartz resonant accelerometer with only a size and cost comparable to a low-end MEMS capacitive accelerometer. The advantages of the silicon resonant accelerometer over conventional silicon micro accelerometer can be summarized below

1. The frequency output can be read directly to the digital interface. The need for analog-to-digital conversion is thus eliminated, removing a major source of error and greatly reducing the system cost.
2. Force rebalancing feedback is avoided, along with the extra error introduced in the feedback loop.
3. The full-scale range is greatly extended by the open loop operation due to the super strength of silicon.
4. The silicon wafer material has most impurities controlled to less than 0.1 ppb, in order to control the electronic properties of silicon. The same pure single crystal silicon used by the electronics industry also has extremely well defined and stable mechanical properties. Since the temperature coefficient of sensitivity (scale factor) is inherent in the material property, it is no doubt that it is constant and has no deviation.
5. The frequency output has a build-in self-test feature.

These features make the silicon resonant accelerometer a promising low-cost solution for high-end applications, such as aerospace and navigation applications where the precision is a primary concern.

The first silicon micromachined resonant accelerometer was demonstrated by Satchell and Greenwood using piezoresistive sense and thermal actuation [23]. To cancel the effects of thermal expansion and nonlinearities, silicon resonant accelerometers with a differential matched resonator configuration are originally proposed and conceptually demonstrated by R. T. Howe and S.C. Chang [24], [25]. In their proposed structure, resonant accelerometers have a proof mass and two beams placed in the opposite sides or four beams at each side. This prototype achieved a sensitivity of 160Hz/g. Resolution and bias stability is not measured in this prototype.

The first navigation grade silicon resonant accelerometer [18] was reported in 1994, fabricated from a hybrid process which combines the bulk micromachining to fabricate a huge proof mass and a fine reactive ion etching (RIE) process to fabricate a delicate sense resonator. The sense resonator is configured as a double ended tuning fork (DETF). The performance achieved was bias stability<50ug and TCF=42ppm, but the sensitivity and the unloaded frequency was not disclosed. An improved version [26] from the same group has a sensitivity of 680Hz/g at 90kHz unloaded frequency and 0.1ug (or 0.75ppb) bias stability.

Although the lateral structure of resonant accelerometer described in [25] is straightforward, z-axis structure using bulk-micromachining and silicon-glass wafer bonding dominates the early development of resonant accelerometer. Taking advantage of a big proof-mass and large sensitivity, a navigation-grade resonant accelerometer was reported [27]. It has a chip size of 10.2mmx8.3mm

and a $2\mu\text{g}$ bias stability in more than several days.

A resonant accelerometer employing piezoresistive sense and electrostatic drive was reported by D.W. Burns, et al. [19]. It had a similar structure and chip size as [18] but reached a much worse performance. The performance it achieved was: sensitivity greater than 700Hz/g , root Allen variance below $140\mu\text{g}$, and seven day stability less than 1.4mg , almost two orders of magnitude worse than [18]. It suggests that capacitive sense and electrostatic actuation is the key feature for resonant accelerometers to achieve navigation grade performance.

Resonant accelerometer can be fully integrated with CMOS interface circuit using modified CMOS process with surface micromachining option. Surface micromachining is virtually a two dimension process in which the proof mass has the same thickness as that of sense resonators, hence a small proof mass. To maintain enough sensitivity under such a small proof mass, a leverage mechanism that multiplies the force applied axially to the sense resonator, is a must. BSAC (Berkeley Sensors and Actuators Center) in University of California, Berkeley reported such a surface micromachined resonant accelerometer employing leverage mechanism [21]. The sense resonator used in this design is actually double-ended tuning-fork comb resonators. Its motion is sensed capacitively and driven electrostatically. The sensor is integrated with a CMOS interface circuit on chip. It achieved 45Hz/g sensitivity @ 68kHz base frequency, root Allen variance below 38mHz . An improved version of this kind of accelerometer was published in 2002 [28].

Similar resonant accelerometer design for surface micromachining can be

applied to dissolved wafer process which produces devices with uniform but thick structure. The Charles Stark Draper Laboratory reported one navigation grade resonant accelerometer based on silicon-on-glass dissolved wafer process [20]. This structure has a 12 μ m thickness. With a breadboard electronic, it achieved a one sigma bias stability of 5 μ g, and a white noise of 23 μ g/ $\sqrt{\text{Hz}}$.

Not only mechanical stiffness, but also electrostatic stiffness can be employed for the resonant sense of displacement. The nonlinear transfer characteristic of capacitive transducer produces a negative stiffness responding to a polarization voltage. This negative stiffness is a function of displacement for plane capacitive transducer, therefore, applying a DC voltage between the two plates of a conventional capacitive Z-axial accelerometer will shift the plates' natural frequency with respect to the displacement [22, 29, 30]. However, the output frequency is polarization voltage dependant, which makes it susceptible to the 1/f noise and supply voltage fluctuation and not suitable for high precision application.

In general, the previously reported silicon resonant accelerometers with navigation-grade stability (10s of μ g) is achieved by the combination of bulk-micromachining, capacitive sense, electrostatic drive, breadboard electronics made from discrete components, as well as vacuum environment. Bulk-micromachined sensor with breadboard electronics is inferior to fully integrated surface-micromachined sensor with on-chip interface circuit, in terms of system cost, power consumption, and size. However, it is difficult to design a low noise high accuracy monolithic readout circuit for SRA based on CMOS process. The

first SRA integrated with a CMOS readout circuit reached a 0.8 mg bias stability with 45 Hz/g sensitivity [21], which is two orders of magnitude away from the navigation-grade performance. Since the surface micromachining process is used and the resonator output is much weaker, the $1/f$ noise of the readout circuit dominates the poor bias stability.

Bias stability refers to the bias (offset) change during a certain period. Poor bias change can be caused by environmental factors such as temperature or by random factors such as $1/f$ noise. Since the temperature effect can be compensated in a number of ways, the ultimate precision of accelerometer is determined by the random bias change. In this paper, bias stability refers to the random bias change to simplify the writing. In contrast to white noise, the bias change caused by $1/f$ noise can not be reduced by averaging and therefore must be minimized in the readout circuit. In SRA, the $1/f$ noise appears as $1/f^3$ sideband, known as $1/f^3$ phase noise, around the frequency of oscillation and pollutes the frequency reading.

The mechanism and the model of phase noise, in a MEMS oscillator, will be reviewed in chapter 5. In the next chapter, the operation principle of silicon resonant accelerometer will be presented.

Chapter 3 Silicon resonant accelerometer

3.1 Sense principle

A resonant accelerometer is a device that measures the frequency changes of sense elements under applied acceleration. As shown in Fig. 3.1, a typical silicon resonant accelerometer has a proof mass and two sense resonators placed at opposite sides along the axis of acceleration. When it is subject to acceleration, the proof mass will axially loads the beams of sense resonators and shift their stiffness and hence their natural frequencies.

The frequency difference between the two sense resonators is the measure of the acceleration. To detect the frequency difference, the sense resonators are excited to their individual natural frequencies, f_1 and f_2 , by self-oscillation loops. The two output frequencies are mixed together and passed through a low pass filter (LPF) to remove the high frequency artifacts, as shown in Fig. 3.1. The output frequency difference can then be measured either by analog methods such as phase-locked loops, or digital methods such as counting the zero-crossings and comparing it to a high precision clock. For accuracy, the oscillation loop design should make sure that the oscillator oscillates precisely at the sense resonator's natural frequency.

One drawback of using of the silicon micromachined resonator as the sense element is its temperature dependence. Because of the temperature sensitivity of

the elastic modulus of the material, the natural frequency of the resonator is a strong function of the ambient temperature. This gives the resonant sensor a poor temperature stability. The problem is overcome by the use of differential topologies. Instead of relying on the absolute frequency reading of a resonant beam, this device reads the frequency difference between two matched resonators as the output of the sensor. A shift in the ambient temperature will cause the frequencies of both resonators to change. Provided that the resonators are well-matched, they will shift the same amount. And the frequency difference will remain unchanged. This 'push-pull' scheme cancels the temperature drift to the first order. This scheme is not limited to cancel the temperature effect only. As a matter of fact, any common mode error present in both of the sense resonators, such as the frequency shift caused by the residue stress, the systematic fabrication error and etc, can be rejected by the fully differential topology as well.

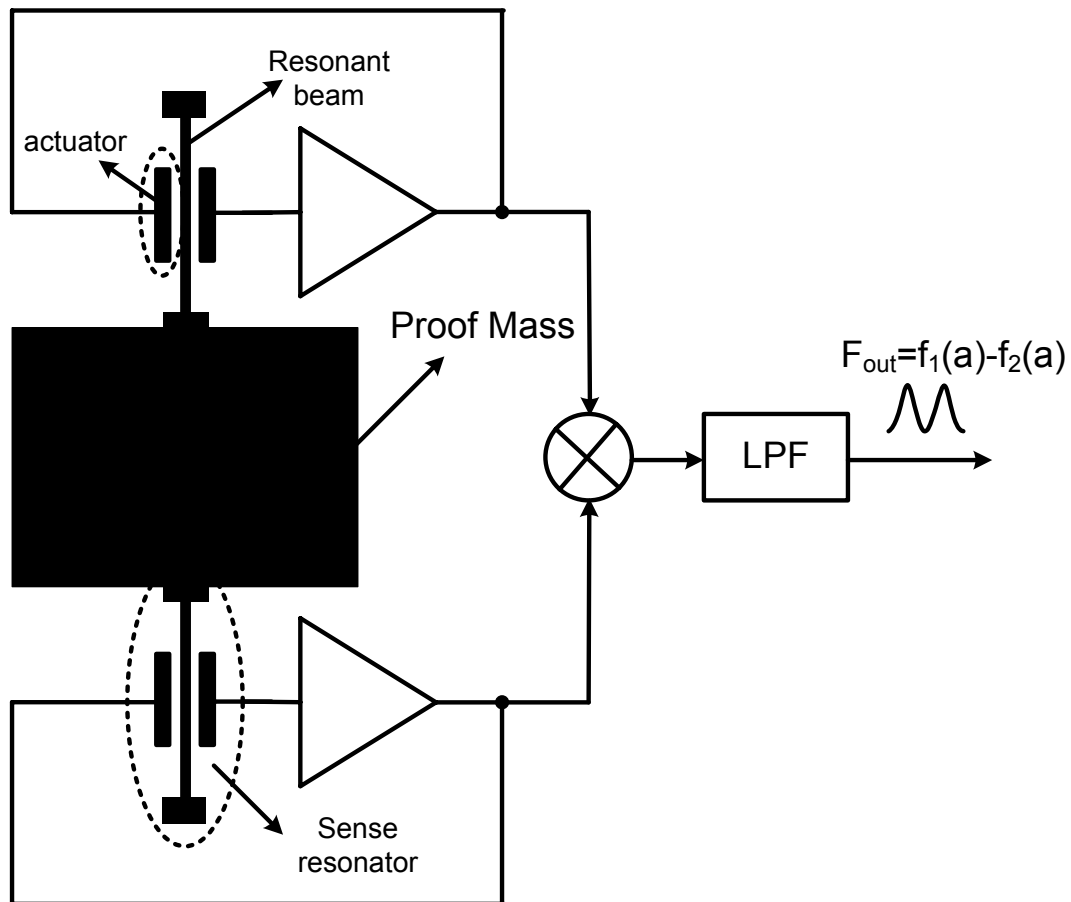


Figure 3.1 Schematic diagram of a typical differential resonant accelerometer

3.2 Mechanical analysis of resonant beam

The sense resonator in resonant accelerometer is made out of a resonant beam and its associated actuator. This resonator belongs to the clamped-clamped resonator category as both of the ends of the resonant beam are clamped. The dimensions of the resonant beam and the material from which the sense resonator is made determine its natural frequency and its frequency sensitivity to the applied force.

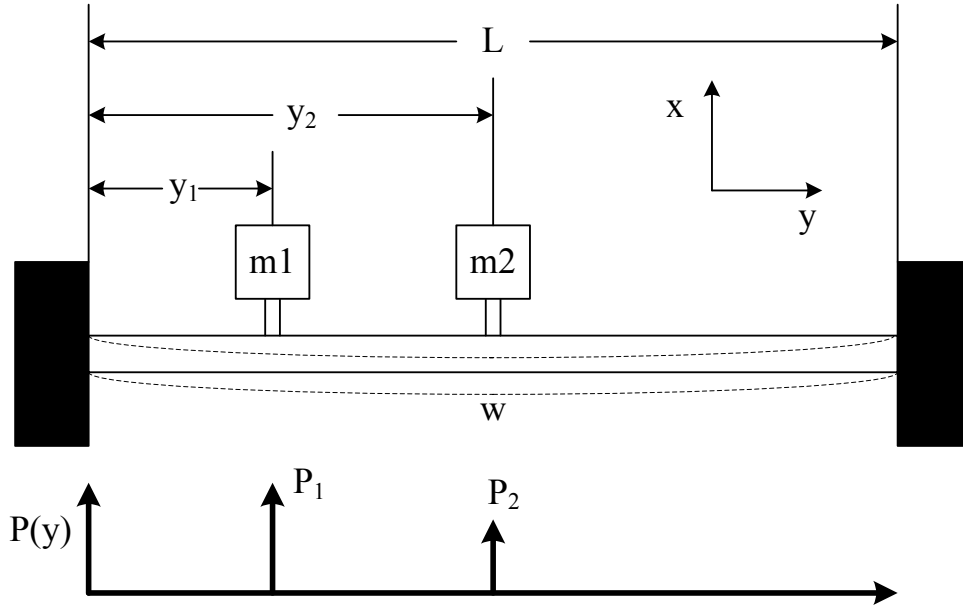


Figure 3.2 Beam model used for vibration analysis

The model for analyzing the vibration of a clamped-clamped beam is shown Fig. 3.2. The resonant beam is fixed at both ends with one or more masses placed along it. The lumped masses model the masses of the comb actuator, which will be discussed in the next subsection. The differential equation that describes the motion of the beam is thus given below [31]

$$\frac{\partial^2}{\partial y^2} \left(EI \frac{\partial^2 w}{\partial y^2} \right) + \frac{\partial}{\partial y} \left(F \frac{\partial w}{\partial y} \right) + \rho A \frac{\partial^2 w}{\partial t^2} = P(y) \quad (3.1)$$

where w is the deflection of the beam, E is the modulus of elasticity of the material, I is the inertial momentum of the beam cross-section, F is the axial tension applied to the beam, ρ is the density of the material, A is the beam cross-sectional area, and P is the transverse force applied to the beam. For the unforced motion, P is zero everywhere except where the actuation masses locate, where the inertial force of each mass has to be considered

$$P = \sum_j m_j \ddot{w}(y_j) \delta(y_j) \quad (3.2)$$

where m_j is the j th mass and y_j is the position of that mass. The boundary conditions for this beam are given below

$$w(0) = w(L) = 0$$

$$\frac{dw}{dy}(0) = \frac{dw}{dy}(L) = 0 \quad (3.3)$$

To solve Eq. (3.1), assume the motion of the beam is a linear combination of a number of vibration modes, each independent from the others and each being defined by the “modal coordinate” $x_i(t)$ multiplied by the “mode shape” $\phi_i(y)$

$$w(t, y) = \sum_i x_i(t) \phi_i(y) \quad (3.4)$$

Given this, the following equation can be derived [31]

$$\left(\int_0^L \rho A \phi_i^2 dy + \sum_j m_j \phi_i^2(y_j) \right) \ddot{x}_i + \left(EI \int_0^L \left(\frac{\partial^2 \phi_i}{\partial y^2} \right)^2 dy + F \int_0^L \left(\frac{\partial \phi_i}{\partial y} \right)^2 dy \right) x_i = 0 \quad (3.5)$$

The first term in the above equation can be thought of as the inertia term and the second as the stiffness term. Thus the effective mass and the effective stiffness can be defined as

$$M_{eff} = \int_0^L \rho A \phi_i^2 dy + \sum_j m_j \phi_i^2(y_j) \quad (3.6.a)$$

$$K_{eff} = EI \int_0^L \left(\frac{\partial^2 \phi_i}{\partial y^2} \right)^2 dy + F \int_0^L \left(\frac{\partial \phi_i}{\partial y} \right)^2 dy \quad (3.6.b)$$

Note that the effective stiffness is linearly proportional to the axial tension F . This effect is the very effect that causes the frequency shift of sense resonator under applied acceleration. Using these definitions, the motion equation can be written

as

$$M_{eff}\ddot{x}_i + K_{eff}x_i = 0 \quad (3.7)$$

The natural frequency corresponding to this particular mode is given

$$\omega_n = \sqrt{\frac{K_{eff}}{M_{eff}}} \quad (3.8)$$

According to the classical beam theory [32], the first resonance mode shape for this clamped-clamped beam is

$$\phi_1(y) = C\{\sinh(\beta y/L) - \sin(\beta y/L) - \alpha[\cosh(\beta y/L) - \cos(\beta y/L)]\} \quad (3.9)$$

where the constants are $C \approx 0.619$, $\beta \approx 4.73$, $\alpha \approx 1.018$. Assuming the excitation force is applied at the center of the beam, the lumped effective mass and the spring constant corresponding to the first resonance mode are

$$m = 0.396\rho whL_0$$

$$K_{eff} = 125.1 \frac{YI}{L_0^3} \quad (3.10)$$

where I is the inertial momentum of the beam cross-section, Y is the Young's modulus, h is the beam height, w is the beam width, and L_0 is the beam length.

3.3 Mechanical leverage-force amplifier

In order to maximize the sensitivity achievable with a relatively small proof mass, a pair of mechanical leverages is used to amplify the forces axially applying to the resonant beams. A mechanical leverage consists of a pivot beam with one end fixed at an anchor, and a rigid bar to approximate a fulcrum and a lever, as shown in Fig. 3.4. The input of the leverage, F_{in} , is the inertial force of

the proof mass while the output of the leverage, F_{out} , is the force applied to the resonant beam. With the improved sensitivity from the amplified force, the noise floor and the bias stability of this acceleration sensor can be greatly improved with a reasonable silicon real estate. However, the maximum achievable force amplification factor is usually limited to an order of magnitude, because the bending of the pivot beam causes an energy loss and lowers the actual force multiplication ratio.

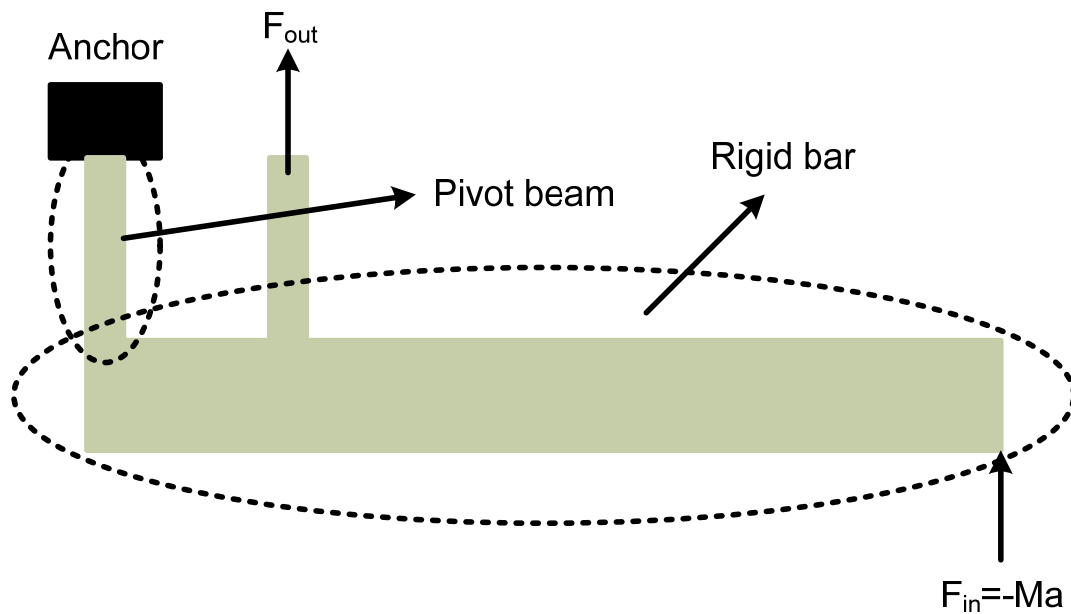


Figure 3.3 illustration of a mechanical leverage

3.4 Electrostatic Actuation

The resonant beam studied here is excited electrostatically. The concept of electrostatic Actuation has been covered in a number of works [33, 34], so only the basics about electrostatic actuation are reviewed here.

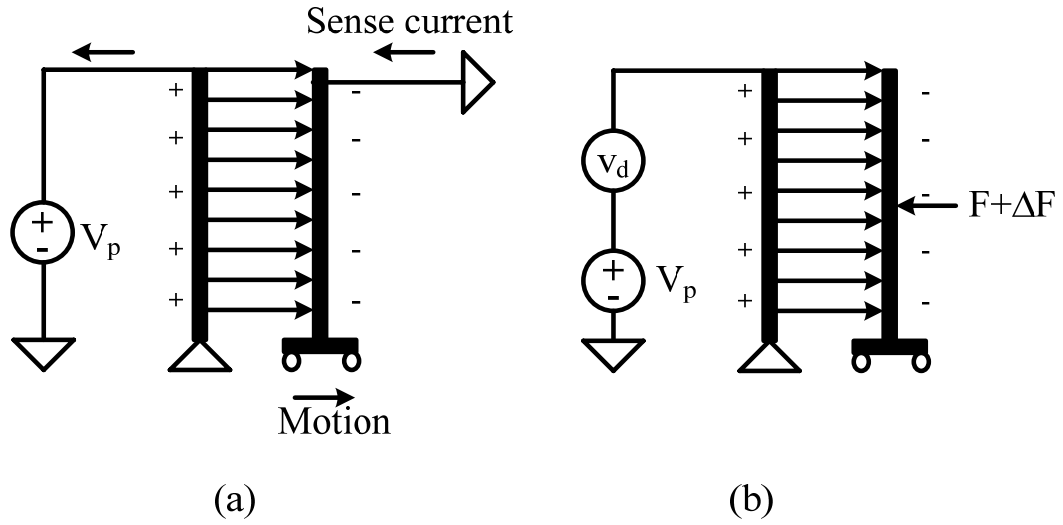


Figure 3.4 Electrostatic actuation

The purpose of an electrostatic actuator is to convert a mechanical power in the form of force, position and velocity to an electrical power in the form of voltage and current, or vice versa. This conversion is done through the capacitor formed between the stationary part and the movable part of the actuator. As shown in Fig. 3.4(a), a charge is stored across the capacitor when a DC voltage (referred to as V_p or the ‘polarization voltage’) is applied across it. If the parts move apart, the capacitance (and therefore the stored charge) decreases, resulting in a charge stream, or current, to flow from the structure.

The motion-to-current transduction factor can be derived by considering the amount of charge stored across the transducer

$$i_s = \frac{dQ}{dt} = \frac{dC}{dt} V_p = \frac{dC}{dx} V_p \frac{dx}{dt} \quad (3.11)$$

where i_s is the sense current produced by the motion. Note that the polarization voltage is assumed to be constant on the sense node. The above equation

shows that the output current is proportional to the velocity of the movable portion of the transducer, assuming dC/dx is a constant.

An electrostatic force is also produced between the moving parts and stationary parts due to the attraction of positive and negative charges. Both the voltage-to-force and motion-to-current relations can be simply derived by taking the actuator as a variable capacitor. The amount of energy stored in the actuator is

$$U = \frac{1}{2} C V_p^2 \quad (3.12)$$

where C is the capacitance between the two parts of the electrode, and V_p is the polarization voltage applied across the actuator. The force exerted between the parts can be found by dU/dx , or

$$F = \frac{1}{2} \frac{\partial C}{\partial x} V_p^2 \quad (3.13)$$

where x is the position of the movable structure. A small voltage variation v_d in the polarization voltage results in a small incremental force change (Fig. 3.4(b))

$$\Delta F = F(V_p + v_d) - F(V_p) \approx \frac{\partial C}{\partial x} V_p v_d \quad (3.14)$$

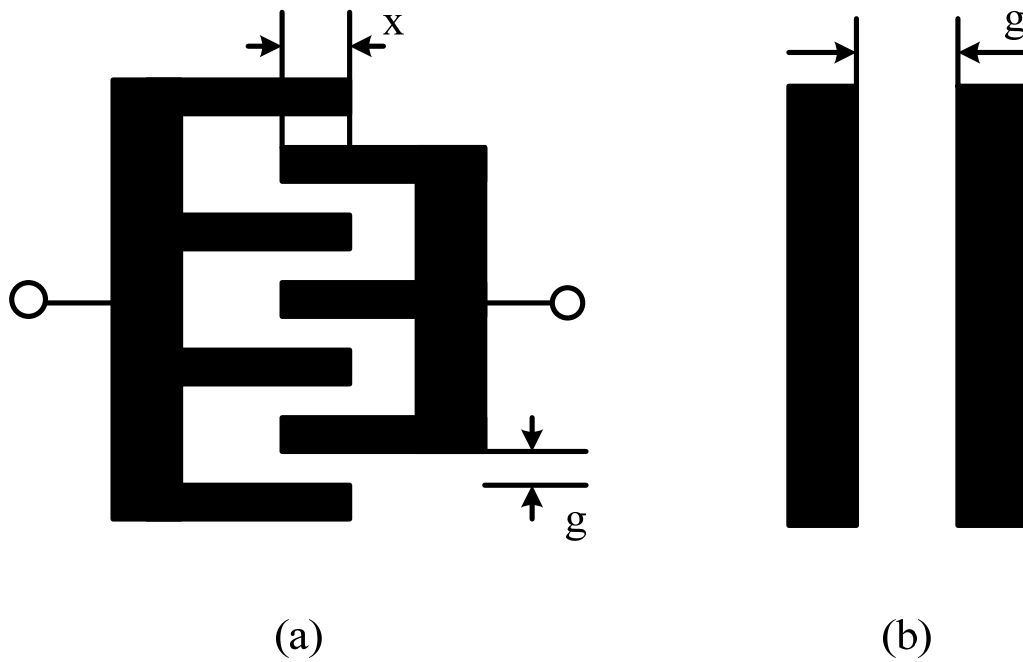


Figure 3.5 (a) Comb drive actuator and (b) parallel plate actuator

There are two kinds of electrostatic actuators that are frequently used. One is comb-drive actuator while the other one is parallel-plate actuator. A comb drive actuator consists of two sets of interdigitated combs, as is shown in Fig. 3.5(a). The variable capacitor formed in this actuator can be viewed as a series of parallel-plate capacitors connecting in parallel. Since the capacitance change is caused by the change in overlap area between the two combs, it varies linearly with the position of the combs. This linear variance results in a constant dC/dx , independent of position. The capacitance associated with this structure is

$$C = \frac{N\epsilon tx}{g} \quad (3.15)$$

Where N is the number of comb gaps, ϵ is the dielectric constant, t is the structure thickness, x is the overlap between the combs, and g is the comb gap

distance. Applying Eq. 3.15 to Eq. 3.11 and Eq. 3.14, the voltage/force and the motion/current relation are derived

$$F = \frac{N\epsilon t}{g} V_p v_d \quad i_s = \frac{N\epsilon t}{g} V_p \frac{dx}{dt} \quad (3.16)$$

In reality, the above equations are only approximations due to the presence of fringing fields.

The other common class of electrostatic transducers is the parallel plate (Fig. 3.5(b)), where the capacitance change is due to the change in the distance between two plates. The capacitance of this structure is

$$C = \frac{\epsilon A}{g} \quad (3.17)$$

where A is the overlap area and g is the gap distance. So the voltage/force and motion/current relations are

$$F = \frac{\epsilon A}{g^2} V_p v_d \quad i_s = \frac{\epsilon A}{g^2} V_p \frac{dg}{dt} \quad (3.18)$$

Note that as the movable plate changes position, the gap size will change as well. This dependence of the transduction constants on plate position illustrates the nonlinearity of the parallel plate method. This kind of transducer provides higher transduction, but is also very nonlinear with position. This nonlinearity results in a negative stiffness which appears as a frequency offset at the resonant frequency. Since it is very difficult to implement a polarization voltage as stable as the mechanical property of bulk silicon, this frequency offset caused by the negative stiffness is a source of frequency instability. Therefore, to achieve higher bias stability, comb drive actuator is generally preferred to parallel plate actuator.

3.5 Damping

Damping refers to the mechanism that causes the energy loss. It has been neglected in the preceding dynamic analysis but is an important consideration in the design of a MEMS resonator. Damping gives rise to Brownian noise and determines the quality factor which limits the ultimate achievable frequency resolution. For this reason, care must be taken to reduce the damping either through the mechanical design or vacuum packaging.

There are two main sources of damping in the MEMS resonators, one is the viscous damping from ambient gas and the other one is the structural damping from the material itself. Viscous damping dominates at atmospheric pressure or low vacuum level. It appears as a force against the motion of object and is proportional to the velocity of an object, as is given below

$$F_{damp} = -\eta v \quad (3.19)$$

where F_{damp} is the damping force, η is the damping coefficient, and v is the velocity of the object. In the case of comb-drive actuator, the opposite plates move parallel to each other, as shown in Fig. 3.6(a), causing a Couette flow damping (also known as slid film damping).

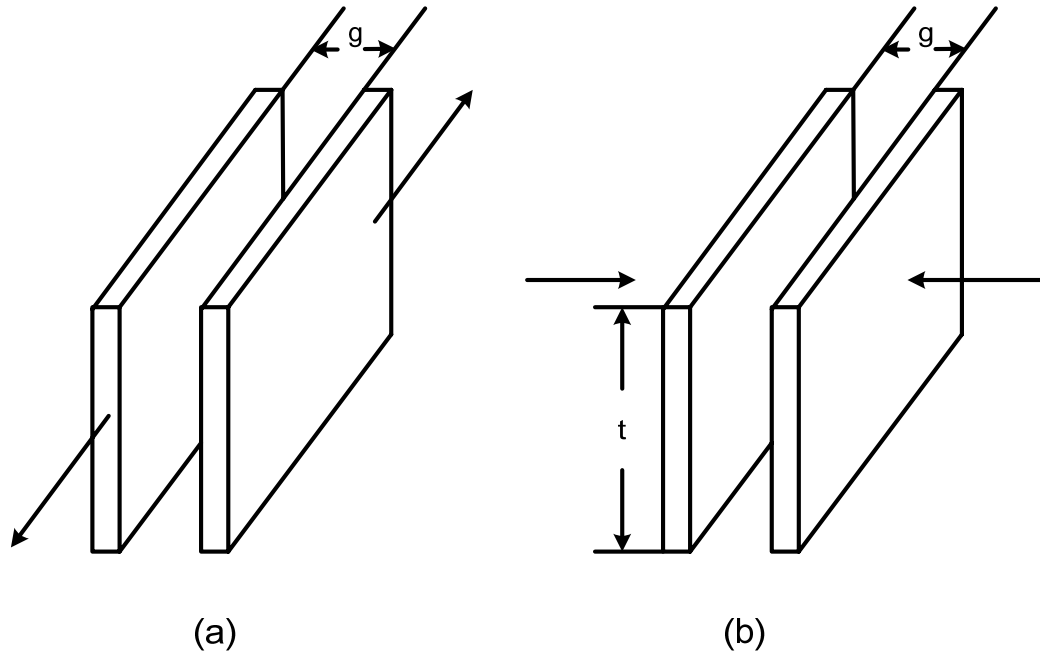


Figure 3.6 Illustration of (a) Couette flow damping and (b) Squeeze film damping

The damping caused by Couette flow is given by

$$\eta = \mu \frac{A}{g} \quad (2.20)$$

where η is the damping coefficient, μ is the fluid viscosity, A is the overlapping area, g is the gap distance.

In the case of parallel plate actuator, opposite plates move to and fro with respect to each other (Fig. 3.6(b)). The gas in the gap is compressed and squeezed out the perimeter of the plates. The behavior of the squeezed film differs depending on how fast the plates move. For fast moving, the gas is mostly compressed and behaves like a spring. For slow moving, the gas is mostly squeezed out which results in a squeeze film damping.

The viscous damping has been studied in a number of works [35-37], here only the concepts are introduced. In a real case, the viscous damping is more

complicated than the simplified Couette flow damping or squeeze film damping and requires numerical simulation to determine its exact value.

In a high vacuum environment, structural damping will tend to dominate over fluid damping [38]. Structural damping arises from viscoelastic strain in the mechanical element. With structural damping, the energy dissipated in each vibration cycle is proportional to the vibration amplitude. It means that the damping coefficient is no more a constant, as is in a typical viscous damping. As a matter of fact, the effective quality factor caused by structural damping tends to increase at an increased amplitude. However, to simplify analysis, the structural damping related quality factor is assumed to be a constant [39].

3.6 Equivalent electrical network

With the help of electrostatic actuators, the MEMS resonator is no more a mechanical component. Instead, it can be modeled as an electrical network. This network has a voltage input at the drive electrode and a current output at the sense electrode. Fig. 3.7 shows the transformation of the MEMS resonator to an equivalent RLC network, with the relationships between mechanical parameters to electrical parameters indicated. This transformation shows that the equivalent resistance R_{eff} inversely proportional to the square of polarization voltage V_p .

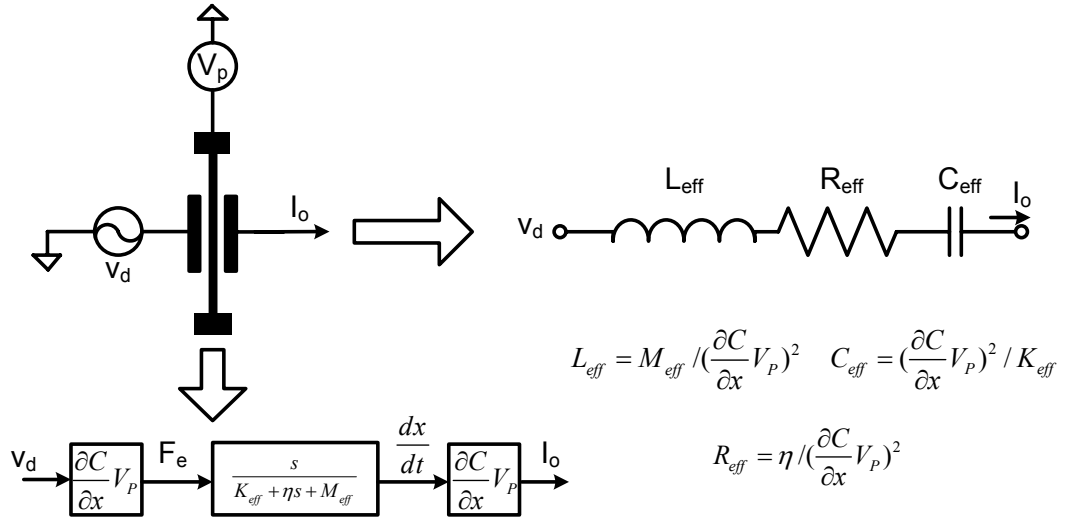
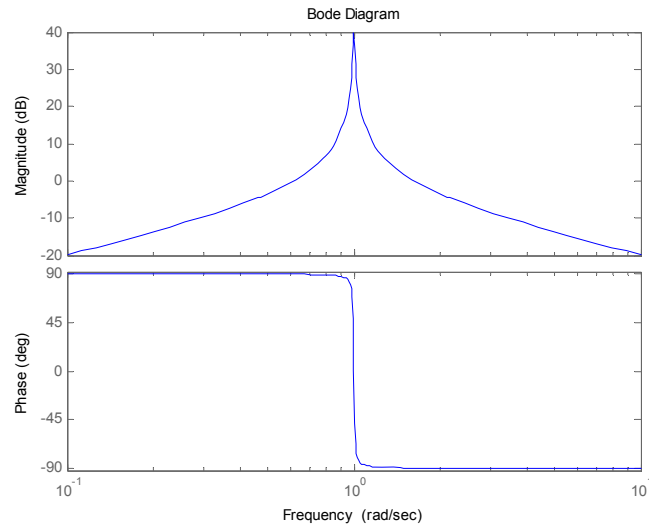


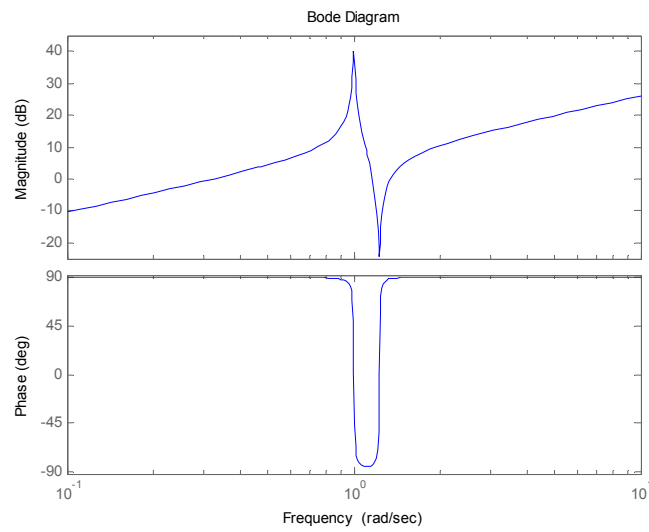
Figure 3.7 Transformation of a MEMS resonator to an equivalent RLC model

3.7 Parasitic electrical coupling

Parasitic electrical coupling, also known as feedthrough, refers to the undesirable signal caused by the parasitic electrical components. Fig. 3.8 conceptually illustrated the possible coupling paths for a MEMS resonator. The MEMS resonator itself is represented by a RLC network. The motion current caused by the electrical-mechanical actuation is identified as I_m . C_{ft} represents the parasitic capacitance between the drive and sense node. To drive, to sense, and to polarize the resonator from the outside, 3 pads are required. Their parasitic capacitances to the substrate are represented by C_{p1} - C_{p3} . However, the substrate itself is not an ideal conductor, thus is modeled as a T-shape network. I_{cft} represents the electrical coupling through the parasitic capacitance C_{ft} . I_{sft} represents the electrical coupling through the substrate. Fig. 3.9 conceptually



(a)



(b)

Figure 3.9 Illustration of the frequency response of a MEMS resonator (a) without parasitic electrical coupling and (b) with parasitic electrical coupling. The frequency is normalized to its natural frequency.

3.8 Fabrication process

We chose a silicon-on-insulator (SOI) process [41] to fabricate our resonant accelerometer sensor to exploit the super stable mechanical property of single-crystal silicon and the perfect temperature matching between the substrate and the structure layer. This SOI process starts with a SOI wafer which consists of a 25 μm top structural silicon layer, a 1 μm oxide layer and a thick substrate layer (Fig. 3.10(a)). The top Silicon layer is doped to enhance its conductivity (Fig. 3.10(b)). A metal stack (“pad metal”) consisting of 20 nm Cr and 500 nm Au is deposited and patterned on top of the electrodes which will be defined in the later processes to further enhance their conductivity (Fig. 3.10(c)). The top silicon layer is lithographically patterned and deep reactive ion etched (DRIE) to define the mechanical structures (Fig. 3.10(d)). Next, the wafer is selectively etched through the substrate layer from the backside to make trenches (Fig. 3.10(e, f)). These trenches not only release the movable structures in the top silicon layer, but also suppress the substrate parasitics. At last, on top of the wafer, a “shadow mask” is temporarily bonded, through which a second metal layer (blank metal) is deposited (Fig. 3.10(g, h)). The deposited metal layer, or ‘blanket metal’, is frequently used for large metal lines such as the substrate contact.

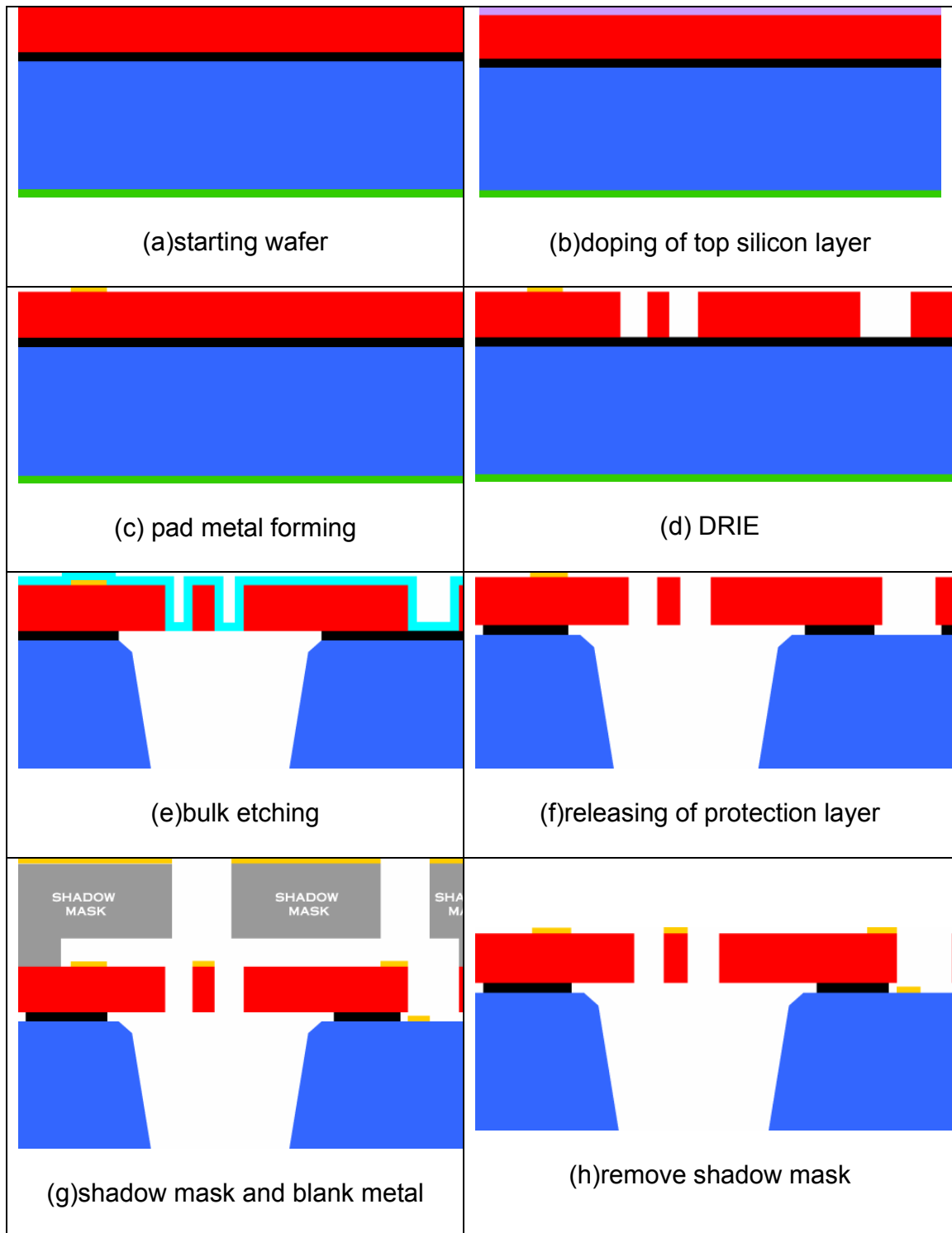


Figure 3.10 SOI process flow

3.9 Our resonant accelerometer design

Our SRA design is conceptually sketched in Fig. 3.11. Since the whole structure is released with the through-hole from backside, the anchors in the mechanical leverages are not allowed to be placed in the center. Hence the mechanical leverages are modified with the anchors placed at the corner (shown in Fig. 3.11). The details of the modified mechanical leverage can be clearly seen in the microphotograph in Fig. 3.12. As is discussed in Section 3.3, the bending of the pivot beam caused the loss of amplification factor. Therefore, to minimize the bending of pivot beam, an additional wide rigid bar is inserted to strengthen the structure below the leverage. The pivot beam is also intentionally designed to be a slim one for the same reason. A clumper is included to prevent the motion at the end of resonant beam to make sure the resonant beam vibrates at the desirable mode. With the aid of a finite element analysis tool, this modified structure was finely adjusted to reach an optimum force amplification ratio of around 35. To further improve the sensitivity, a layer of “blank metal” is deposited on top of the proof mass. The accelerometer achieves a sensitivity of 140Hz/g with a nominal frequency of 135 kHz.

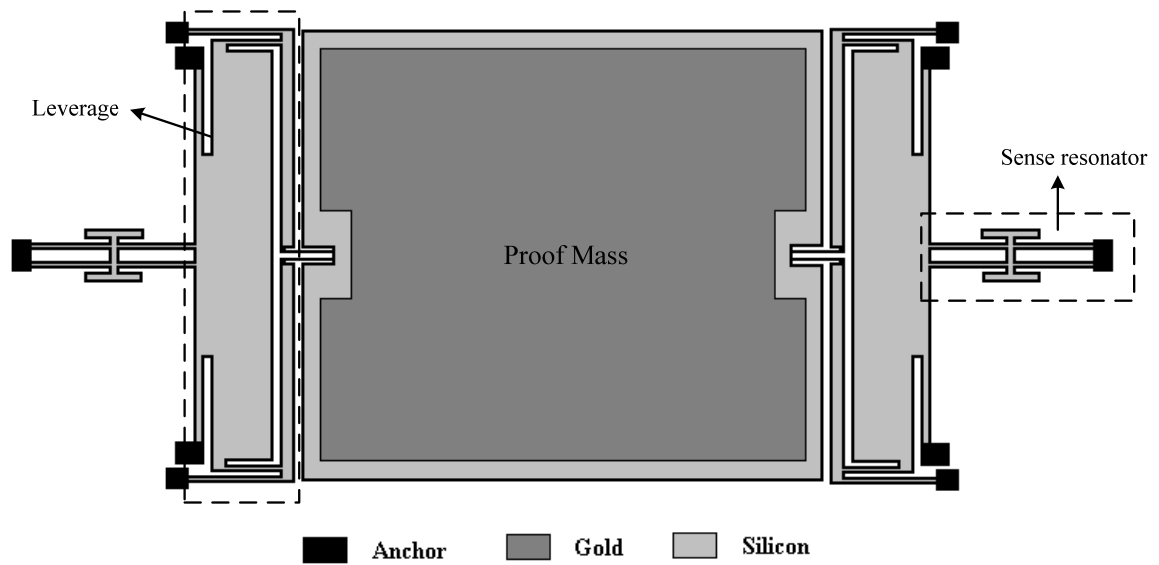


Figure 3.11 Schematic diagram of the resonant accelerometer based on SOIMUMPs process

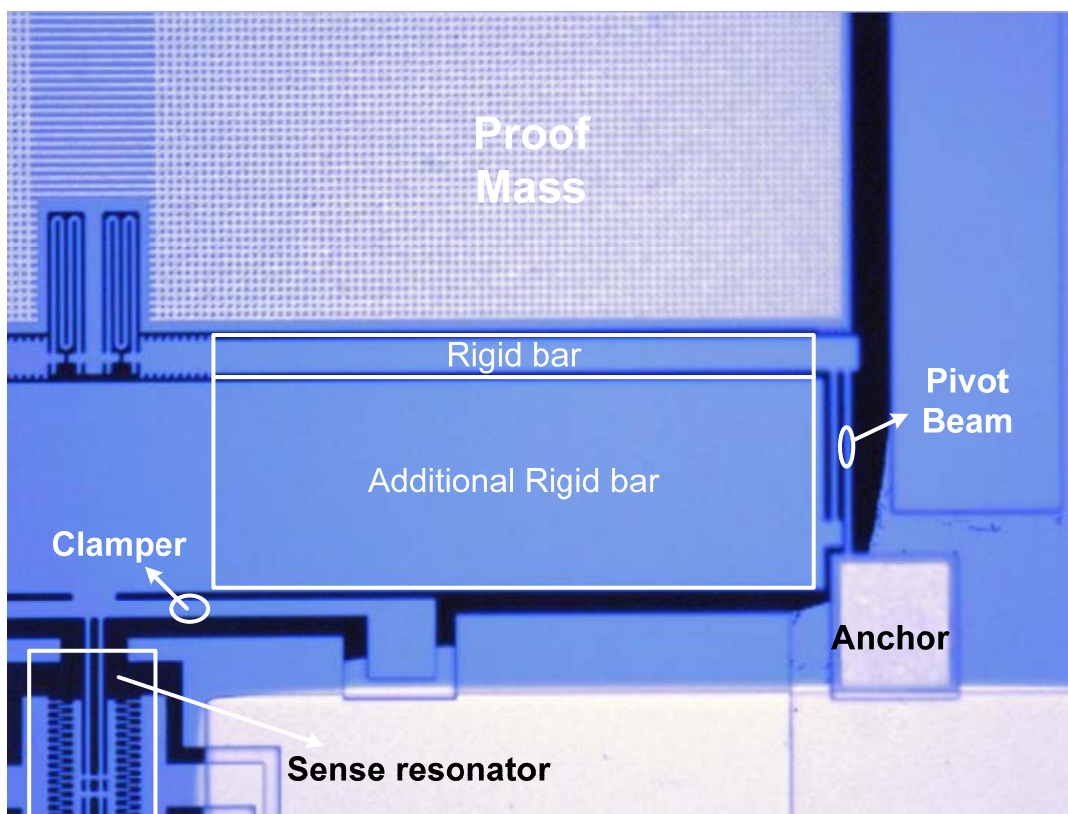


Figure 3.12 Microphotograph of a mechanical leverage in the resonant accelerometer

The sense resonator is a key component in a resonant accelerometer. In the previous work [18-20], the sense resonators are made with a double-ended tuning fork (DETF) structure shown in Fig. 3.13(a). The two beams are excited exactly 180° out-of-phase during the operation to minimize the acoustic radiation. Although this structure helps achieve a good quality factor (Q), it favors only single-ended operation. In our design, to take advantage of differential operation, a connection is made at the center of DETF, as shown in Fig. 3.13(b), which forces both beams to move exactly in-phase with each other, resulting in a differential capacitance change. Comb structures are chosen for electro-mechanical transduction for their good linearity. The sense resonator has a measured Q of 30,000 @ 0.1m bar (Fig. 3.14(b)), compared with the Q of DETF resonator in the range of 50,000-100,000. The reduced Q of the new sense resonator is already high enough to bring the motion current above the noise level under a 3.3 V polarization voltage. However, due to the strong parasitic electrical coupling, the resonant peak is barely seen at 3.3 V, as shown in Fig. 3.14 (a).

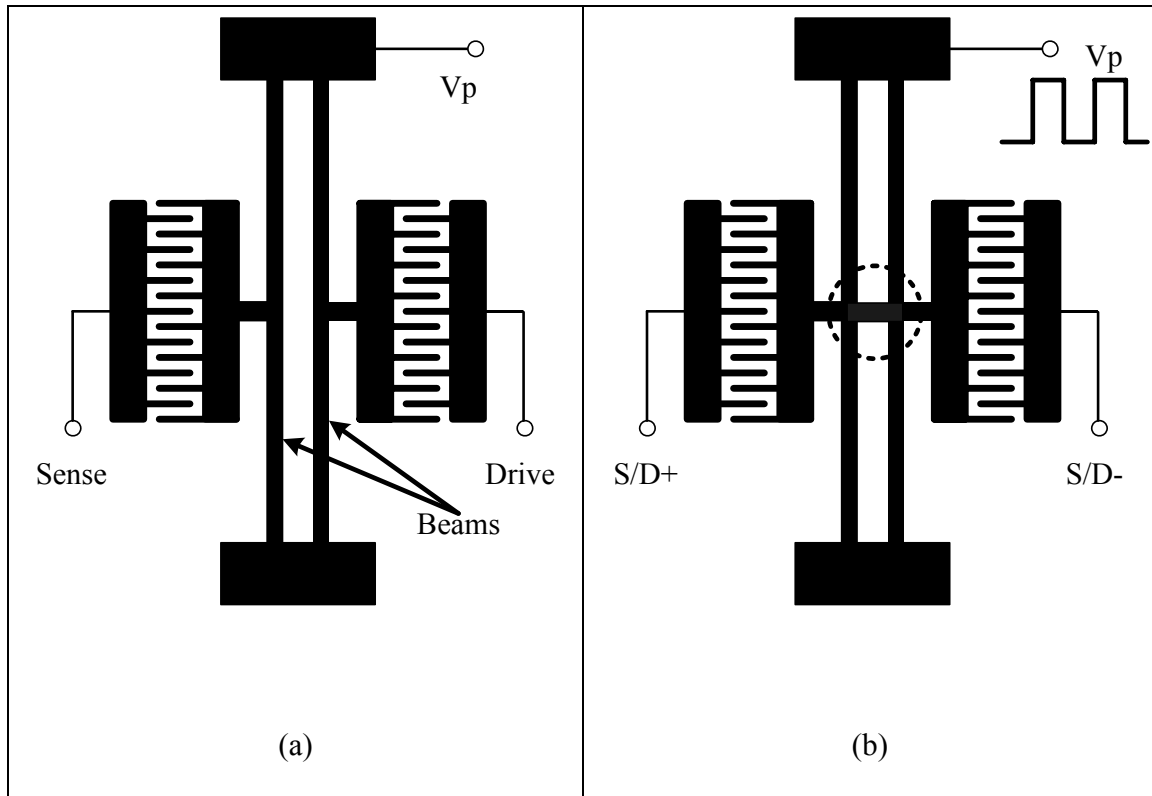
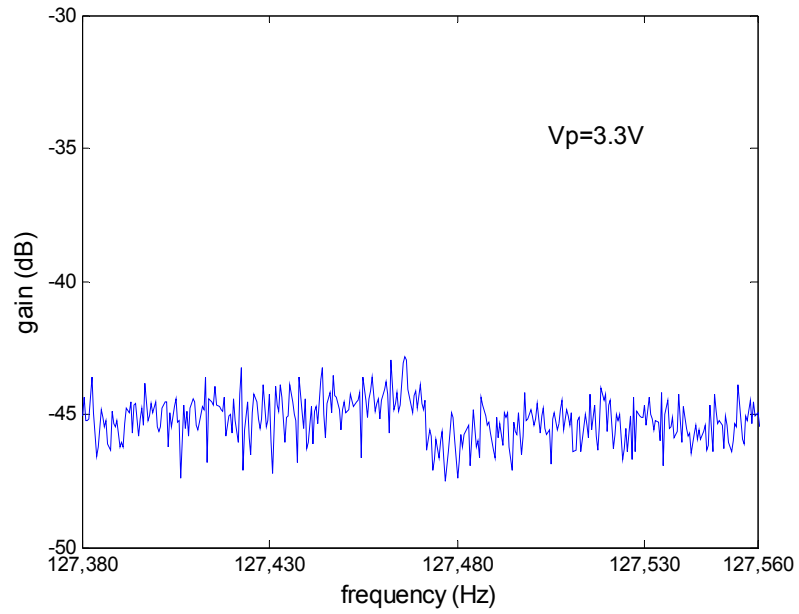
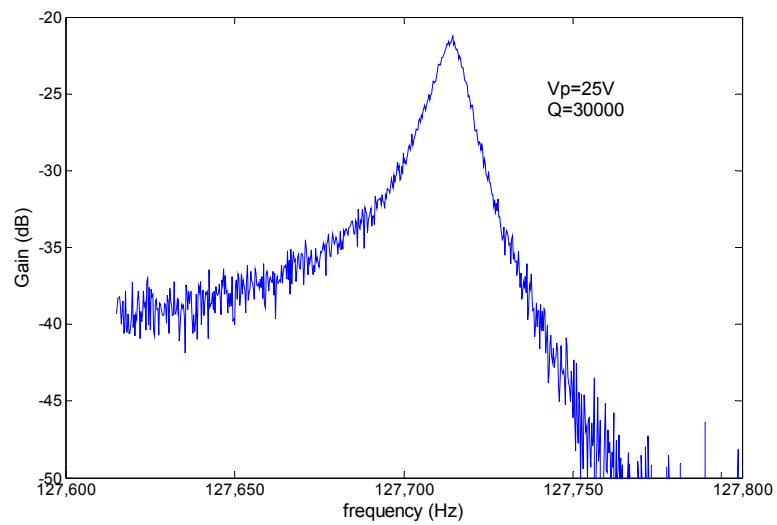


Figure 3.13 (a) Double-ended tuning fork for single-ended operation and (b) modified structure for fully-differential operation.



(a)



(b)

Figure 3.14 Measured sense resonator frequency response (a) at 3.3 V polarization voltage and (b) at 25 V polarization voltage.

Chapter 4 Resonator nonlinearities

Strictly speaking, every physical device exhibits nonlinear characteristics, but the nonlinearities are usually so small that are ignored in analysis. However, due to the overwhelmingly high quality factor and the relatively large amplitude to achieve enough signal-noise-ratio, nonlinearities play an important role in the dynamic behavior of a MEMS resonator. This section reviews the origin of nonlinearities in the electrostatically actuated MEMS resonators and their forced dynamic response.

4.1 Origin of nonlinearities

The nonlinearities in MEMS resonators can have mechanical and/or capacitive origin. The mechanical nonlinearity is due to geometrical and material effects in the resonating element while the capacitive nonlinearity is due to nonlinear characteristic of electrostatic force. In this section, both effects are briefly reviewed.

4.1.1 Geometrical

(A) Clamped-clamped beam resonator

The dominant source of nonlinearities present in the resonant beam is the mechanical nonlinearity due to geometrical effect. Take the clamped-clamped

beam resonator as an example, as its vibration amplitude increases, the resonant beam is forced to extend, as shown in Fig. 4.1. This extension causes additional axial force, adding to the stiffness in the structure. This stiffness is a function of vibration amplitude. At larger amplitude, the stiffness increases and causes the resonant frequency to increase. This effect can be analyzed using energy method [2]: The amount of extension of the beam for a given vibration amplitude is

$$\Delta L = \frac{1}{2} \int_0^L \left(\frac{dw}{dy} \right)^2 dy \quad (4.1)$$

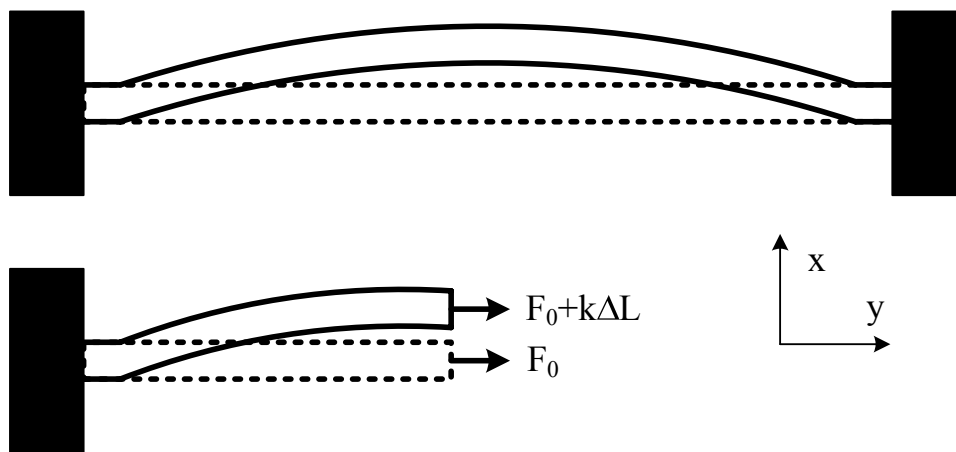


Figure 4.1 Geometrical effect that leads to the nonlinearity in the clamped-clamped beam resonator.

The extra potential energy caused by extension can thus be found

$$\begin{aligned}
 U_{extra} &= \frac{1}{2} k (\Delta L)^2 = \frac{1}{2} \left(\frac{EA}{L} \right) \left(\frac{1}{2} \int_0^L \left(\frac{dw}{dy} \right)^2 dy \right)^2 \\
 &= \frac{1}{8} \left(\frac{EA}{L} \right) \left(\int_0^L \left(\frac{dw}{dy} \right)^2 dy \right)^2
 \end{aligned} \tag{4.2}$$

where k is the stiffness of the axial beam spring, EA/L .

With the extra extension energy included, the total potential energy of the resonant beam is

$$\begin{aligned}
 U_{total} &= U_{bend} + U_{axial} + U_{extra} \\
 &= \frac{1}{2} \int_0^L EI \left(\frac{d^2 w}{dy^2} \right)^2 dy + \frac{1}{2} \int_0^L F \left(\frac{dw}{dy} \right)^2 dy + \frac{1}{8} \frac{EA}{L} \left(\int_0^L \left(\frac{dw}{dy} \right)^2 dy \right)^2
 \end{aligned} \tag{4.3}$$

Replace w with $x(t)\phi(y)$ and normalize y to ε , with $\varepsilon = y/L$

$$U_{total} = \left(\frac{1}{2} \frac{EI}{L^3} \int_0^1 \left(\frac{d^2 \phi}{d\varepsilon^2} \right)^2 d\varepsilon + \frac{1}{2} \frac{F}{L} \int_0^1 \left(\frac{d\phi}{d\varepsilon} \right)^2 d\varepsilon \right) x^2 + \left(\frac{1}{8} \frac{EA}{L^3} \left(\int_0^1 \left(\frac{d\phi}{d\varepsilon} \right)^2 d\varepsilon \right)^2 \right) x^4 \tag{4.4}$$

The restoration force F_e , can be found as the derivative of U with respect to x

$$\begin{aligned}
 F_e = \frac{dU_{total}}{dx} &= \left(\frac{EI}{L^3} \int_0^1 \left(\frac{d^2 \phi}{d\varepsilon^2} \right)^2 d\varepsilon + \frac{F}{L} \int_0^1 \left(\frac{d\phi}{d\varepsilon} \right)^2 d\varepsilon \right) x + \left(\frac{1}{2} \frac{EA}{L^3} \left(\int_0^1 \left(\frac{d\phi}{d\varepsilon} \right)^2 d\varepsilon \right)^2 \right) x^3 \\
 &= K_{eff} x + K_{3,eff} x^3
 \end{aligned} \tag{4.5}$$

This is a classic governing equation of a nonlinear spring. From this equation, it is obvious that both the effective stiffness changes caused by the applied force F and by the amplitude stiffening effect are proportional to the integration $\int_0^1 \left(\frac{d\phi}{d\varepsilon} \right)^2 d\varepsilon$, which is determined by the dimension and the geometry of the resonant beam. This explains why the nonlinearity cancellation through mechanical design is not applicable to the sense resonator.

(B) Bulk acoustic wave (BAW) Resonator

The vibration mode of the beam resonator shown in Fig. 4.2 is a half wave length longitudinal mode wave. This resonator is thus referred to a bulk acoustic wave (BAW) resonator. The stiffness of the resonator exhibits nonlinearity due to the change in the cross sectional area of the beam [42]. With the cross sectional area change included, the wave equation for a longitudinal displacement $u(y,t)$ is

$$\rho A(y,t) \frac{\partial^2 u(y,t)}{\partial t^2} = \frac{\partial}{\partial y} (A(y,t) Y \frac{\partial u(y,t)}{\partial y}) \quad (4.6)$$

where ρ is the material density, Y is the Young's modulus, and $A(y,t)$ is beam cross sectional area. The deformed area $A(y,t)$ is a function of longitudinal stress S_y

$$A(y,t) = A_0 (1 - 2\nu S_y) = A_0 (1 - 2\nu \frac{\partial u}{\partial y}) \quad (4.7)$$

where ν is the poisson's ratio. The solution to Eq. 4.6 is approximated by the linear solution

$$u(y,t) = u(L,t) \sin(\frac{\pi y}{2L}) \quad (4.8)$$

where $u(L,t)$ is the motion of the beam tip. Substituting Eq. 4.8 into Eq. 4.6

and Eq. 4.7 and integrating over the mode shape leads to

$$\rho A_0 L \frac{d^2 u(L,t)}{dt^2} = -\frac{\pi^2}{4} \frac{A_0 Y}{L} u(L,t) + \frac{\pi^2}{3} \frac{\nu A_0 Y}{L^2} u(L,t)^2 \quad (4.9)$$

The effective mass and the nonlinear spring constant can be recognized as

$$m = \rho A_0 L; \quad k_0 = \frac{\pi^2}{4} \frac{A_0 Y}{L}; \quad k_1 = -\frac{\pi^2}{3} \frac{v A_0 Y}{L^2} \quad (4.10)$$

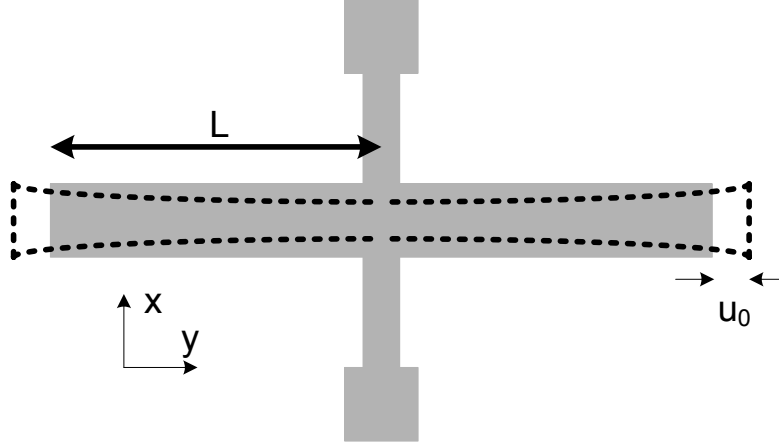


Figure 4.2 Spring softening due to change in the cross section area in the bulk acoustic wave (BAW) resonator.

4.1.2 Nonlinear Young's Modulus

Single-crystal silicon is often regarded as a linear material. However, due to their overwhelmingly high quality factor, the MEMS resonators are susceptible to even small nonlinearities from the silicon material itself. The nonlinear Young's modulus is defined as [43]

$$Y = Y_0 + Y_1 S + Y_2 S^2 \quad (4.11)$$

where $S = \partial u / \partial x$ is the displacement gradient with respect to undeformed coordinates, and Y_1 and Y_2 are the first- and second-order corrections to the linear Young's modulus Y_0 , respectively. The linear and nonlinear young's modulus terms in [100] and [110] directions are tabulated in Table 4.1[44].

Table 4.1 Nonlinear Young's modulus for single-crystal silicon

	Y ₀ (GPa)	Y ₁ (GPa)	Y ₂ (GPa)
[100]direction	130	84.5	-598
[110]direction	170	-442	-1377

Substituting Eq. 4.8 and Eq. 4.11 into the wave equation 4.6, and integrating over the mode shape leads to [44]

$$\rho A_0 L \frac{d^2 u(L, t)}{dt^2} = -\frac{\pi^2}{4} \frac{A_0 Y}{L} u(L, t) - \frac{\pi^2}{3} \frac{A_0 Y_1}{L^2} u(L, t)^2 - \frac{3\pi^4}{64 L^3} \frac{A_0 Y_2}{L^3} u(L, t)^3 \quad (4.12)$$

The effective mass and the nonlinear spring constant can be identified as

$$m = \rho A_0 L; \quad k_0 = \frac{\pi^2}{4} \frac{A_0 Y}{L}; \quad k_1 = \frac{\pi^2}{3} \frac{A_0 Y_1}{L^2}; \quad k_2 = \frac{3\pi^4}{64} \frac{A_0 Y_2}{L^3} \quad (4.13)$$

4.1.3 Capacitive transduction

Take parallel plate capacitive actuator as an example, its electrostatic force is given by

$$F_e = -\frac{V_p^2}{2} \frac{\partial C(x)}{\partial x} = -\frac{V_p^2}{2} \left[\partial \left(\frac{\varepsilon A}{d-x} \right) / \partial x \right] \quad (4.14)$$

Taken the series expansion of the capacitance

$$C(x) = \frac{\varepsilon A}{d-x} = \frac{\varepsilon A}{d} \left(\frac{1}{1-x/d} \right) = \frac{\varepsilon A}{d} \left[1 + \frac{x}{d} + \left(\frac{x}{d} \right)^2 + \left(\frac{x}{d} \right)^3 + \left(\frac{x}{d} \right)^4 o(x^4) \right] \quad (4.15)$$

The electrostatic force can be found

$$F_e = -\frac{V_p^2}{2}[\partial C(x)/\partial x] = -\frac{V_p^2}{2} \frac{\epsilon A}{d} \left[\frac{1}{d} + \frac{2x}{d^2} + \frac{3x^2}{d^3} + \frac{4x^3}{d^4} + o(x^3) \right] \quad (4.16)$$

Therefore, the electrostatic force is nonlinearly dependent on the displacement x , thus is modeled by a nonlinear spring, with the nonlinear spring constants given by

$$k_{0e} = \frac{V_p^2 \epsilon A}{d^3} \quad k_{1e} = \frac{3V_p^2 \epsilon A}{2d^4} \quad k_{2e} = \frac{2V_p^2 \epsilon A}{d^5} \quad (4.17)$$

Since the electrical spring coefficient is proportional to V_p^2 , the capacitive nonlinearity can be reduced by lowering the bias voltage. Also, the nonlinearity could be significantly reduced with different actuator configuration, e.g., comb-drive actuation.

4.2 Nonlinear forced vibration

The equation of motion for a forced oscillation is

$$m \frac{d^2 x}{dt^2} + \gamma \frac{dx}{dt} + k_0 x + k_1 x^2 + k_2 x^3 = F_\omega \cos \omega t \quad (4.18)$$

where t is the time, x is the displacement of the lumped mass m , γ is the damping coefficient, k_0 is the linear spring constant, k_1 and k_2 are the first and second order nonlinear corrections for the spring constant, and $F_\omega \cos \omega t$ is the applied harmonic force. It is useful to define the natural frequency $\omega_0 = \sqrt{k_0/m}$ and quality factor $Q = \omega_0 m / \gamma$. The solutions to Eq. 4.18 can be obtained by the method of successive approximations by assuming a solution in the following

form [45]

$$x(t) = x_0 + x_1 \cos \omega'_0 t + x_2 \cos 2\omega'_0 t + x_3 \cos 3\omega'_0 t + \dots \quad (4.19)$$

For vibrations without damping, the amplitude of the higher harmonics is given by

$$x_2 = \frac{k_1}{6k_0} x_1^2$$

$$x_3 = \left(\frac{k_1^2}{48k_0^2} + \frac{k_2}{32k_0} \right) x_1^3 \quad (4.20)$$

The resonance frequency is related to the vibration amplitude

$$\omega'_0 = \omega_0 \left[1 + \left(\frac{3k_2}{8k_0} - \frac{5k_1^2}{12k_0^2} \right) x_1^2 \right] = \omega_0 (1 + \lambda x_1^2) \quad (4.21)$$

where $\lambda = \frac{3k_2}{8k_0} - \frac{5k_1^2}{12k_0^2}$. Eq. 4.21 indicates that the existence of k_1 , no matter it is

negative or positive, will cause the peak frequency to shift to a lower frequency. Similarly, a negative k_2 results in the peak-frequency shifting to a lower frequency while a positive k_2 results in a higher peak-frequency.

The influence of the peak-frequency shift on the amplitude-frequency response is illustrated in Fig. 4.3. A typical linear amplitude-frequency response is shown in Fig. 4.3(a). A negative λ causes a tilting of the resonance peak to a lower frequency (Fig. 4.3(b)) while a positive λ results in tilting of the peak to a higher frequency (Fig. 4.3(c)). Increasing the excitation signal causes further increase in nonlinearity and eventually the amplitude-frequency response shows hysteresis (bifurcation) (Fig. 4.3(d)).

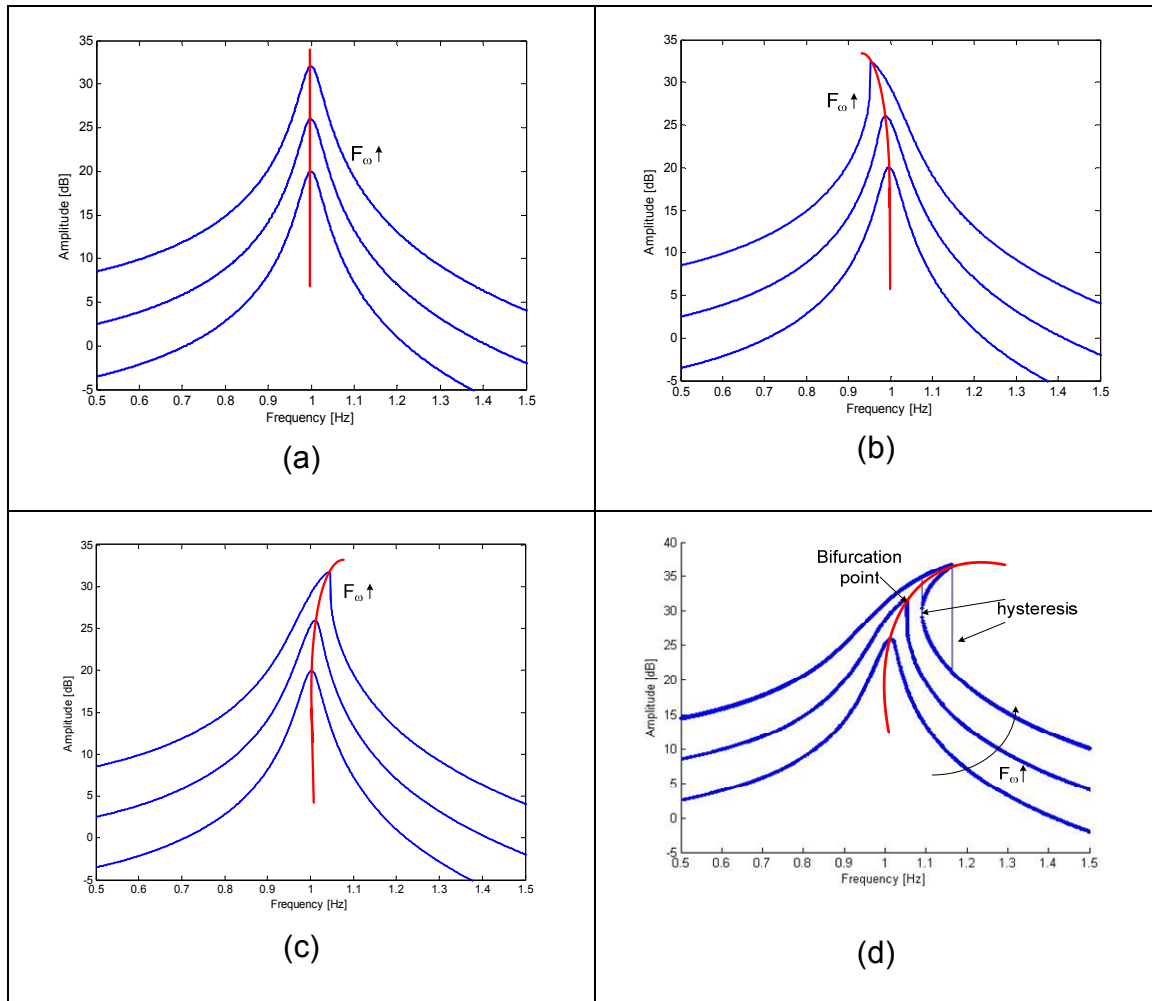


Figure 4.3 The amplitude-frequency response of (a) a linear resonator; (b) a nonlinear resonator that has a negative frequency shift; (c) a nonlinear resonator that has a positive frequency shift; (d) a nonlinear resonator excited below and beyond the bifurcation points.

Beyond the bifurcation point, the frequency-amplitude plot shows hysteresis. In the hysteresis region, the amplitude is no more a single value function of exciting frequency. As a matter of fact, in a practical case, the system energy

does not allow sudden jump of amplitude from one value to another. Instead, the amplitude will gradually change. This amplitude ambiguity is the origin of chaotic behavior.

Chapter 5 MEMS oscillator and phase noise theory

This chapter forms the theoretical basis for the design of low noise MEMS oscillator. The existing oscillation structures of MEMS resonators are reviewed and their drawbacks analyzed. A novel automatic amplitude control structure is thus proposed for better temperature stability and phase noise control. To analyze the phase noise in a MEMS oscillator system, we first reviewed two of the most recognized phase noise models, the LTI model and the LTV model, with their limitations in analyzing a mechanical oscillator. Later on, a state-space analysis is performed on the nonlinear oscillator with the proposed AAC loop. Numerical simulation results are presented as well for verification.

5.1 MEMS oscillator and automatic amplitude control

A simple MEMS oscillator can be constructed using the circuit given in Fig. 5.1 [46]. The resonant beam needs to be polarized at V_p . At motion, the resonant beam produces a motion current at one electrode. This current is sensed and fed back to the other electrode or through a comparator [47] to generate an electrostatic force. If the gain and phase criterion is satisfied, the resonant beam will oscillate until its amplitude is eventually stabilized by the nonlinearities in the mechanical part or electrical part. The amplitude of this oscillator suffers from temperature and supply voltage variation and thus is limited to the low accuracy arena due to the amplitude caused frequency drift.

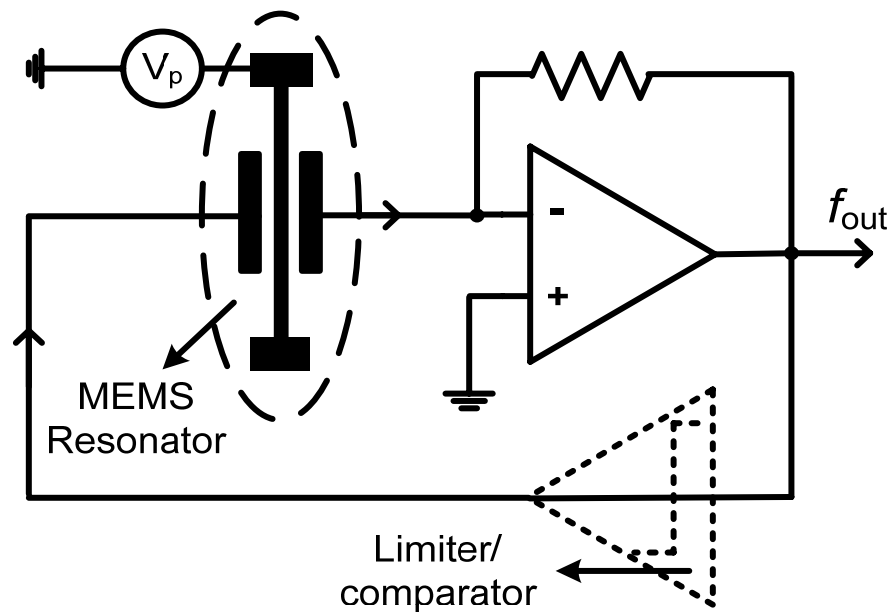


Figure 5.1 Schematic diagram of direct feedback MEMS oscillator

An automatic amplitude control (AAC) loop is introduced to avoid strong nonlinearity. The most widely used AAC structure (Fig. 5. 2) [5, 6, 9] adjusts the gain of the sense amplifier by replacing the feedback resistor with a MOSFET transistor operating in linear region. The amplitude of the oscillation signal at the sense amplifier output is detected and compared with a preset value. The amplified error signal is used to adjust the resistance of the MOSFET transistor. Once a stable oscillation is established, the feedback resistor will precisely match the effective resistance of the MEMS resonator. Therefore, the temperature drift of the effective resistance will cause the same drift in oscillation amplitude and in turn causes a frequency drift.

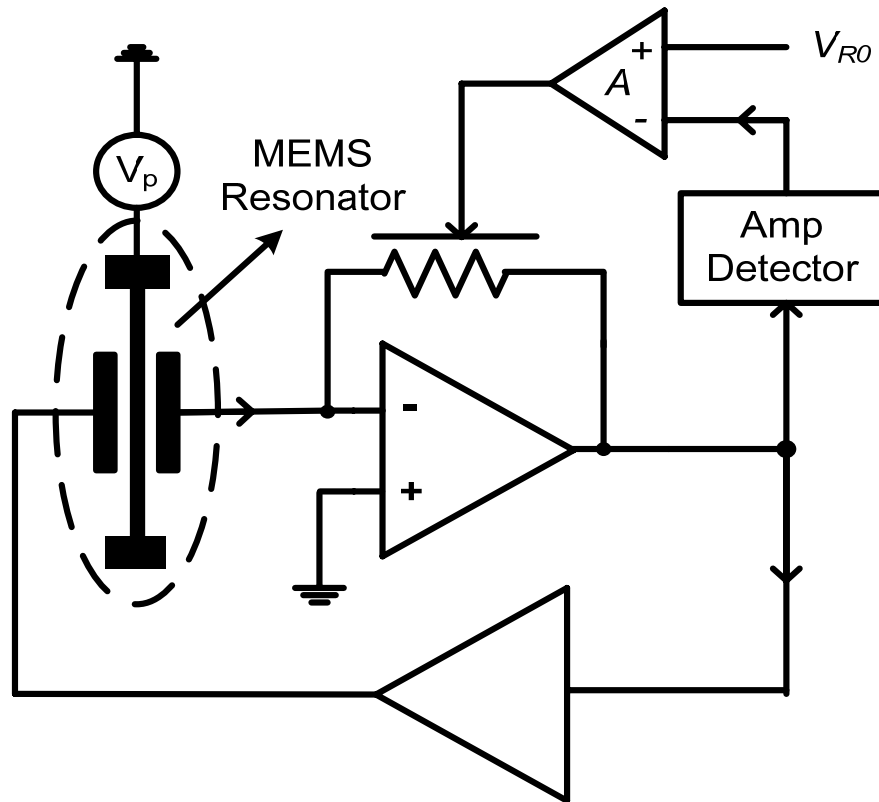


Figure 5.2 Schematic diagram of MEMS oscillator with AAC loop and gain control performed on the sense amplifier.

We propose a more temperature-robust AAC structure with a fixed gain amplifier and a linear variable gain amplifier (VGA) following it, as is shown in Fig. 5.3. The gain of the linear VGA is controlled by the difference between the oscillator amplitude and the present value, V_{R0} , through a loop filter $L(s)$.

The MEMS oscillators with AAC loop contains nonlinear building blocks such as amplitude detector, variable gain amplifier, and especially a nonlinear resonator, which prevent any ordinary linear analysis. To give the reader a better understanding our own phase noise analysis, it is useful to briefly review the LTI model and the LTV model in the next section.

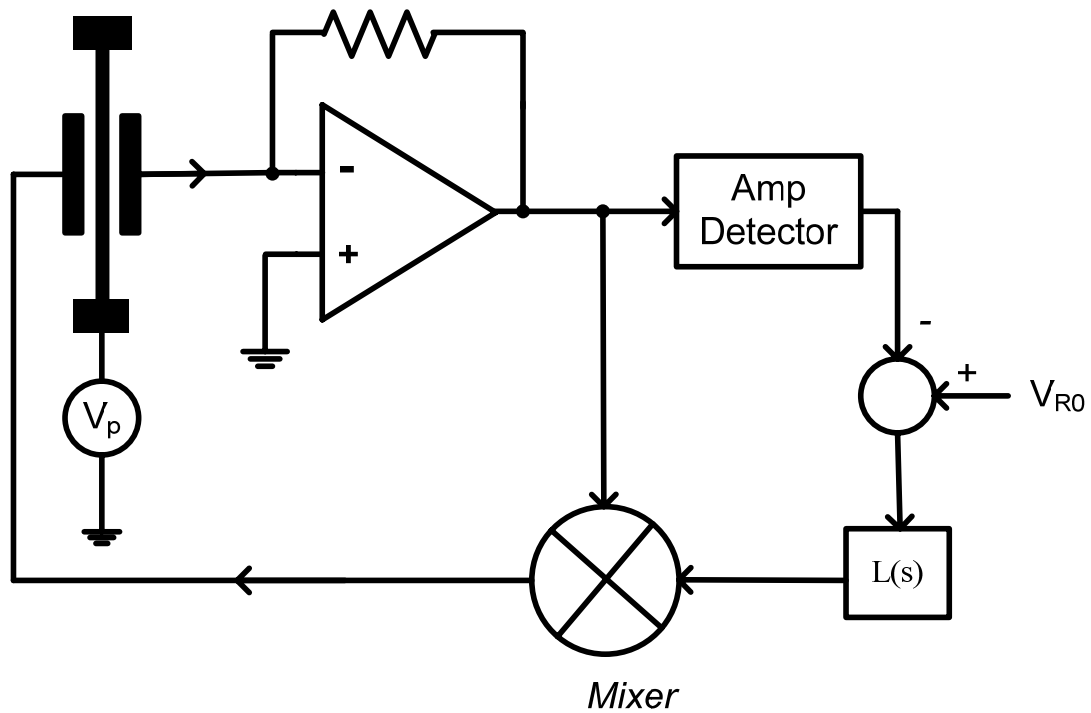


Figure 5.3 Oscillator structure with fixed gain sense amplifier and AAC performed on a separate linear VGA.

5.2 Existing phase noise theory

5.2.1 Phase noise basics

Ideally, the output of an oscillator may be expressed as $y(t) = A \cos(\omega_0 t + \phi)$, where A is the amplitude, and ω_0 is the frequency. In practice, however, the amplitude A and the phase offset ϕ are functions of time. Ignoring the waveform distortion, the output can be thus given by

$$y(t) = A(t) \cos[\omega_0 t + \phi(t)] \quad (5.1)$$

and further decomposed into

$$\begin{aligned}
y(t) &= A(t) \cos[\omega_0 t + \phi(t)] \\
&= A_0[1 + \delta(t)] \cos[\omega_0 t + \phi(t)] \\
&\approx A_0[\cos(\omega_0 t) + \delta(t) \cos \omega_0 t + \phi(t) \sin \omega_0 t]
\end{aligned} \tag{5.2}$$

The above equation indicates that the amplitude variation is actually caused by the in-phase component, while the phase variation is actually caused by the quadrature component, with referred to the ideal oscillation $\cos(\omega_0 t)$. The marking of noise in the time-domain with referred to the oscillation waveform is the key to understand the dynamics of an oscillator.

The amplitude noise and phase noise produces noise sidebands around the oscillation frequency. In a practical oscillator, the noise in $A(t)$ will be reduced by an amplitude limiting mechanism like saturation, or eliminated by the application of a limiter to the output signal, whereas the noise in $\phi(t)$ won't be affected and will accumulate over-time. Thus the noise sideband is dominated by the phase portion, known as phase noise.

5.2.2 Linear time-invariant model

The linear time-invariant (LTI) model was derived from a linear frequency-domain transfer function [48-50]. Take a simple feedback system shown in Fig. 5.4 as an example. $N(s)$ represents a noise source, and $H(s)$ is the frequency selection tank. If at frequency ω_0 , the phase-shift across $H(s)$ precisely matches 360° and the loop gain across $H(s)$ matches unity, the closed-loop transfer function

$$\frac{Y}{N}(j\omega) = \frac{H(j\omega)}{1 - H(j\omega)} \quad (5.3)$$

goes to infinity, thus an oscillation at ω_0 will build up until limited by some mechanisms. Suppose the oscillation frequency ω slightly deviates from ω_0 , $\omega = \omega_0 + \Delta\omega$, the phase shift deviates from 360° or the loop gain deviates from the unity, thus its noise transfer function can be approximated as

$$\begin{aligned} \frac{Y}{N}[j(\omega_0 + \Delta\omega)] &= \frac{H(j\omega_0 + j\Delta\omega)}{1 - H(j\omega_0 + j\Delta\omega)} \\ &= \frac{H(j\omega_0) + \Delta\omega \cdot dH/d\omega}{1 - H(j\omega_0) - \Delta\omega \cdot dH/d\omega} \end{aligned} \quad (5.4)$$

Since $H(j\omega_0) = 1$ and for most practical cases $|\Delta\omega \cdot dH/d\omega| \ll 1$, Eq. (5.4) reduces to

$$\frac{Y}{N}[j(\omega_0 + \Delta\omega)] = \frac{-1}{\Delta\omega \cdot dH/d\omega} \quad (5.5)$$

This equation indicates that a noise component at $\omega = \omega_0 + \Delta\omega$ is multiplied by $(\Delta\omega \cdot dH/d\omega)^{-1}$ when it appears at the output of the oscillator. In other words, the noise power spectral density is shaped by

$$\left| \frac{Y}{N}[j(\omega_0 + \Delta\omega)] \right|^2 = \frac{1}{(\Delta\omega)^2 |dH/d\omega|^2} \quad (5.6)$$

To gain more insight, let $H(j\omega) \approx A(\omega)\exp[j\Phi(\omega)]$, and hence

$$\frac{dH}{d\omega} = \left(\frac{dA}{d\omega} + jA \frac{d\Phi}{d\omega} \right) \exp(j\Phi) \quad (5.7)$$

Since for $\omega \approx \omega_0$, $A \approx 1$, Eq. (5.6) can be written as

$$\left| \frac{Y}{N}[j(\omega_0 + \Delta\omega)] \right|^2 = \frac{1}{(\Delta\omega)^2 [(dA/d\omega)^2 + (d\Phi/d\omega)^2]} \quad (5.8)$$

With the quality factor generally defined as [49]

$$Q = \frac{\omega_0}{2} \sqrt{\left(\frac{dA}{d\omega}\right)^2 + \left(\frac{d\Phi}{d\omega}\right)^2} \quad (5.9)$$

Eq. (5.8) is reduced to

$$\left| \frac{Y}{N} [j(\omega_0 + \Delta\omega)] \right|^2 = \frac{1}{4Q^2} \left(\frac{\omega_0}{\Delta\omega} \right)^2 \quad (5.10)$$

The output noise can be equally divided into phase and amplitude fluctuations with referred to the output oscillation. Taking only phase fluctuation into account yields

$$\left| \frac{Y_p}{N} [j(\omega_0 + \Delta\omega)] \right|^2 = \frac{1}{8Q^2} \left(\frac{\omega_0}{\Delta\omega} \right)^2 \quad (5.11)$$

Because of the linear assumption and the stationary noise source assumption, the LTI phase noise model provides important qualitative design insights but is limited in its quantitative predictive ability. For example, the measured phase noise usually follows a $1/f^3$ behavior at close-in region, and flats out at a large frequency offset.

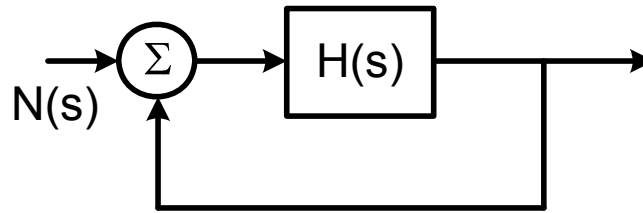


Figure 5.4 A linear oscillator system

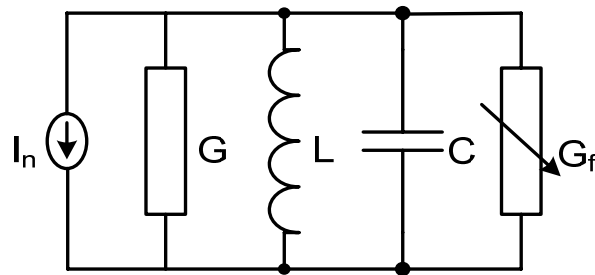
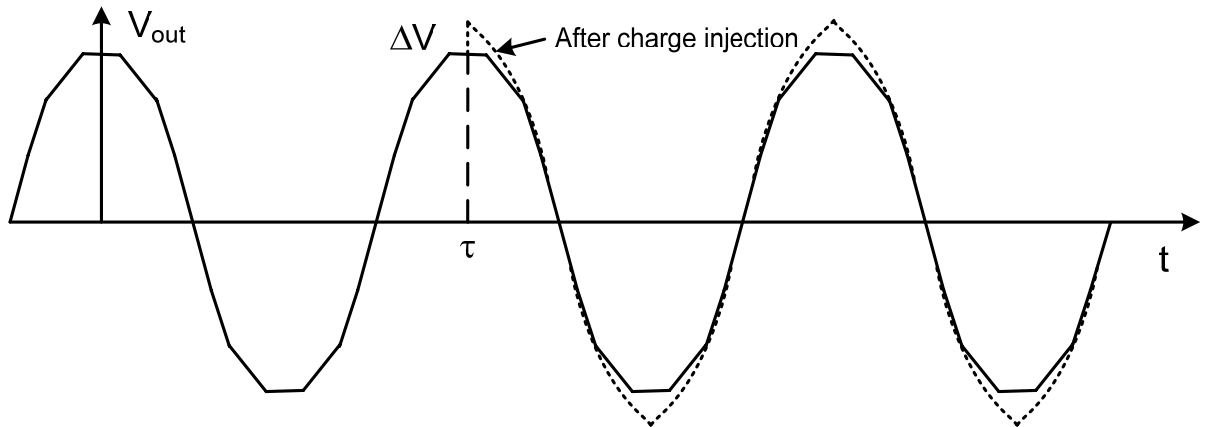


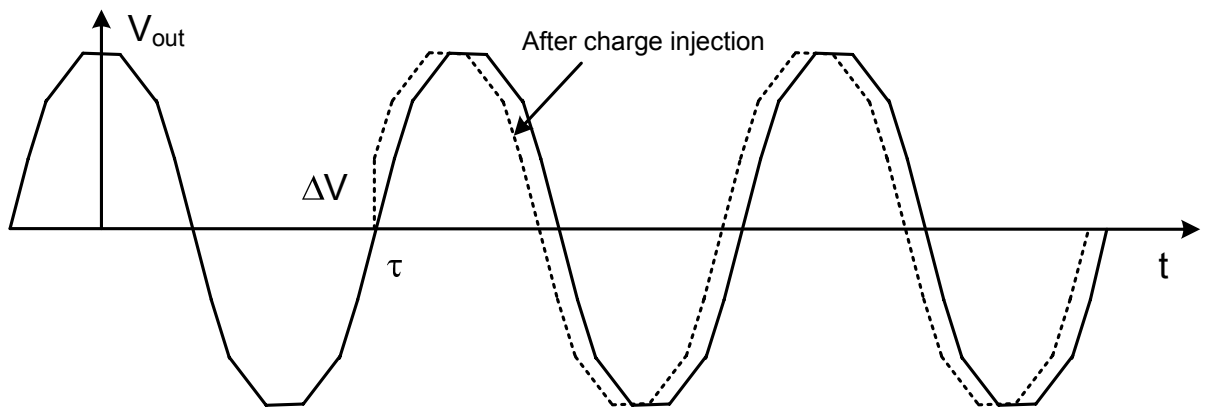
Figure 5.5 LC oscillator showing charge injection

5.2.3 Linear time-variant model

The Linear time-variant (LTV) model was proposed by A. Hajimiri and T. H. Lee [51] to include the omnipresent nonlinearity in a linear model. This model can be explained using a LC oscillator shown in Fig. 5.5 as an example. Assume a charge injection occurs when the oscillator is oscillating at a steady state. It can be seen from Fig. 5.6 that the resultant amplitude and phase change is time dependent. In particular, if the charge is applied at the peak of the voltage across the capacitor, the oscillation amplitude will increase, as shown in Fig. 5.6(a). Assuming that an amplitude change does not affect the oscillation frequency, the timing of the zero crossings (or phase) won't be affected in this case. On the other hand, if this impulse is applied at the zero crossing, it affects the zero-crossing but has negligible effect on the amplitude, as shown in Fig. 5.6(b).



(a)



(b)

Figure 5.6 Impulse response of LC oscillator

Based on the above observation, an impulse sensitivity function (ISF) $\Gamma(x)$, as a function of when the injection takes place, can be derived. The phase change with response to an impulse input is thus given by

$$h_{\Phi}(t, \tau) = \frac{\Gamma(\omega_0 \tau)}{q_{\max}} u(t - \tau) \quad (5.12)$$

where $u(t)$ is the unit step function, q_{\max} is the maximum charge displacement across the capacitor, and $\Gamma(x)$ is the impulse sensitivity function and is a dimensionless periodic function with a period of 2π . Fig. 5.7 shows the ISF for an LC oscillator, which has its maximum value near the zero crossings of the oscillation, and a zero value at the peak of the oscillation waveform. The phase shift of the oscillator caused by a current perturbation $i(t)$ is thus given in the block diagram shown in Fig. 5.8.

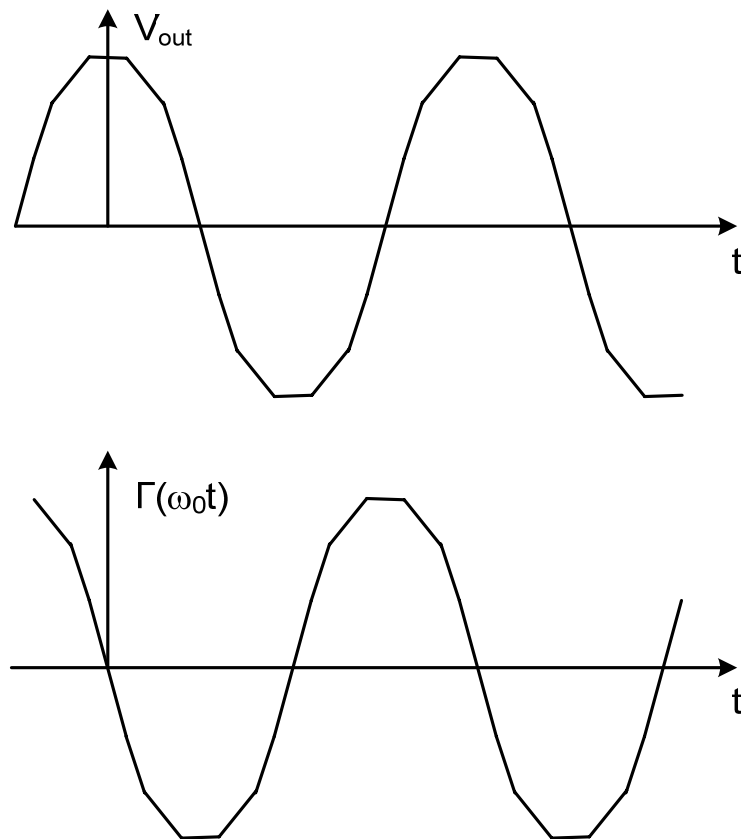


Figure 5.7 Waveform and ISF for a LC oscillator

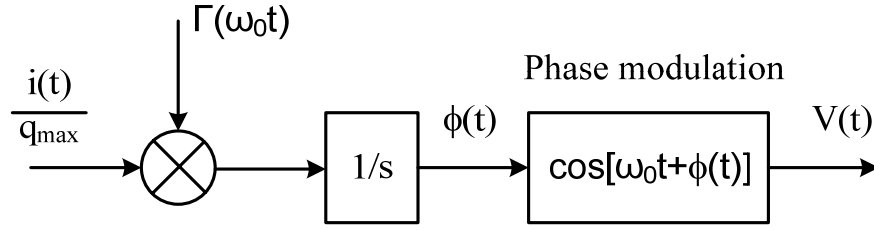


Figure 5.8 The equivalent block diagram of the LTV model

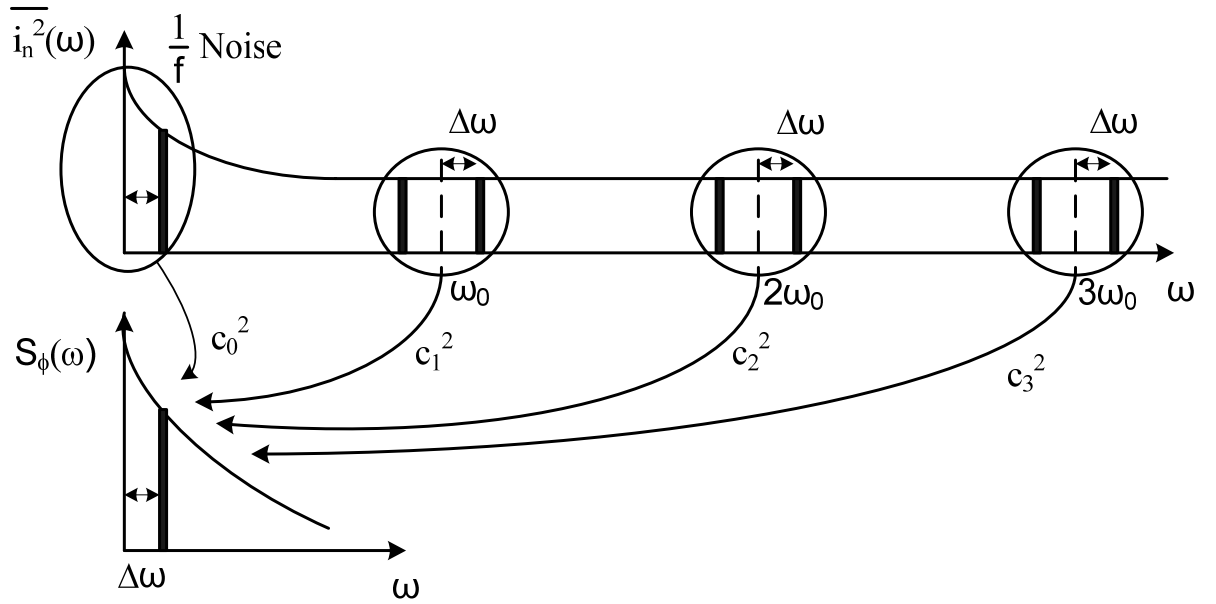


Figure 5.9 Noise folding due to ISF decomposition

$\Gamma(x)$ can be expressed as a Fourier series

$$\Gamma(\omega_0 \tau) = \frac{c_0}{2} + \sum_{n=1}^{\infty} c_n \cos(n\omega_0 \tau + \theta_n) \quad (5.13)$$

where θ_n is the phase of the n th harmonic of the ISF. Fig. 5.9 explains how the noise folding happens in an oscillator. Note that $1/f^3$ noise is caused by the

upconversion of $1/f$ noise through the coefficient c_0 . Since c_0 is the dc value of the ISF, $1/f^3$ phase-noise can be greatly reduced by the proper ISF design, through adjustment of the rise- and fall-time symmetry.

5.2.4 Limitation of LTV model

At the first glance it looks that the LTV model well solves the nonlinearity associated with an oscillator. But this theory is derived from an implicit assumption that the frequency does not change with amplitude variation. Take a clamped-clamped beam micro resonator as an example, whose restoration force is given by

$$F_r = -k_0x - k_2x^3 \quad (5.14)$$

Due to the missing of first order nonlinear correction term k_1x^2 , an oscillator made from it outputs fully symmetrical waveform. Hence, c_0 , the dc value of the ISF, is zero, which predicts no $1/f^3$ phase noise in the close-in region. The measured phase noise, however, exhibits strong $1/f^3$ phase noise [5]. In this case, the oscillation frequency is actually a function of amplitude, making the assumption of unchanging frequency and step function invalid.

5.3 State-space theory

Analyzing phase noise in the state space is not a new idea. To the author's acknowledgement, a unifying phase noise model proposed by Kaertner and Demir [60-63] belongs to this category. In this model, the noise perturbation is

decomposed into orbital and phasal components along the Floquet vectors in the state-space, and models the phasal perturbation as a diffusion problem. The soundness of this model is verified in numerical simulators [64-65]. In addition, the oscillation envelop can also be predicted by employing this model [66]. However, due to the complexity in mathematics, this model fails to arrive at a closed-form solution based on the circuit or device parameters. To guide the oscillator design process, we combine the mathematical soundness of state-space approach and the understandability of Hajimiri's approach in our model. Our model is different from Kaertner and Demir's model in that the orbital component still influences the phase.

5.3.1 Unperturbed oscillator trajectory in state-space

To gain insight into the origin of phase noise, the dynamics of a nonlinear oscillator with automatic amplitude control is studied via the state-space approach. The analysis is performed in the mechanical domain for simplicity.

With a nonlinear spring force $F = -k_0x - k_1x^2 - k_2x^3$, the motion of a second-order spring-mass-damping resonator is given by its state-space equation:

$$\begin{aligned} \frac{dy}{dt} &= \frac{d}{dt} \begin{bmatrix} y_1 \\ y_2 \end{bmatrix} = \frac{d}{dt} \begin{bmatrix} x \\ \dot{x} \end{bmatrix} \\ &= \begin{bmatrix} \dot{x} \\ -\frac{k_0}{m}x - \frac{k_1}{m}x^2 - \frac{k_2}{m}x^3 - \frac{\eta_0}{m}\dot{x} \end{bmatrix} + \frac{1}{m} \begin{bmatrix} 0 \\ F_{fb} \end{bmatrix} \end{aligned} \quad (5.15)$$

where F_{fb} is the excitation force or feedback force applied to the resonator. A feedback mechanism observes the velocity \dot{x} and applies a force F_{fb} which is

proportional to the observed velocity. The feedback gain is finely adjusted to η_0 so that the mechanical loss $\eta_0 \dot{x}$ is exactly balanced by the feedback force F_{fb} , as is given by

$$\begin{aligned} \frac{dy}{dt} = \frac{d}{dt} \begin{bmatrix} x \\ \dot{x} \end{bmatrix} &= \begin{bmatrix} \dot{x} \\ -\frac{k_0}{m}x - \frac{k_1}{m}x^2 - \frac{k_2}{m}x^3 - \frac{\eta_0}{m}\dot{x} \end{bmatrix} \\ + \frac{1}{m} \begin{bmatrix} 0 \\ \eta_0 \dot{x} \end{bmatrix} &= \begin{bmatrix} \dot{x} \\ -\frac{k_0}{m}x - \frac{k_1}{m}x^2 - \frac{k_2}{m}x^3 \end{bmatrix} = f(y) \end{aligned} \quad (5.16)$$

Eq. (5.16) has a periodic solution $y_0(t) = (x_0(t), \dot{x}_0(t))$ plotted in the state-space plane (Fig. 5.10) where the position $x_0(t)$ is plotted against velocity $\dot{x}_0(t)$. The solution forms a closed curve, or unperturbed trajectory. Since the mechanical loss is fully compensated, the unperturbed trajectory follows an orbit that has a fixed energy E given by

$$\begin{aligned} E &= \frac{1}{2}m\dot{x}^2 + \int k(x)xdx \\ &= \frac{1}{2}m\dot{x}^2 + \frac{1}{2}k_0x^2 + \frac{1}{3}k_1x^3 + \frac{1}{4}k_2x^4 \end{aligned} \quad (5.17)$$

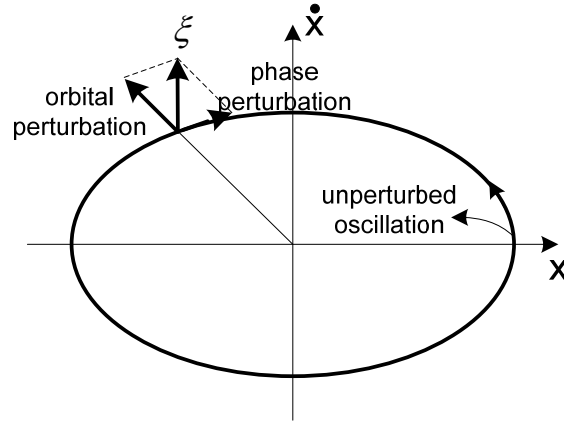


Figure 5.10 Unperturbed oscillation trajectory $y_0(t)$ and perturbation decomposition.

5.3.2 Velocity observation noise and gain variation

The noise introduced in the sense amplifier and the driving buffer can be simplified as a velocity observation noise N_v . The feedback gain may not precisely match η_0 all the time, which is modeled as a feedback gain variation $\Delta\eta$. The velocity observation noise and the gain variation are included in the macro model of a second order nonlinear oscillator, as shown in Fig 5.11.

The describing function of the oscillator shown in Fig. 5.11 is thus given by

$$\frac{dy}{dt} = f(y) + \begin{bmatrix} 0 \\ \frac{\Delta\eta\dot{x}}{m} + \frac{\eta_0 N_v}{m} \end{bmatrix} = f(y) + \xi \quad (5.18)$$

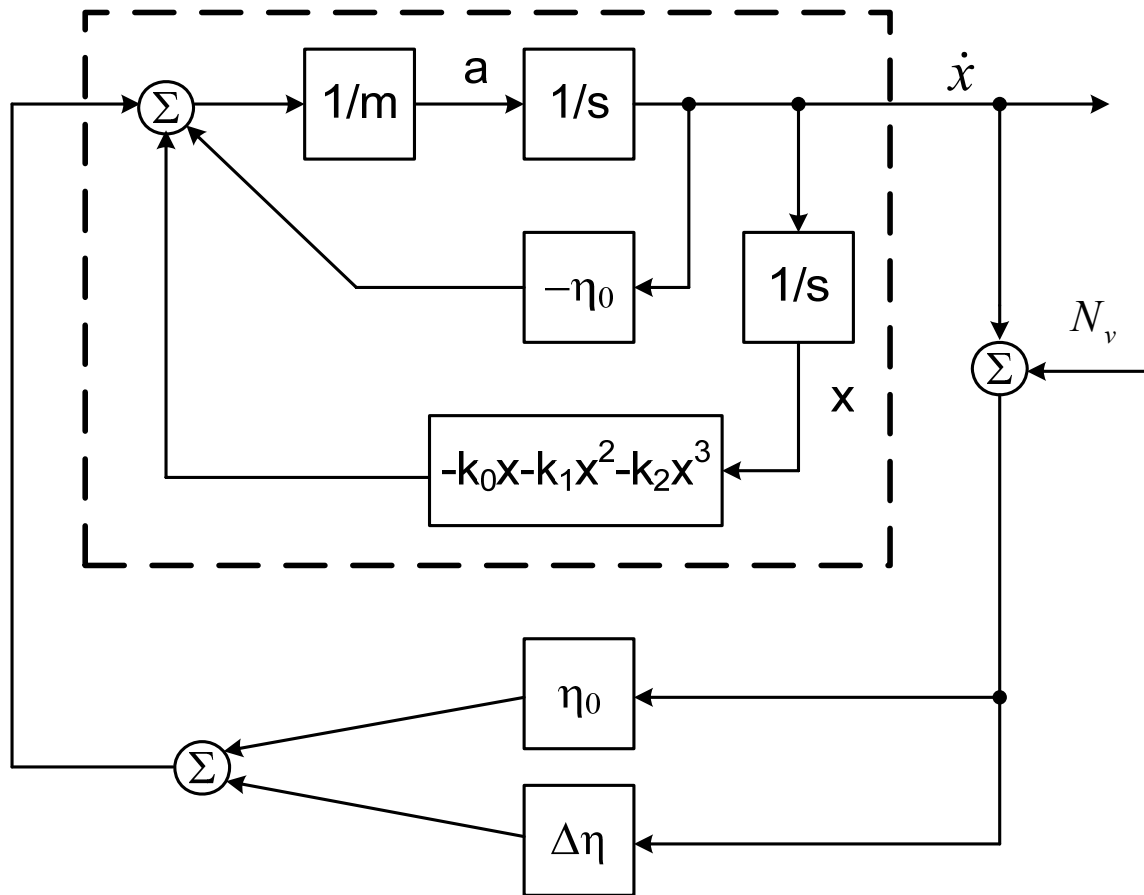


Figure 5.11 Macro model of second order nonlinear oscillator with noise in the observed velocity and feedback gain. Inside the dash box is the macro model of nonlinear resonator

5.3.3 Orbital and phase perturbation

Let's use Fig. 5.10 to study the influence of ξ over the motion trajectory. We noticed that, in an unperturbed trajectory, the vector (x, \dot{x}) is a monotonic function of time (within a period). Therefore, phase can be uniquely defined by

the vector (x, \dot{x}) , for any unperturbed trajectory with different orbit. Therefore, if the trajectory is perturbed by a component proportional to $y = (x_0, \dot{x}_0)$, the phase will remain fixed but the orbit will change. On the contrary, a perturbation in parallel with $f(y)$ is not going to change the motion trajectory (or orbit), but will change the speed of cycling and hence affect the phase (refer to Eq. 5.16). Therefore, the perturbation ξ can be decomposed into an orbital perturbation that is parallel to y , and a phase perturbation that is in parallel to $f(y)$, as shown in Fig. 5.10.

$$\begin{aligned}\xi &= [f(y), 0][f(y), y]^{-1}\xi + [0, y][f(y), y]^{-1}\xi \\ &= \{f(y)[1 \quad 0][f(y), y]^{-1} \begin{bmatrix} 0 \\ 1 \end{bmatrix} + y[0 \quad 1][f(y), y]^{-1} \begin{bmatrix} 0 \\ 1 \end{bmatrix}\} \end{aligned} \quad (5.19)$$

$$\left(\frac{\Delta\eta\dot{x}}{m} + \frac{\eta_0 N_v}{m}\right) = [\Gamma(y)f(y) + H(y)y] \left(\frac{\Delta\eta\dot{x}}{m} + \frac{\eta_0 N_v}{m}\right)$$

where

$$\begin{aligned}\Gamma(y) &= [1 \quad 0][f(y), y]^{-1} \begin{bmatrix} 0 \\ 1 \end{bmatrix} \\ &= \frac{-mx}{m\dot{x}^2 + (k_0x^2 + k_1x^3 + k_2x^4)} = \frac{-mx}{2E + (k_1x^3/3) + (k_2x^4/2)},\end{aligned}$$

$$\begin{aligned}H(y) &= [0 \quad 1][f(y), y]^{-1} \begin{bmatrix} 0 \\ 1 \end{bmatrix} \\ &= \frac{m\dot{x}}{m\dot{x}^2 + (k_0x^2 + k_1x^3 + k_2x^4)} = \frac{m\dot{x}}{2E + (k_1x^3/3) + (k_2x^4/2)}.\end{aligned}$$

Combine Eq. (5.18) and (5.19) yields

$$\begin{aligned}\frac{dy}{dt} &= [1 + \left(\frac{\Delta\eta\dot{x}}{m} + \frac{\eta_0 N_v}{m}\right)\Gamma(y)]f(y) \\ &\quad + \left(\frac{\Delta\eta\dot{x}}{m} + \frac{\eta_0 N_v}{m}\right)H(y)y\end{aligned} \quad (5.20)$$

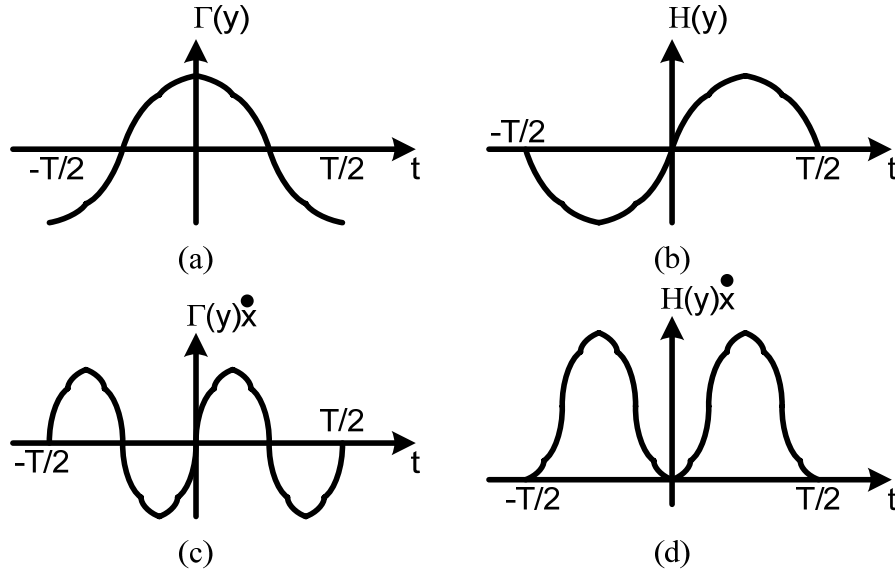


Figure 5.12 Illustration of $\Gamma(y)$, $H(y)$, $\dot{x}\Gamma(y)$ and $\dot{x}H(y)$.

The term $(\frac{\Delta\eta\dot{x}}{m} + \frac{\eta_0 N_v}{m})\Gamma(y)$ determines the fractional timing shift due to the phase perturbation, while the term $(\frac{\Delta\eta\dot{x}}{m} + \frac{\eta_0 N_v}{m})H(y)$ determines the fractional orbital shift due to the orbital perturbation. Fractional timing shift refers to the timing shift divided by the unperturbed oscillation period T , while fractional orbital shift refers to the energy change divided by the unperturbed energy. Since the energy change is very small, the fractional orbital shift can be approximated as $\Delta x / X_0$, where Δx is the amplitude change and X_0 is the unperturbed oscillation amplitude.

5.3.4 Cycling speed correction factor

Besides the phase perturbation, the orbital change will cause an additional phase change due to the A-S effect, as is indicated in Eq. (4.21). The oscillation

period T is actually a function of the oscillation amplitude X_0 . Within a narrow band of the orbit

$$\begin{aligned} T &= \frac{2\pi}{\omega} = \frac{2\pi}{\omega_0(1+\lambda X^2)} = \frac{2\pi}{\omega_0[1+\lambda(X_0+\Delta x)^2]} \\ &\approx \frac{2\pi}{\omega_0(1+\lambda X_0^2)} \left(1 - \frac{2\lambda X_0}{1+\lambda X_0^2} \Delta x\right) = T'_0(1-c\Delta x) \end{aligned} \quad (5.21)$$

where X_0 is the amplitude of unperturbed oscillation, T'_0 is the unperturbed period, T is the perturbed period at amplitude X , and c equals to $2\lambda X_0/(1+\lambda X_0^2)$. The net timing shift is the result of both the phase perturbation and the orbital perturbation. Taking both of them into account, we have a cycling speed correction factor

$$CF = \left(\frac{\Delta\eta\dot{x}}{m} + \frac{\eta_0 N_v}{m}\right)\Gamma(y) + c\delta(t)X_0 \quad (5.22)$$

Where $\delta(t)$ is the fractional orbital shift. In Eq. (5.22), the first part is caused by the phase perturbation, while the second part is caused by the orbital shift. Therefore, the equivalent model for a perturbed free running nonlinear oscillator is plotted in Fig. 5.12, with $\delta(t)$ representing the fractional orbital shift, and $\varphi(t)$ representing the fractional phase shift. The perturbed oscillator has an output $[1+\delta(t)]y_0\{[1+\varphi(t)]t\}$, where $y_0(t)$ is the unperturbed oscillation from Eq. (5.17).

The observed velocity noise N_v is transformed by $H(y)$ into a normalized orbital perturbation N_1 and by $\Gamma(y)$ into a normalized phase perturbation N_2 . This transformation is similar to the phase and orbital decomposition in the linear time-invariant (LTI) model. If the nonlinear spring term k_1 and k_2 does not exist, $H(y)$ and $\Gamma(y)$ will degenerate to sinusoidal functions, and N_1 and N_2 will be equally

split, which agrees well with the LTI model. Fig. 5.12 illustrate $\Gamma(y)$, $H(y)$, $\dot{x}\Gamma(y)$ and $\dot{x}H(y)$ as a function of time.

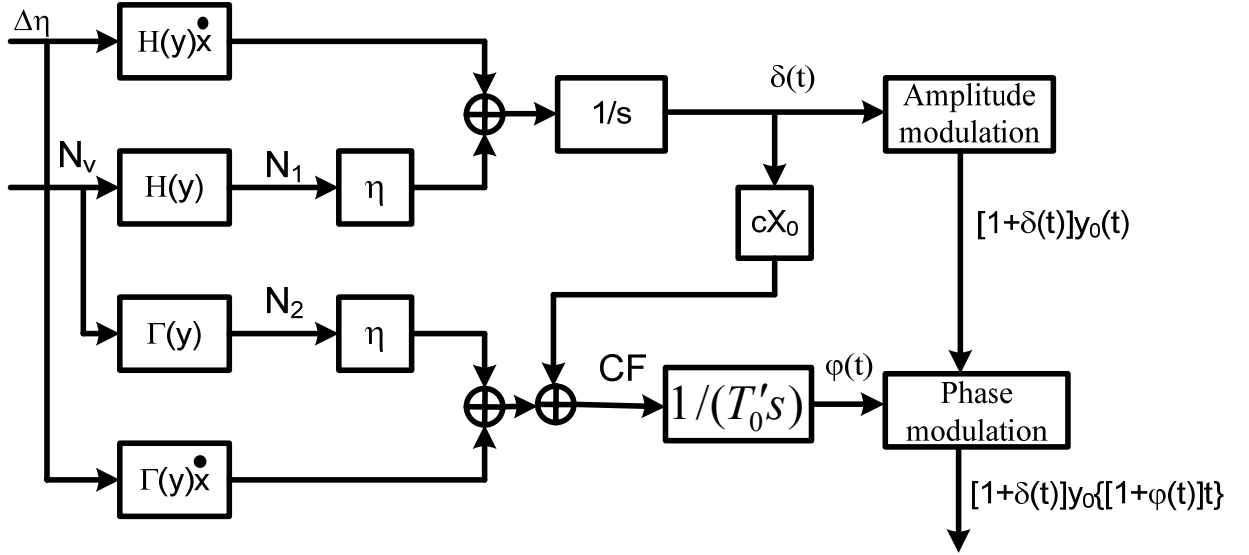


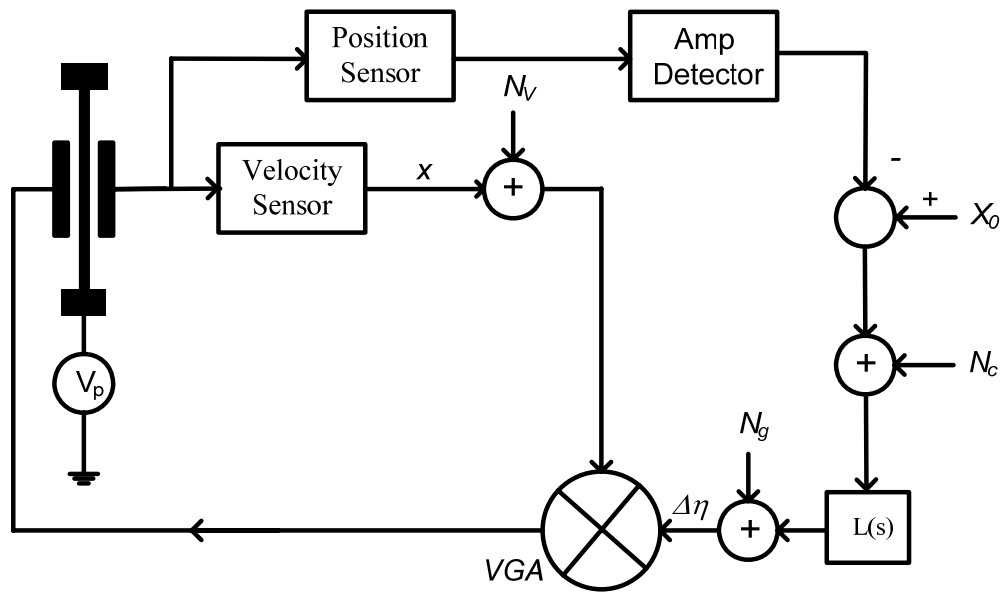
Figure 5.13 Equivalent models of a perturbed free running nonlinear oscillator described by Equation 5.18

5.3.5 Amplitude limiting-Automatic amplitude control (AAC)

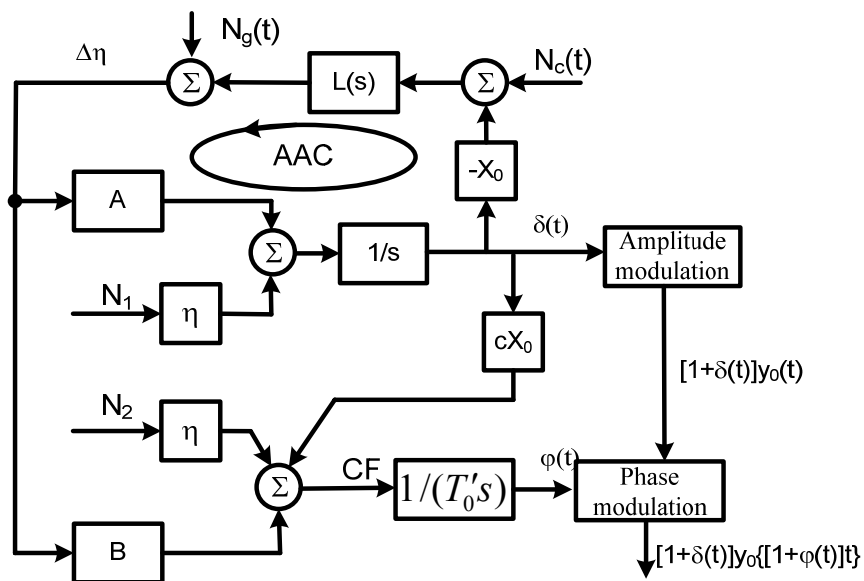
If the oscillator is free of any amplitude limiting mechanism, the orbital perturbation will be integrated and result in an unbounded orbital shift. Such an undesirable unbounded shift is avoided by employing the proposed automatic amplitude control. The following analysis is performed on the oscillator with an ideal position sensor, an ideal velocity sensor and an AAC loop, as is shown in Fig. 5.14(a) Here the orbital position is identified by the oscillation amplitude X . The detected oscillation amplitude X is compared with a preset value, X_0 . Their

difference is fed to the AAC loop filter $L(s)$ to produce the gain perturbation signal

$\Delta\eta$.



(a)



(b)

Figure 5.14 (a) Nonlinear MEMS oscillator with ideal position and velocity sensor and AAC loop; and (b) its equivalent linear model.

Inside the AAC loop, the amplitude detection introduces extra noise which is modeled as $N_c(t)$ and the variable gain amplifier has a input referred noise $N_g(t)$ at the gain control node (Fig. 5.14(a)). Assume that the amplitude control loop responds much slower than the oscillation itself, $\dot{x}\Gamma(y)$ and $\dot{x}H(y)$ can be replaced with their average values for simplicity, as is given below

$$A = \frac{1}{T} \int_0^T \dot{x}H(y)dt \quad B = \frac{1}{T} \int_0^T \dot{x}\Gamma(y)dt \quad (5.23)$$

Fig. 5.14(b) shows the derived linear equivalent model for this ideal nonlinear MEMS oscillator. The transfer function of the fractional orbital fluctuation is given by

$$\Delta(s) = \frac{[\eta_0 N_1(s) + AN_g(s) + AN_c(s)L(s)]/s}{1 + AX_0L(s)/s} \quad (5.24)$$

In the derived linear model, it is interesting to note that the AAC loop features the same integrator as is in the derived model for a linear LC oscillator [52], which reminds us of the similarity between the AAC loop and the phase-locked loop (PLL). Without the negative feedback of the AAC loop, the orbit shift will build up exactly in the same way as the phase difference between two frequencies does. Therefore, the same loop filter design strategy used in PLL can be applied directly to the AAC loop. A 2^{nd} order loop filter borrowed from the charge-pump PLL [53] can satisfy both the noise shaping and stability requirement, as is given below

$$L(s) = \frac{L_0(s/\omega_z + 1)}{s(s/\omega_p + 1)} \quad (5.25)$$

5.3.6 Phase noise discussion

The transfer function of the fractional phase fluctuation is given by

$$\begin{aligned}\Phi(s) &= (\eta_0 N_2 + \Delta(s)cX_0 + \Delta\eta(s)B)/(T'_0 s) \\ &= (\eta_0 N_2 + \Delta(s)cX_0 + \frac{N_g(s) + N_c(s)L(s)}{1 + AX_0 L(s)/s} B)/(T'_0 s)\end{aligned}\quad (5.26)$$

Three phase noise sources are identified in Eq. (4.26). $\eta_0 N_2 / T'_0 s$ is caused by the normalized phase perturbation, corresponding to the linear phase noise in LTI model. $\Delta(s)cX_0 / T'_0 s$ is caused by the orbital fluctuation through the A-S effect, which aliases the $1/f$ noise component in $\delta(t)$ into $1/f^3$ phase noise. It looks from the last term $\Delta\eta(s)B/(T'_0 s)$ that an extra phase noise is caused by the feedback gain variation through the asymmetry of the oscillation waveform. However, we found through simulation that B is so small that can be practically ignored even though an asymmetrical waveform is produced by the first nonlinear correction term $k_1 x^2$.

So far, we have proved that as long as the unperturbed trajectory forms a closed trajectory, the amplitude noise as well as the phase noise from a nonlinear mechanical oscillator can be still studied using a linear model. Therefore, the oscillation amplitude should only be constrained by the hard limits such as material, structure, or supply voltage, providing that the circuit design ensures a noiseless AAC loop.

At frequency close to dc, the orbital fluctuation

$$\Delta(s) \approx \frac{\eta N_1(s)}{AX_0 L(s)} + \frac{N_g(s)}{X_0 L(s)} + N_c(s) \quad (s \rightarrow 0) \quad (5.27)$$

Eq. (5.27) indicates that N_1 and N_g will be shaped by $L(s)$, but N_c will stay untouched. The suggested AAC loop filter has a high gain at dc to minimize the orbital fluctuation so that the phase noise can be minimized.

Since N_c will appear unattenuated in the orbital fluctuation at low frequencies, its $1/f$ noise component is the only source that gives rise to $1/f^3$ phase noise in the close-in region. Attention thus must be paid to design a low noise amplitude detector as well as a low noise error amplifier.

To use this model in a practical MEMS oscillator, proper scaling is required to accommodate the C/V and V/F conversion.

5.4 Numerical simulation

Simulink is used to numerically simulate the ideal nonlinear oscillator shown in Fig. 5.15. Two nonlinear resonators with normalized stiffness and resonant frequency are used in the simulation, as is given in Table 5.1. The quality factors are set to 1000 instead of hundreds of thousands in a practical case, due to the accuracy achievable with the simulation tool. The peak-frequency shifts caused by k_1 and k_2 are in the same amount, except that in resonator 1 both of them tilt to the same direction while in resonator 2 they completely cancel each other, as is shown in Fig. 5.15. For resonator 1, the oscillation amplitude is already far beyond the Duffing bifurcation point.

Table 5.1 parameters for the simulation setup

	Resonator 1	Resonator 2
m	$1/(4\pi^2)$	$1/(4\pi^2)$
k_0	1	1
k_1	0.1	0.1
k_2	-0.011111	0.011111
Q	1000	1000
X_0	2	2
X_b (bifurcation point) [8]	0.263	NA
f	0.9663	1

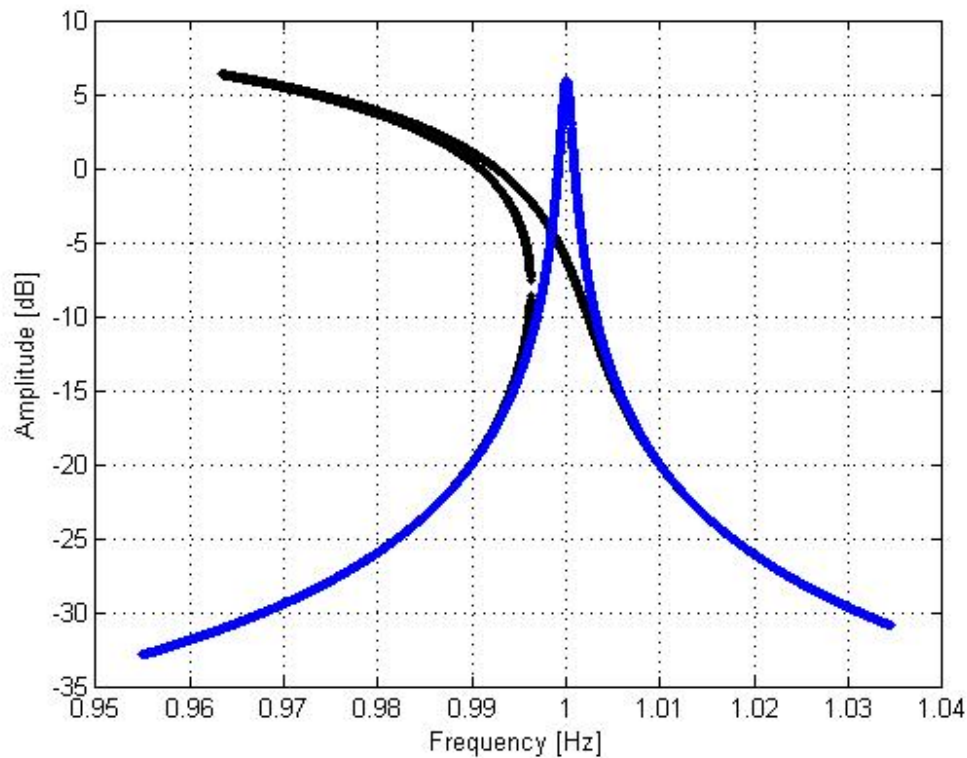


Figure 5.15 Amplitude-frequency responses of resonator 1 (black) and resonator 2 (blue) in Table 5.1.

Fig. 5.16 shows the state-space trajectories of the stable oscillations for resonator 1, resonator 2 and a linear resonator. Although the trajectories for oscillator 1 and oscillator 2 shows asymmetry against the oscillation amplitude x due to the first order nonlinear correction term, the waveforms should have symmetrical rising and falling time. Therefore, LTV model should yield a close result as LTI model.

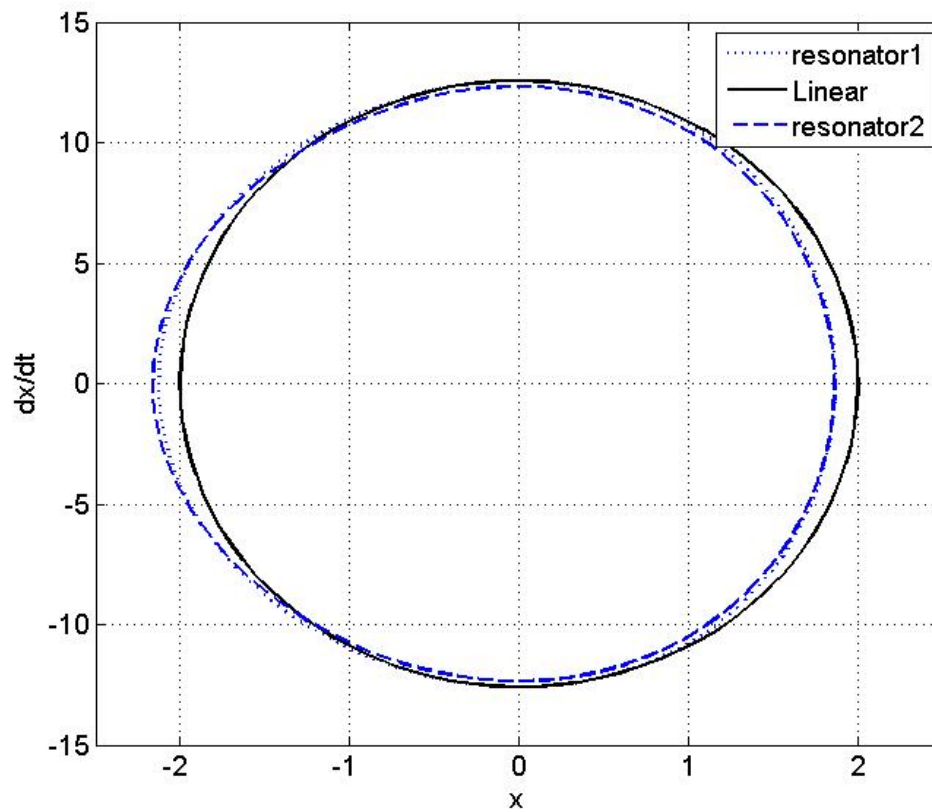


Figure 5.16 the state-space trajectories of the oscillator built from resonator 1, resonator 2 and an ideal linear resonator.

A two-tone test is employed to verify the linearity between a control signal at the AAC loop and the resulted phase change. The testing tones, f_1 (0.004rad/s) and f_2 (0.01rad/s), are injected at the amplitude comparison node. To remove the amplitude noise, the oscillation output is fed to an amplitude limiter. The simulated sideband spectrums after the amplitude limiter are shown in Fig. 5.17. For resonator 1, only two tones are clearly seen in the phase plot. The absent of an intermodulation tone indicates a perfect linear relationship. For resonator 2, no tone is seen at the desired frequency, indicating neither the A-S induced

phase shift nor asymmetry related phase shift exists.

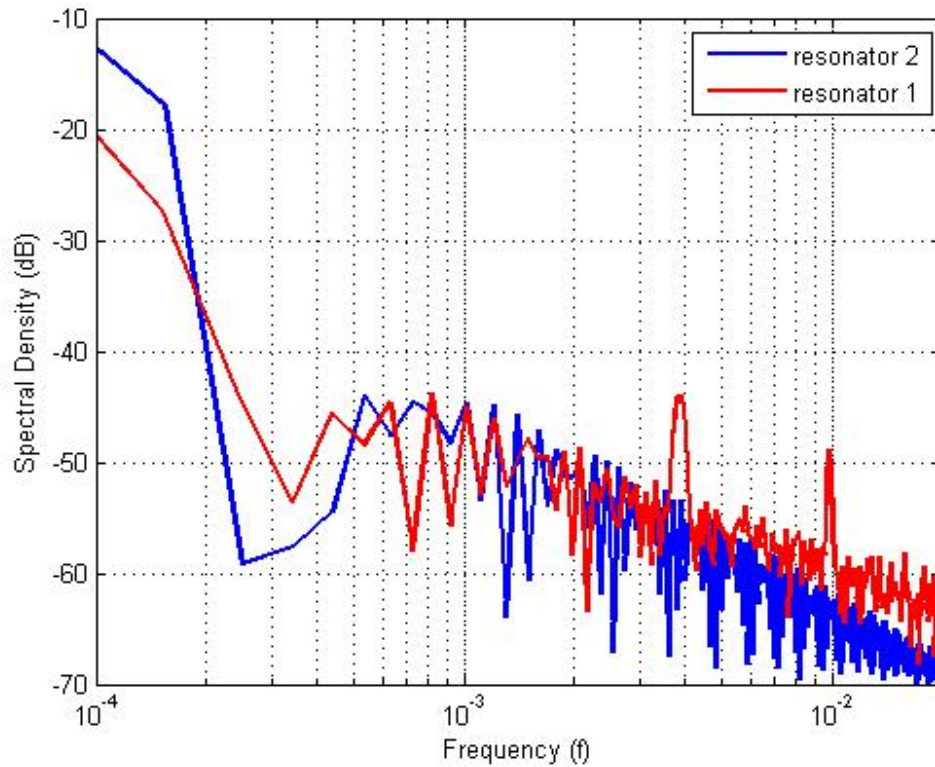


Figure 5.17 Simulated two-tone spectrum sidebands for resonator 1 and resonator 2.

To verify the quantitative prediction power of the proposed phase noise model, flicker noise is inserted at the amplitude comparison node in the oscillator based on resonator 1. Fig. 5.18 compares the simulated sideband spectrum with the LTI (and LTV) model and state-space model. The state-space model agrees well with the simulated spectrum, but the LTI model underestimate the resultant phase noise.

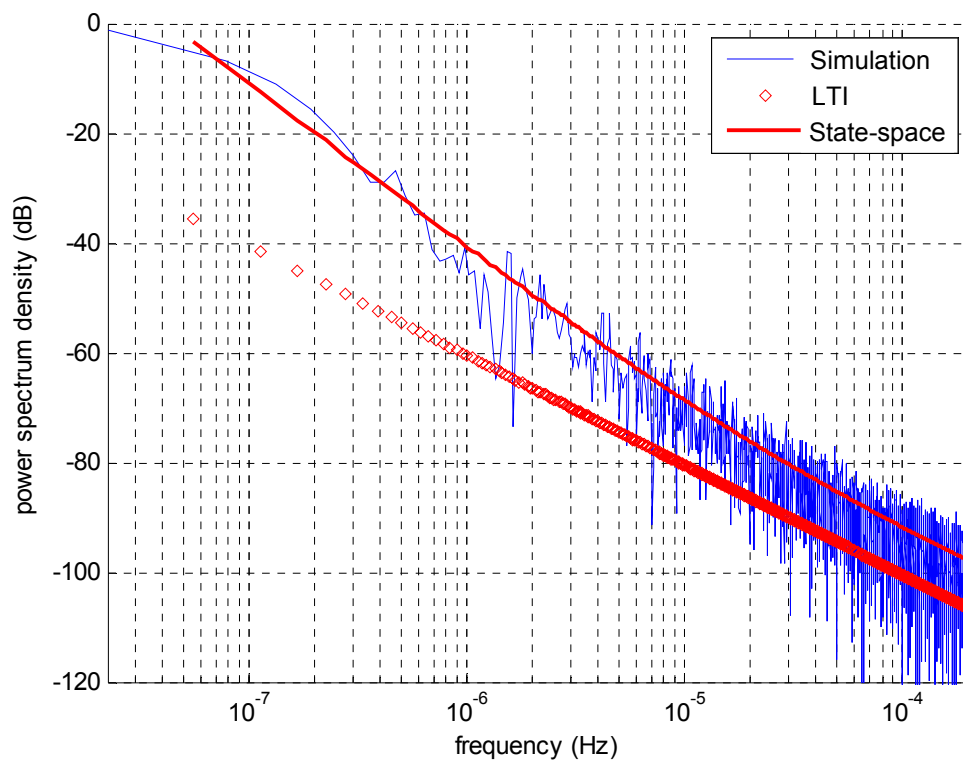


Figure 5.18 Simulated phase noise sideband versus LTI model and State-space model

Chapter 6 Circuit design

6.1 System overview

Based on the analysis in chapter 5, a readout system with a low-noise AAC loop for SOI resonant accelerometer is proposed and shown in Fig. 6.1. A switched-cap capacitive sense interface is used to detect the displacement of the resonant beam. A velocity signal is obtained by a differentiator to provide a proper phase shift required for oscillation. The signal is multiplied by a gain control signal and fed back through a buffer to drive the resonator. The gain control signal is automatically set by the AAC loop. Inside the AAC loop, the oscillation signal is pre-amplified by A_2 before feeding it to the rectifier to ensure its proper operation. An error amplifier is used to amplify the difference between the detected amplitude and a preset value V_{R0} . To reduce the $1/f$ noise, chopper stabilization is applied to the rectifier and the error amplifier. The resultant error signal is fed to the loop filter $L(s)$ whose output controls the gain of the linear VGA (or multiplier). To operate the whole system under 3.3 V power supply, a driving scheme from [54, 55] is adopted to reject the driving feedthrough by separating the sense and drive operation in the time domain. The same electrodes are reused to maximize the signal.

6.2 Low noise capacitive sense interface

The motion of the resonator causes a sense capacitance variation at a frequency of 135 kHz. This capacitance variation is over-sampled by the sense interface at a rate of 5 MHz to maintain a near-smooth waveform and to minimize the delay introduced. This sense interface is modified from a switched-cap charge integrator, with correlated double sampling (CDS) performed at the amplifier output to remove the offset and flicker noise [54, 55]. Fig. 6.2 depicts the proposed capacitive sense interface circuit and its associated clock timing diagram. An additional gain stage is placed after the switched-cap charge integrator.

The operation of this sense interface involves four phases, namely, *clear*, *autozero*, *sense*, and *drive*. Fig. 6.3 shows the simplified configurations of the sense amplifier in four respective phases. The *clear* phase (Fig. 6.3(a)) resets the input common-mode voltage of the sense interface to V_{icm} to ensure a correct bias point and discharges the capacitors to erase the memory from previous cycle. During the *autozero* phase (Fig. 6.3(b)), the amplifier offset and flicker noise are amplified and stored in C_H and to be subtracted in the subsequent sense phase. The polarization voltage V_p is kept at $2V_{DD}$. During the *sense* phase (Fig. 6.3(c)), V_p transits from $2V_{DD}$ to V_{DD} . A small differential charge that is proportional to C_s is produced and flows onto the integrating capacitor C_i . During the *drive* phase (Fig. 6.3(d)), V_p is reset back to $2V_{DD}$ to improve the voltage-to-force transduction. A fully-differential drive voltage V_d is applied to the same electrodes that connect the sense interface. To avoid overdriving OTA1, a pair of

capacitors C_c is used to isolate the drive signal from the inputs of OTA1 whose inputs are shorted during the *drive* phase.

With CDS, at the end of the *autozero* phase, broadband thermal noise will be sampled onto C_H . The capacitive resolution of this sense block is derived as [56]

$$\overline{C_n^2} \approx (\pi f_{-3dB} T_s - 1) \left(\frac{C_c + C_g}{C_c} \right)^2 \frac{C_T^2 \overline{V_n^2}}{(\Delta V_P)^2} \quad (6.1)$$

where f_{-3dB} is the close-loop -3dB bandwidth, T_s is the length of sensing phase, $C_T = C_s + C_p + C_g + C_i$ is the total capacitance, V_n is the input noise of OTA1, and

V_P is the voltage step applied to the common node of capacitive half-bridge. Eq. (6.1) implies that reducing C_T or increasing the sampling rate helps improve the resolution of the sense interface.

In order to reduce the parasitic capacitance at the input of OTA1, the input common mode feedback (ICMFB) [54, 55] is not employed. This will cause the input common mode voltage to vary in response to the voltage step V_P and hence any mismatch between the parasitic capacitances will appear as an offset at the output. In our design, this offset can be removed by the following differentiator and thus, it is no longer an issue.

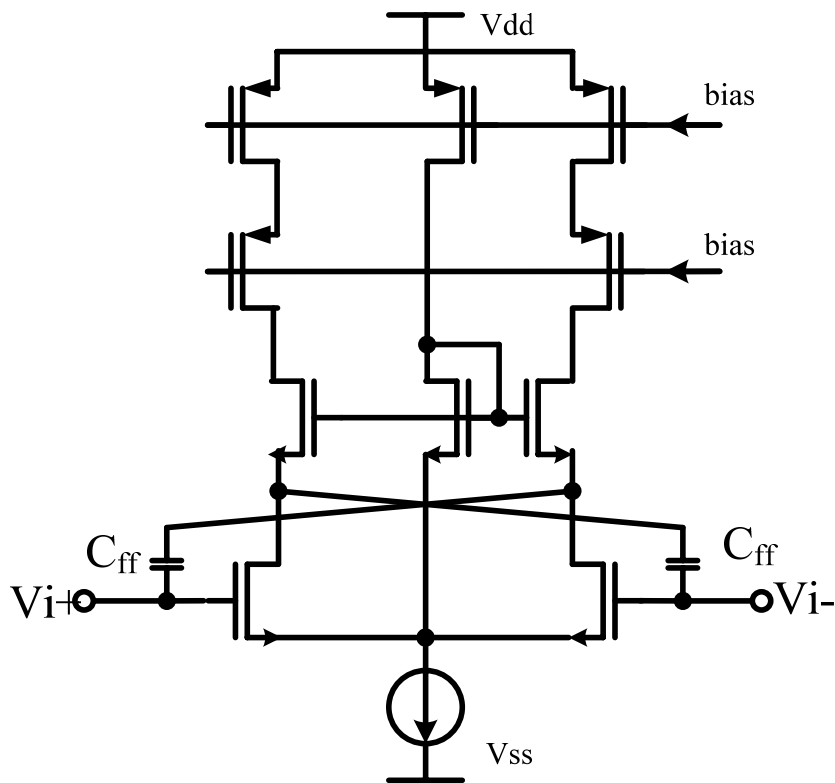


Figure 6.3 Simplified schematic of fast-settling opamp with feedforward path.

The sampling rate is improved by the following techniques. Firstly, two feedforward fast-settling OTAs, OTA1 and OTA2, are designed by introducing a pair of cross-coupling capacitors C_{ff} between the gates and opposite drains of the differential pair [57], as shown in Fig. 6.3. Secondly, a pair of compensation resistors R_c (Fig. 6.2) is introduced in the extra gain stage to optimize its settling time. Thirdly, the reset switches of OTA1 and OTA2 are assigned to different clocks, CLR for OTA1 and $CLRD$ for OTA2, to avoid two-stage settling in the autozero phase, which is identified as the settling bottleneck. CLR is only half of $CLRD$ (Fig. 6.2), which remains high in the whole clear phase. Therefore, at the end of *clear* phase, the error signal in the first stage is already settled and stored

on C_A .

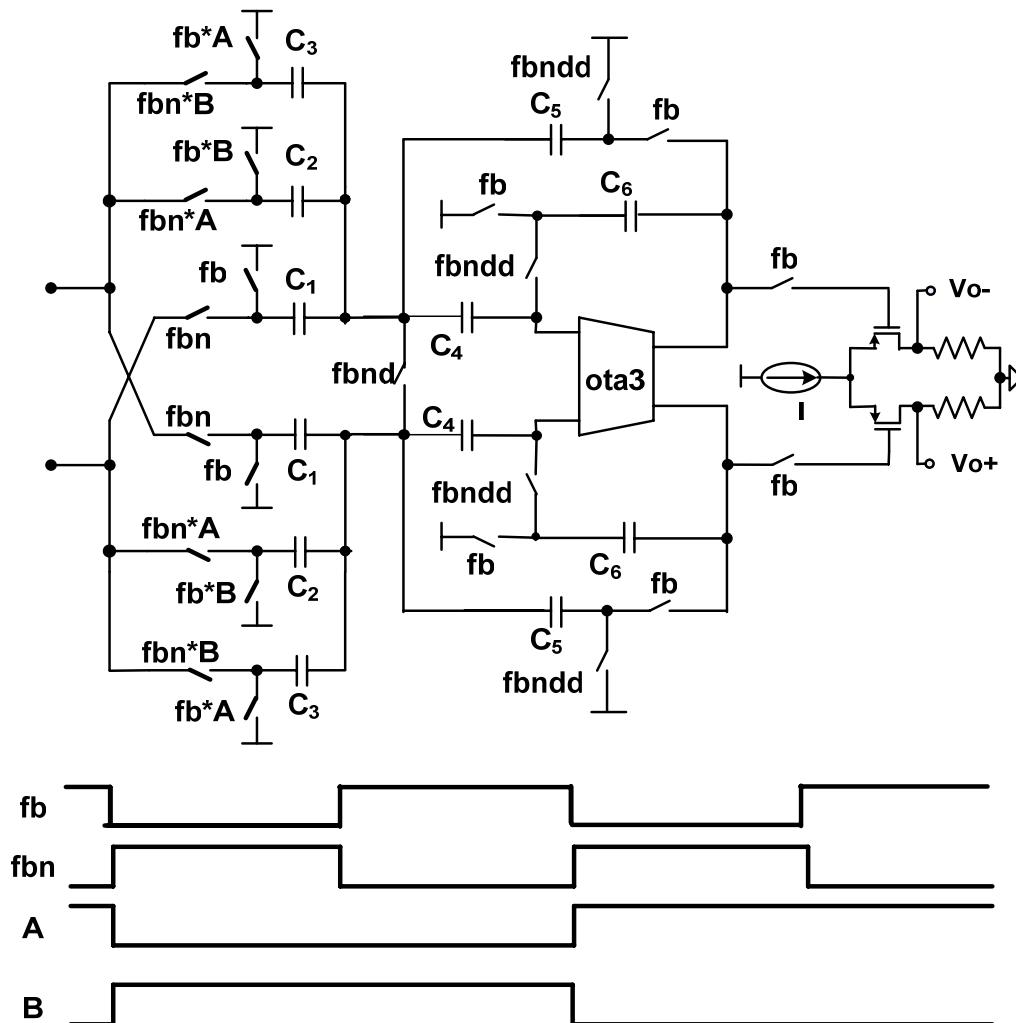


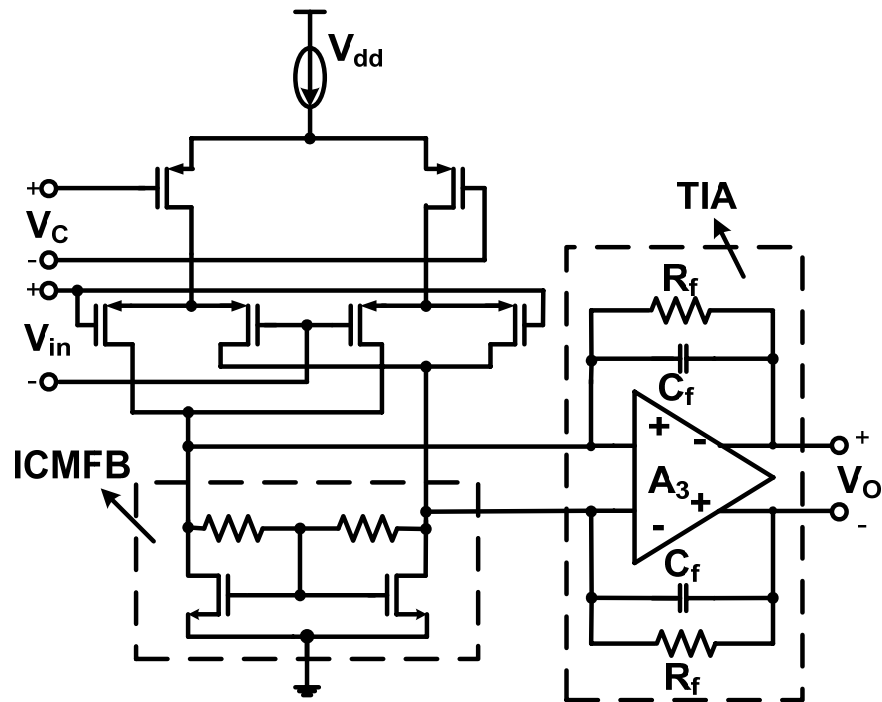
Figure 6.4 (a) Schematic of offset-free differentiator and (b) its associated clock diagram (FBND is delayed version of FBN and FBND is delayed version of FBND).

6.3 Offset-free differentiator

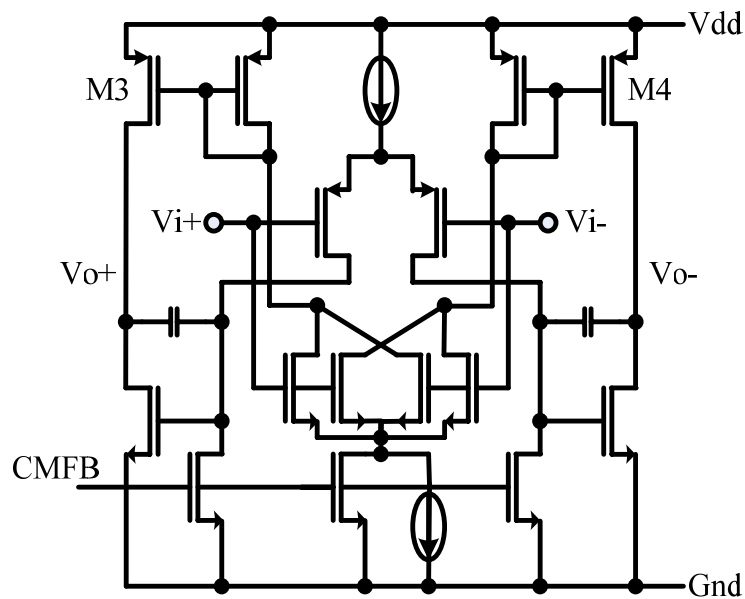
The feedback force should be in phase with the velocity of the resonant

beam to excite self-oscillation. This velocity signal is obtained by differentiating the sensed position signal, C_s , in the z domain. Fig. 6.4 shows the schematic of the differentiator and its clock timing diagram. The differentiation function is realized by charge redistribution among two capacitors. C_1 stores the present signal while C_2 and C_3 alternatively store the delayed signal. The capacitances of C_1 , C_2 , and C_3 are equal. As the signal at the input of the differentiator is still weak, any low frequency noise from OTA3 could jeopardize the signal. Thus, correlated double sampling (CDS) is applied to remove the DC offset and $1/f$ noise at the input of OTA3. During the drive phase, the charges stored on C_1 , C_2 or C_3 are transferred to C_5 and the output becomes valid. During the phase when FBN is high, C_6 holds the output signal from the previous period so that OTA3 remains closed loop. The differentiator stage also provides 4x voltage gain.

The differentiator output is sampled by a pair of switches and held on the input capacitances of a differential pair amplifier.



(a)



(b)

Figure 6.5 Schematic diagram of VGA with transimpedance amplifier as the output buffer.

6.4 Linear VGA and buffer

The linear VGA is essentially a multiplier implemented by a Gilbert cell. Its differential current output is amplified by a trans-impedance amplifier (Fig. 6.5(a)). The common mode output current from the Gilbert cell is subtracted by the input common mode feedback block. Capacitor C_f is introduced in parallel with R_f for phase compensation. This compensation technique allows us to design an op-amp with minimum bandwidth. The TIA has to drive the sense resonator periodically in the presence of parasitic capacitance C_p . Since the output of the TIA drives both the capacitive and resistive loads, a variant of the conventional two-stage Miller amplifier is used, as shown in Fig. 6.5(b). Unlike the conventional two-stage Miller amplifier where the output stage is biased by a constant current, in our modified version, a push-pull output stage is used, which is able to deliver large output current for a large input signal and hence improves the slew rate. A feed-forward path is also introduced in the bottom differential pair to further speed the linear settling.

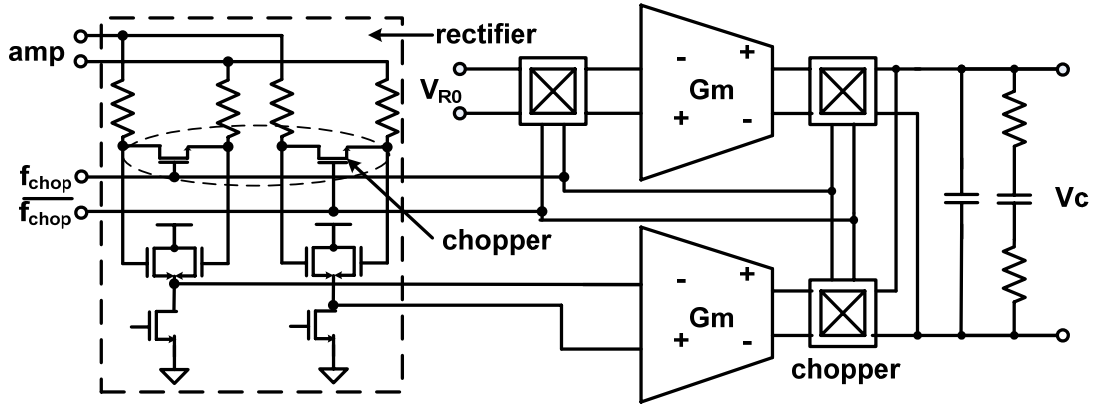


Figure 6.6 Chopper stabilized peak detector and error amplifier.

6.5 CHS peak detector and error amplifier

The AAC loop consists of a rectifier, an error amplifier, and a loop filter. The rectifier is realized using an alternating-voltage-follower (AVF) (Fig. 6.6) for its compatibility to standard CMOS process and its reduced threshold voltage compared with diode based rectifier. However, it suffers from the $1/f$ noise in the tail current. Thus, a chopper stabilization (CHS) is employed in the rectifier to remove the $1/f$ noise. Two sets of AVFs are used, when one is detecting the amplitude, the other acts as a reference to compensate for the voltage shift of source follower. To modulate the input signal, two switches are added at the inputs of the AVFs (Fig. 6.6). These two switches periodically exchange the roles of the rectification and the reference AVFs. This novel CHS is easy to implement and consumes little power compared with CDS.

The comparison between the detected amplitude and the preset value V_{R0} is performed in the current domain through two linearized transconductors, which

convert the output voltage of the rectifier to current. An off-chip RC network provides the necessary poles and zeros for the loop filter $L(s)$. Three sets of chopper are placed around the transconductors to complete the chopper stabilization.

6.6 Chip floorplan and microphotograph

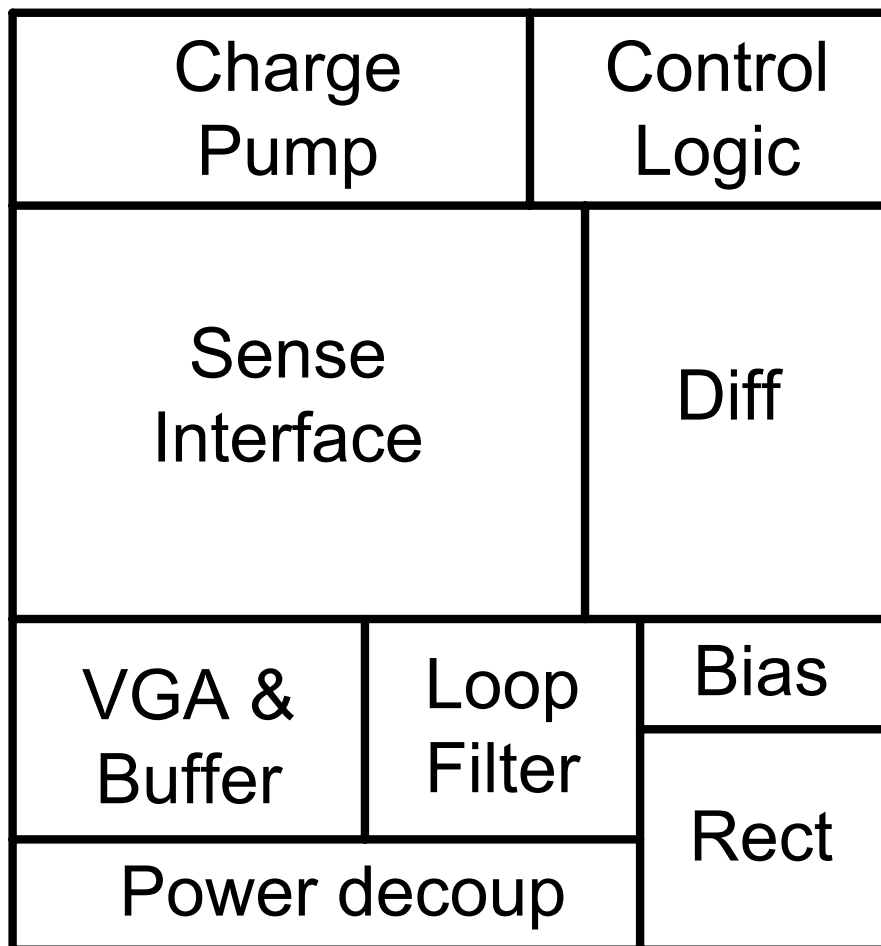


Figure 6.7 Chip floorplan

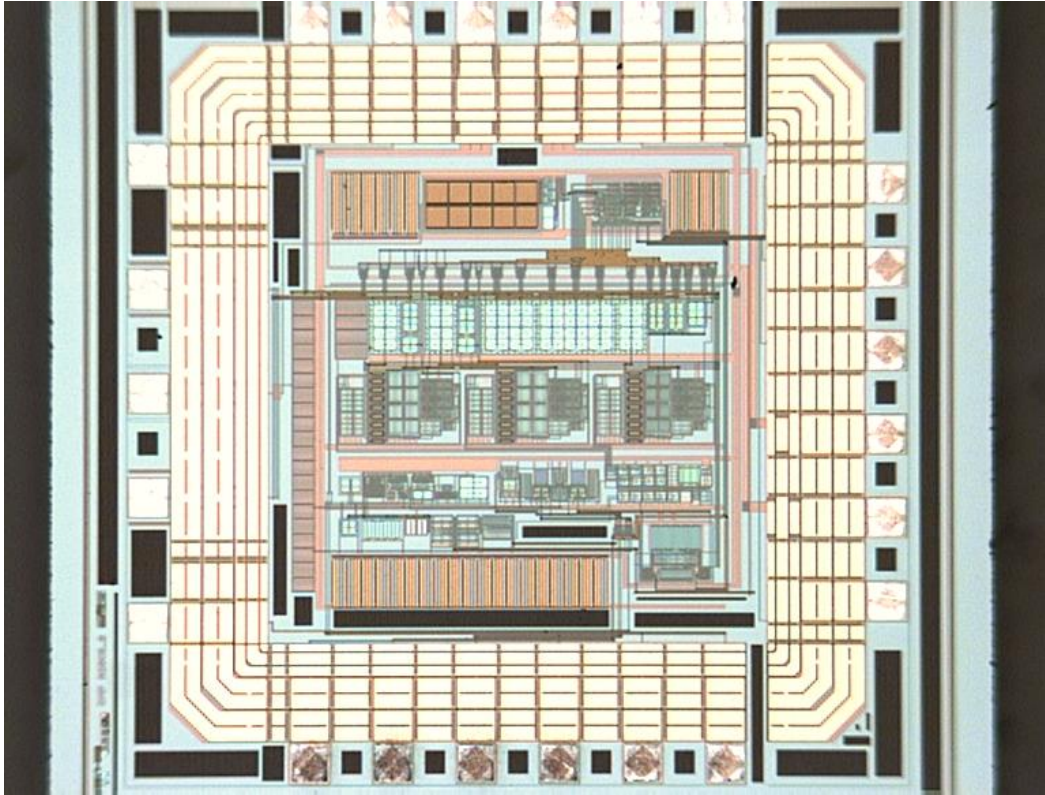


Figure 6.8 Chip microphotograph

Chapter 7 Experimental result

7.1 MEMS oscillator

The readout circuit IC was designed twice based on a 2P4M CMOS 0.35 μm process. In the first run, the circuit chip was characterized with a single sense resonator, whose parameters are given in Table 7.1. They are mounted together on a PCB and interconnected through bond wires, as shown in Fig. 7.1. The PCB is placed in a vacuum chamber. The oscillation amplitude is set to be 0.15 μm by the external voltage V_{R0} , which is already 3 times the bifurcation point. This corresponds to a capacitance variation of 0.5 fF. The resonator has a 113 kHz resonant frequency. The AAC loop bandwidth is set around 100 Hz to attenuate the ripple introduced in the rectifier. The chopping frequency is set to be 2 kHz to facilitate the filter design.



Figure 7.1 Microphotograph of CMOS readout circuit chip and SOI resonator interconnected.

Table 7.1 parameters of the sense resonator

parameters		units	parameters		units
Beam Length	400	$\mu\text{ m}$	Quality Factor	15,000	–
Beam Width	5	$\mu\text{ m}$	Effective Stiffness k_{ef}	274	N/m
Number of Fingers	17	–	Effective Mass m_{ef}	2.18×10^{-9}	kg
Finger Overlap	6	$\mu\text{ m}$	Static overlap Cap C_s	20	fF
Gap	2	$\mu\text{ m}$	Equivalent Cap C_x	1.29×10^{-16}	F
Thickness	25	$\mu\text{ m}$	Equivalent Induc. L_x	6.17×10^4	H
Measured Freq	113.36k	Hz	Equivalent Res. R_x	4.37×10^7	Ω
DC bias voltage	50	V	feedthrough C_{ft}	12	fF

To measure the phase noise with the signal source analyzer available (Agilent E5052A), an off-chip phase-locked-loop (PLL) is built to multiply the oscillation frequency by a factor of 420. The chip design allows us to disable the chopper in the AAC loop and replace the 2nd order AAC loop filter with a 1st order one. The measured phase noises were plotted in Fig. 7.2. The performance improvement by the CHS can be clearly seen.

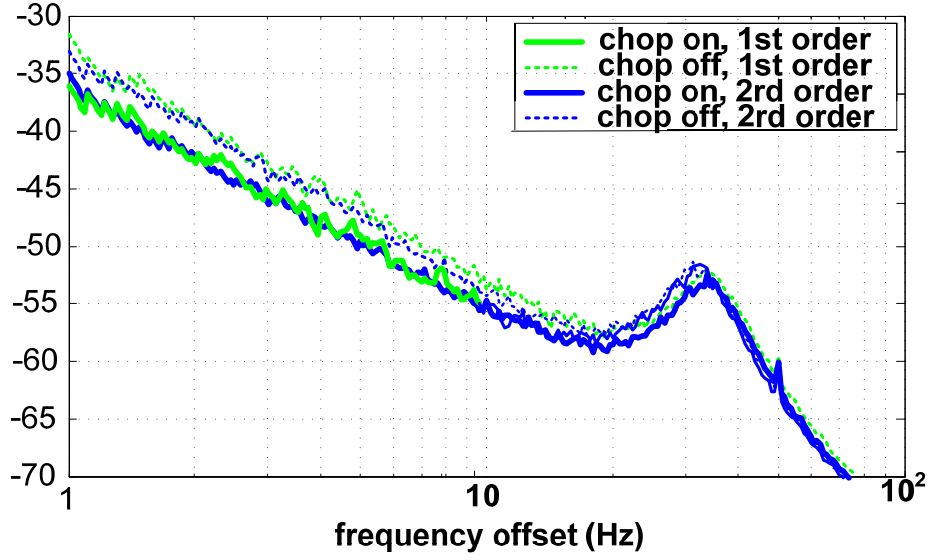


Figure 7.2 The oscillator phase noise deduced from the measured PLL phase noise.

Secondly, the random bias variation was characterized using Allan variance, a method proposed for clock systems [58]. The definition of Allan variance σ is given by

$$\sigma_y^2(\tau) = \frac{1}{2} \langle (y_{n+1} - y_n)^2 \rangle \quad (7.1)$$

where y_n is the average frequency reading over sample period n , and τ is the time span per sample period.

The instant frequency value is read at a rate of 5 Hz with the universal counter Agilent E53131A. Fig. 7.3 shows a sample of measured frequency, from which a slow frequency drift can be observed. This drift is believed to be caused by the temperature drift. To study the random bias variation, the recorded frequency reading was filtered by a 0.5 mHz butterworth high pass filter to

remove the temperature drift. The filtered frequency reading is also plotted in Fig. 7.3.

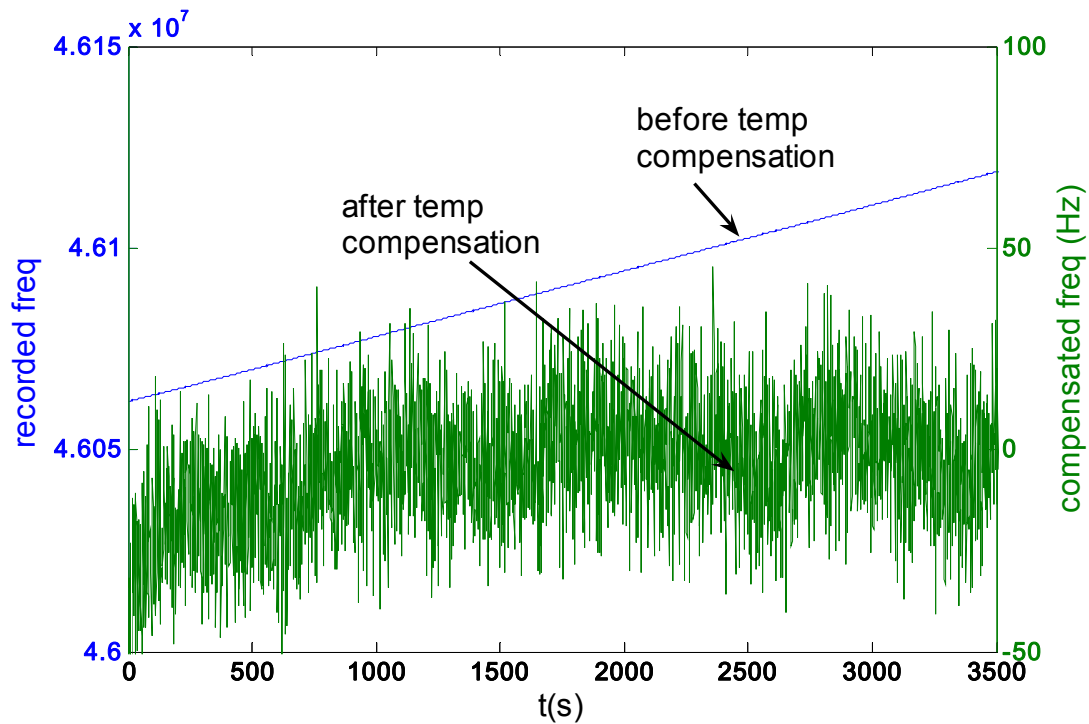


Figure 7.3 A sample of measured frequency at PLL output versus elapsed time and its compensated result.

Allan variance calculation was applied to the filtered frequency reading and plotted in Fig. 7.4. The Allan variance gradually flattens out as the averaging time increases. The floor is known as the Allan deviation, which indicates the random parts of the bias variation. Allan deviation improves from 8 mHz to 3.5 mHz with chopper enabled.

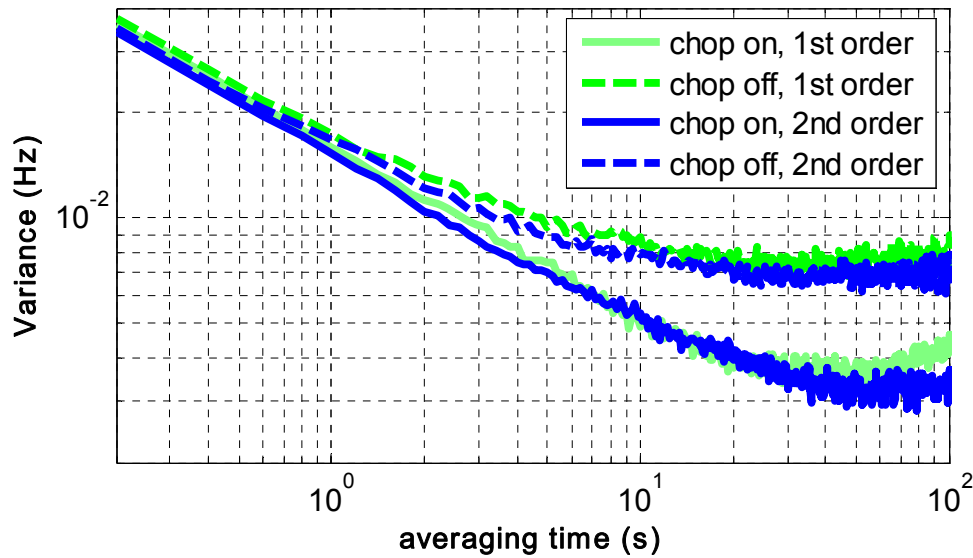


Figure 7.4 Measured Allan Variance.

The residue bias instability could be attributed to the $1/f$ noise in the bias current of the differential pair in Fig. 6.4, which modulate the gain of the differential pair and introduce an additive $1/f$ amplitude noise.

7.2 SOI resonant accelerometer

We designed the second chip which contains two readout channels dedicated to the two sense resonators of an SOI resonant accelerometer. The output signals of the two channels are multiplied with each other with an off-chip multiplier to extract their frequency difference. The multiplier output is low-pass filtered to remove the high frequency components. The complete resonant

To verify that the $1/f$ noise upconversion causes the undesirable bias instability, the bias current in Fig. 6.4 is replaced with a low-noise one in our second chip. The temperature drift is common mode to both of the resonators and is therefore rejected to the first order. Fig. 7.7 plots the Allan variance of the output frequency difference, from which a 3 mHz variance at 1s and a 0.6 mHz floor is observed, which is about 5 times lower than that of the first design by merely replacing the current source in the differential pair.

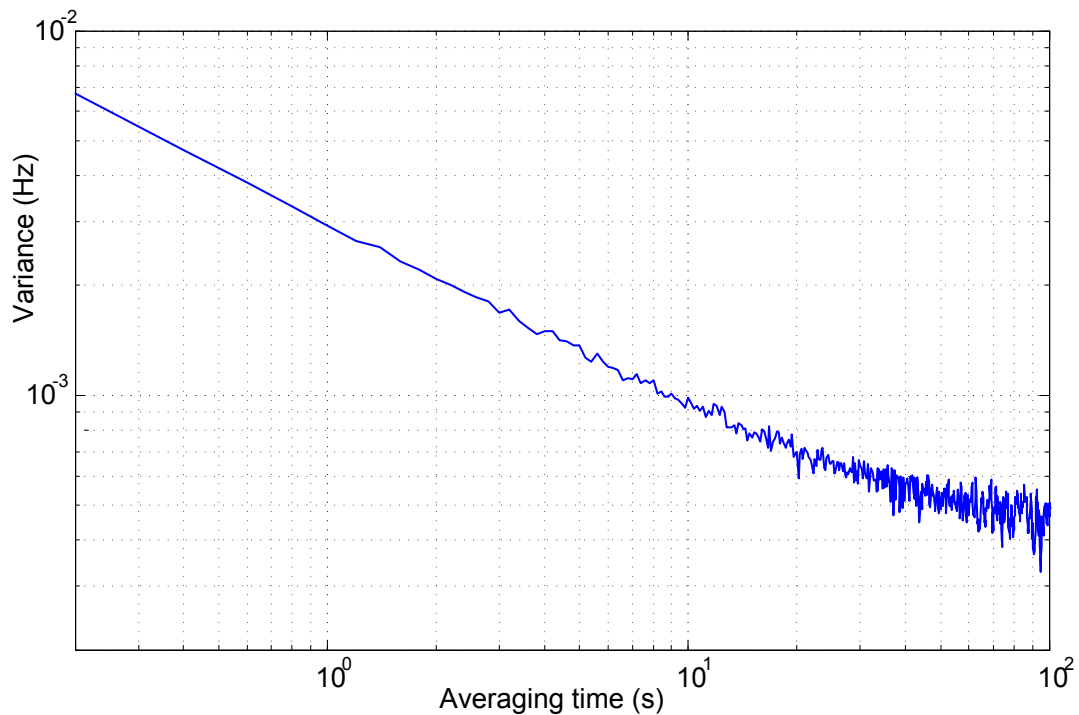


Figure 7.7 The measured Allan variance of the resonant accelerometer.

Due to lack of high precision rotation stage, the sensitivity or the scale factor is characterized by 3 static tests using gravity, that is, 1g, -1g and zero

acceleration. The unloaded frequencies are slightly different from 135 kHz, due to the fabrication error. The result is shown in Fig. 7.8. Based on the measured sensitivity, the measured Allan variance corresponds to $20 \mu\text{g}/\sqrt{\text{Hz}}$ resolution and $4 \mu\text{g}$ bias stability. The $20 \mu\text{g}/\sqrt{\text{Hz}}$ resolution is mainly determined by the noise of differentiator while the bias stability is determined by the $1/f$ noise in the bias current.

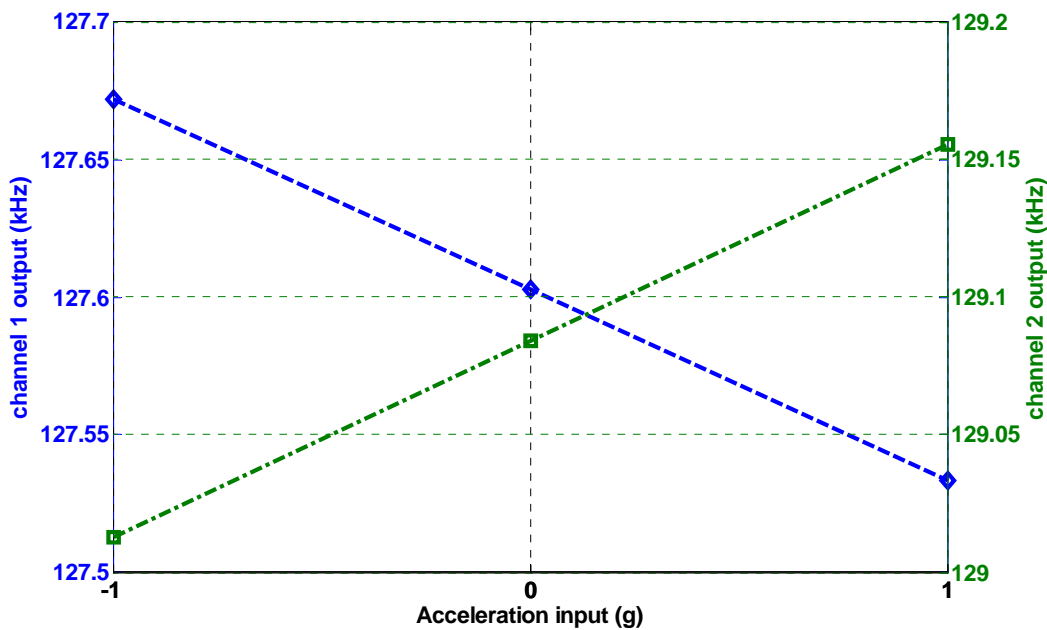


Figure 7.8 Static acceleration testing result.

This work is compared with the previous capacitive accelerometers in Table 7.2 and the previous CMOS readout circuit for SRA in Table 7.3. Although it consumes more power and requires a PLL or high resolution counters for readout, it has a potential to achieve a much higher dynamic range than a conventional capacitive accelerometer.

It seems that the rectifier dominates the noise since other noise sources in total only explain a small portion of the total noise density while the $1/f$ noise in the bias current dominates the bias instability. However, the rectifier noise is mostly caused by the switching behavior, which converts $1/f$ noise into a wide band noise, a mechanism that is not properly modeled in any tools [59], making it hard to predict. Nevertheless, the result highlights the importance of the low noise AAC loop in the design of the high quality MEMS oscillator.

Table 7.2 Comparison of this work with previous capacitive MEMS accelerometer

	Supply	Power	Full range	Noise
[54]	5-V	135-mW	$\pm 0.2g$	$110\mu g/\sqrt{Hz}$
[13]	N.A	N.A	$\pm 13g$	$1m g/\sqrt{Hz}$
[14]	5-V	12-mW	$\pm 1g$	$1.6\mu g/\sqrt{Hz}$
This work	3.3-V	23- mW	$\pm 20g$ (design value)	$20\mu g/\sqrt{Hz}$

Table 7.3 Comparison of this work with previous silicon resonant accelerometer

		Vp	power	noise	Bias stability
[21]	5-V	16-V	N.A	$900\mu g/\sqrt{Hz}$	0.84mg
This work	3.3-V	3.3-6.4V	23mW	$20\mu g/\sqrt{Hz}$	4 μg

Chapter 8 Conclusions and future work

8.1 Conclusion

We proposed a new phase noise model for nonlinear MEMS oscillator employing automatic amplitude control. This model is derived based on state-space theory. According to our analysis, the phase noise is still governed by its linear transfer function, despite of the nonlinearity in the MEMS resonator. The suspicious Duffing behavior is not found in this model, which suggests that even if the MEMS resonator is oscillating far beyond the Duffing bifurcation point, the resultant phase noise should be still governed by linear transfer function. Therefore, to reach the minimum phase noise, the designers are encouraged to maximize the oscillation amplitude, and put more emphasis on the low noise automatic amplitude control loop design so as to minimize the noise aliasing through A-S effect.

Guided by the proposed phase noise model, a prototype MEMS oscillator circuit for silicon resonant accelerometer was demonstrated in this research. The noise inside the oscillation loop was intentionally minimized by a low-noise capacitive sense interface to highlight the importance of the AAC loop. A high-order loop filter borrowed from the PLL design is used to shape the noise at the gain control input of the variable gain amplifier. A novel chopper stabilized (CHS) peak detector and error amplifier is introduced to remove the $1/f$ noise inside the AAC loop and to minimize the phase noise caused by the A-S effect. Combined

with a prototype resonant accelerometer sensor, the circuit achieved 4- μg bias stability and 20- $\mu\text{g}/\sqrt{\text{Hz}}$ resolution. The residue bias instability was found to be caused by the 1/f noise upconversion in the gain stage following the differentiator.

8.2 Future work

We made several assumptions for simplicity in the proposed phase noise model. For example, in this model, the damping is assumed to be viscous. In practice, however, the damping mechanism under high vacuum is dominated by the structural damping arising from viscoelastic strain in the mechanical element, which does not follow a strict linear relationship between damping and the velocity. On the other hand, due to the small size of MEMS devices, absorption-desorption of air atoms may cause additional phase noise around dc. Temperature stability is another possible obstacle to reach higher stability. All of this requires extra work in the modeling.

The analysis of the measurement results suggest that the unexpected residue bias instability was caused by the 1/f upconversion through the open-loop gain stages and the frequency resolution is mainly determined by the noise from the rectifier. The rectifier noise is unknown due to its switching behavior, which converts 1/f noise into a wide band noise. The research into a less noisy AAC loop is therefore a logical next step.

From the power point of view, in this prototype, the sense interface was designed based on the power hungry switched-cap principle. Achieving a better stability

and better resolution at much low power consumption is one of the major challenges in the future work.

References

- [1] T. Gast, "Sensors with oscillating elements," *Journal of Physics E: Scientific Instruments*, Vol. 18, pp. 783-789, 1985.
- [2] T. A. Roessig, "Integrated MEMS tuning fork oscillators for sensor applications," Ph.D. dissertation, Dept. Mechan. Eng., Univ. of California, Berkeley, 1998.
- [3] B. L. Norling, "Precision gravity measurement utilizing accelerex vibrating beam accelerometer technology," in *IEEE Symp. Position Location and Navigation. A Decade of Excellence in the Navigation Sciences*, Las Vegas, NV, Nov. 1990, pp. 509-515.
- [4] W. C. Albert, "Monolithic quartz structure vibrating beam accelerometer (VBA)," in *Proc. IEEE 48th Annu. Symp. Frequency Control*, Boston, MA, May 1994, pp. 415-420.
- [5] T. A. Roessig, R. T. Howe, and A. P. Pisano, "Nonlinear mixing in surface micromachined tuning fork oscillators," in *Proc. IEEE Int. Freq. Control Symp.*, May 1997.
- [6] S. Lee and C. T.-C. Nguyen, "Influence of automatic level control on micromechanical resonator oscillator phase noise," in *Proc. IEEE Int. Freq. Control Symp.*, May 2003, pp. 341-349.
- [7] J. Cao, C.T.-C. Nguyen, "Driving amplitude dependence of micromechanical resonator series motional resistance," *Transducer 99*, pp 1826-1829.

- [8] M. Agarwal et al., "Non-Linearity Cancellation in MEMS Resonators for Improved Power Handling," in *IEEE International Electron Device Meeting (IEDM)*, Tech. Dig., pp. 286-289, Dec. 2005.
- [9] Y.-W. Lin et al., "Series-resonant VHF micromechanical resonator reference oscillators," *IEEE J. Solid-State Circuits*, vol. 39, no. 12, pp. 2477-2491, Dec. 2004.
- [10] V. Kaajakari et al., "Nonlinear limits for single-crystal silicon microresonators," in *J. MEMS*, Vol. 13, No. 5, pp. 715-724, Oct. 2004.
- [11] D.H. Titterton and J.L. Weston, "Strapdown inertial navigation technology," Peter Peregrinus Ltd., 1997.
- [12] C. Lu, M. Lemkin, and B. E. Boser, "A monolithic surface micromachined accelerometer with digital output," in *IEEE J. Solid-State Circuits*, Vol. 30, No. 12, pp. 1367-1373, Dec. 1995.
- [13] H. Luo, et al. "A post-CMOS micromachined lateral accelerometer," in *J. of MEMS*, Vol. 11, No. 3, pp. 188-195, June, 2002.
- [14] J. Chae, H. Kulah, and K. Najafi, "A monolithic three-axis micro-g micromachined silicon capacitive accelerometer," in *J. of MEMS*, Vol. 14, No. 2, pp. 235-242, Apr. 2005.
- [15] N. Yazdi, F. Ayazi, and K. Najafi, "Micromachined inertial sensors," in *Proc. the IEEE*, Vol. 86, No. 8, Aug. 1998.
- [16] L. D. Edmonds, G. M. Swift, and C. I. Lee, "Radiation response of a MEMS accelerometer," in *IEEE Trans. Nuclear Science*, Vol. 45, No. 6, pp. 2779-2788, Dec. 1998.

- [17] M. S. Weinberg, et al., "Temperature compensated oscillating accelerometer with force multiplier," *US patent*, 6269696B1, Aug. 2001.
- [18] M. Helsel et al., "Navigation grade micro-machined silicon accelerometer," in *Proc. IEEE Position Location and Navigation Symp.*, 1994, pp. 51-58.
- [19] D. W. Burns, et al., "Resonant microbeam accelerometers," in *Transducers'95*, June 1995, pp. 656–658.
- [20] R.E. Hopkins et al., "The silicon oscillating accelerometer: a MEMS inertial instrument for strategic missile," in *Proc. Guidance Missile Sciences Conference*, November, 2000, pp. 44-51.
- [21] T. A. Roessig et al., "Surface-micromachined resonant accelerometer," in *Transducers'97*, June 1997, pp. 859-862.
- [22] S. Seok, H. Kim, and K. Chun, "An inertial grade laterally driven MEMS differential resonant accelerometer," in *Proc. IEEE sensors*, Oct. 2004, pp. 654-657.
- [23] D. W. Satchell and J. C. Greenwood, "A thermally-excited silicon accelerometer," *Sensors Actuators*, vol. 17, pp. 241–245, 1989.
- [24] R. T. Howe, S. C. Chang, "Resonant accelerometer," US patent 4805456, Feb. 1989.
- [25] S. C. Chang, M. W. Putty, D. B. Hicks, and C. H. Li, "Resonant bridge two-axis microaccelerometer," *Sensors Actuators*, vol. A21/A23, pp. 342–345, 1990.
- [26] R. Leonardson, S. Foote, "SiMMA™ accelerometer for inertial guidance and navigation," *Proc. IEEE Position Location and Navigation Symposium*, Apr

1998, pp. 152 – 160

- [27] T. V. Roszhart, H. Jerman, J. Drake, and C. de Cotiis, "An inertial-grade micromachined vibrating beam accelerometer," in *Tech. Dig. 8th Int. Conf. Solid-State Sensors and Actuators (Transducers'95)*, June 1995, pp. 656–658
- [28] A.A. Seshia, etc., "A vacuum packaged surface micromachined resonant accelerometer", *Journal of MEMS*, Volume: 11 Issue: 6 , Dec 2002 pp. 784 -793
- [29] B.L. Lee, et al, "A vacuum packaged differential resonant accelerometer using gap sensitive electrostatic stiffness changing effect ", *MEMS 2000*, 23-27 Jan 2000.
- [30] S. Sung, et al. "Development of a tunable resonant accelerometer with self-sustained oscillation loop" *IEEE*, 2000, pp.354-361.
- [31] S. S. Rao, "Mechanical vibrations," 2nd Edition, Addison-Wesley, Reading, MA, 1990.
- [32] W. Weaver Jr., S. Timoshenko, and D. Young, *Vibration Problems in Engineering*, 5th ed. New York: Wiley, 1990.
- [33] M. A. Lemkin, "Micro accelerometer with digital feedback control," PH.D. Dissertation, UC Berkeley, 1997.
- [34] W. A. Clark, "Micromechanical vibratory rate gyroscope," PH.D. Dissertation, UC Berkeley, 1997.
- [35] W. Kuehnel, "Modeling of the mechanical behavior of a differential capacitor acceleration sensor." *Sensors and actuators A*, Vol. A48, May 1995, pp. 101-8.

- [36] W. S. Griffin, et. al., "A study of fluid squeeze film damping," *Journal of Basic Engineering*, June 1966, pp.451-456.
- [37] J. J. Blech, "On Isothermal squeeze films," *Journal of Lubrication Technology*, Vol. 105, pp. 615-620, Oct. 1983.
- [38] J. D. Zook, et al., "Characteristics of polysilicon resonant microbeams," *Sensors and Actuators A*, A35, pp. 51-59, 1992.
- [39] L. Meirovitch, "Analytical Methods in vibrations," Macmillan Publishing Co., Inc. New York, 1967.
- [40] T. C. Nguyen, "Micromechanical signal processor," PH.D. Dissertation, UC Berkeley, Berkeley, CA, 1994.
- [41] Keith Miller, et al. "SOIMUMPs Design Handbook", revision 4.0. K.F. Graff, "Wave Motion in Elastic Solids," Dover, New York, 1991.
- [42] K.F. Graff, "Wave Motion in Elastic Solids," Dover, New York, 1991.
- [43] H. McSkimin, P. Andreatch Jr., "Measurement of third-order moduli of silicon and germanium," *J. Appl. Phys.* 35 (1964) 3312–3319.
- [44] V. Kaajakari, T. Mattila, A. Oja, and H. Seppa, "Nonlinear limit for single crystal silicon microresonators," *J. Microelectromechanical systems*, Vol. 13, No. 5, pp. 715-724, Oct. 2004.
- [45] L. D. Landau and E. M. Lifshitz, *Mechanics*, 3rd ed. Oxford, U.K.: Butterworth-Heinemann, 1999.
- [46] S. S. Bedair¹, G. K. Fedder, "CMOS MEMS oscillator for gas chemical detection," in *Proc. IEEE sensors* Oct. 2004, pp. 955-958.

- [47] J. A. Geen, et al., "Single-Chip Surface Micromachined Integrated Gyroscope With 50°/h Allan Deviation, " in *IEEE J. Solid-State Circuits*, vol. 37, no. 12, pp. 1860-1866, Dec. 2002.
- [48] D. B. Leeson, "A simple model of feedback oscillator noise spectrum," *Proc. IEEE*, pp. 329–330, Feb. 1966.
- [49] B. Razavi, "A Study of Phase Noise in CMOS Oscillators," *JSSC*, pp.331-343, Mar. 1996.
- [50] L. S. Cutler and C. L. Searle, "Some aspects of the theory and measurement of frequency fluctuations in frequency standards," *Proc. IEEE*, vol. 54, pp. 136–154, Feb. 1966.
- [51] Ali Hajimiri, Thomas H. Lee, "A general theory of phase noise in electrical oscillators, "in *IEEE J. Solid-State Circuits*, pp. 179-194, Feb. 1998.
- [52] B. Linares-Barranco and T. Serrano-Gotarredona, "A loss control feedback loop for VCO stable amplitude tuning of RF integrated filters," in *Proc. IEEE International Symposium on Circuits and Systems*, pp.521-524. Aug. 2002.
- [53] F.M. Gardner, "Charge-Pump Phase-Locked Loops," in *IEEE Trans. Comm.*, Vol. COM-28, pp. 1849-1858, Nov. 1980.
- [54] M. Lemkin and B.E. Boser, "A three-axis micromachined accelerometer with a CMOS position-sense interface and digital offset-trim electronics," in *IEEE J. Solid-State Circuits*, vol. 34, pp. 456-468, Apr. 1999.
- [55] X. Jiang, et al, "A Monolithic Surface Micromachined Z-Axis Gyroscope with Digital Output," in *Tech Digest of VLSI Circuit symposium*, 2000, pp 15-18.

- [56] C. C. Enz, G. C. Temes, "Circuit Techniques for Reducing the Effects of Op-Amp Imperfections: Autozeroing, Correlated Double Sampling and Chopper Stabilization," in *Proc. of the IEEE*, vol. 84, no. 11, pp. 1584-1614, November, 1996.
- [57] C. Toumazou and S. Setty, "Feedforward Compensation Techniques for the Design of Low-Voltage OPAMPs and OTAs," in *IEEE, Proc. ISCAS-98*, vol.1, pp. 464-367, May 1998.
- [58] D.W. Allan, "Time and Frequency (Time-Domain) Characterization, Estimation, and Prediction of Precision Clocks and Oscillators," in *IEEE Trans. Ultrasonics, Ferroelectrics, and Frequency Control*, UFFC-34, 647-654, 1987.
- [59] A. P. Wel, et, al., "Low-Frequency Noise Phenomena in Switched MOSFETs," in *IEEE JSSC*, Vol. 42, pp.540-550, March 2007.
- [60] F.X. Kaertner, "Determination of the correlation spectrum of oscillators with low noise," *IEEE Trans. Microw. Theory Tech.*, vol. 37, no. 1, pp. 90-101, Jan. 1989.
- [61] F.X. Kaertner, "Analysis of white and f^{α} noise in oscillators," *Int. J. Circuit Theory Appl.*, vol. 18, pp. 485-519, 1990.
- [62] A. Demir, A. Mehrotra, and J. Roychowdhury, "Phase noise in oscillators: a unifying theory and numerical methods for characterization," *IEEE Trans. Circuits Syst. I, Fundam. Theory Appl.*, vol. 47, no. 5, pp. 655-674, May 2000.
- [63] A. Demir, "Phase noise and timing jitter in oscillators with colored-noise sources," *IEEE Trans. Circuits Syst. I, Fundam. Theory Appl.*, vol. 49, no. 12, pp. 1782-1791, Dec. 2002.

- [64] V. Vasudevan, "A time-domain technique for computation of noise-spectral density in linear and nonlinear time-varying circuits," *IEEE Trans. Circuits Syst. I*, vol. 51, No.2, pp. 422- 433, Feb. 2004.
- [65] B. D. Smedt and G. Gielen, "Accurate simulation of phase noise in oscillators," in *Europun Solid-Sture Circuits Conference*, pp 208-1 1, 1997.
- [66] P. Vanassche, G. Gielen, W. Sansen, "[Efficient analysis of slow-varying oscillator dynamics](#)," *IEEE Trans. Circuits Syst. I*, vol. 51, No.8, pp. 1457-1467, Aug. 2004.

Publication list

Journal:

1. Lin He, Yong Ping Xu, Moorthi Palaniapan, "A CMOS readout circuit for SOI resonant accelerometer with 4- μg bias stability and 20 $\mu\text{g}/\sqrt{\text{Hz}}$ resolution," *IEEE J. Solid-State Circuits*, Vol. 43, No. 6, pp.1480-1490, June 2008.
2. Lin He, Yong Ping Xu, Moorthi Palaniapan, "A state-space phase noise model for nonlinear MEMS oscillators employing automatic amplitude control," *IEEE Trans. on Circ. and Sys.I (to appear)*.

Conference:

1. Lin He, Yong Ping Xu, and Moorthi Palaniapan, "A CMOS readout circuit for silicon resonant accelerometer with 32ppb bias stability," in *Tech. Dig. VLSI Circuits Symp.*, Kyoto, Japan, June 2007, pp. 146-147.
2. Lin He, Yong Ping Xu, Anping Qiu, "Folded silicon resonant accelerometer with temperature compensation," in *Proc. IEEE sensors*, Vienna, Austria, Oct. 2004, pp. 512-515.
3. Lin He, Yong Ping Xu, "Circuit technique to enhance bias stability of silicon resonant accelerometer hybrid-packaged under moderate vacuum," in *Tech. Dig. Eurosensors XVIII*, Rome, Italy, Sep., 2004.

Patents:

1. Lin He, Yong Ping Xu, and Moorthi Palaniapan, "Circuits and methods of automatic amplitude control based on orthogonal envelop detector for MEMS reference oscillator and gyroscope," US Provisional patent, No. 61/096,084.

Appendix

$$[f(y), y]^{-1} = \begin{bmatrix} \dot{x} & x \\ -\frac{k_0}{m}x - \frac{k_1}{m}x^2 - \frac{k_2}{m}x^3 & \dot{x} \end{bmatrix}^{-1}$$

$$= \frac{1}{\dot{x}^2 + (\frac{k_0}{m}x^2 + \frac{k_1}{m}x^3 + \frac{k_2}{m}x^4)} \begin{bmatrix} \dot{x} & -x \\ \frac{k_0}{m}x + \frac{k_1}{m}x^2 + \frac{k_2}{m}x^3 & \dot{x} \end{bmatrix}$$

$$[f(y), 0][f(y), y]^{-1}\xi = f(y)[1, 0][f(y), y]^{-1} \begin{bmatrix} 0 \\ 1 \end{bmatrix} (\Delta\eta\dot{x} + \eta N_{\dot{x}})$$

$$= f(y) \frac{-x}{\dot{x}^2 + (\frac{k_0}{m}x^2 + \frac{k_1}{m}x^3 + \frac{k_2}{m}x^4)} (\Delta\eta\dot{x} + \eta N_{\dot{x}})$$

$$= f(y) \frac{-mx}{m\dot{x}^2 + (k_0x^2 + k_1x^3 + k_2x^4)} (\Delta\eta\dot{x} + \eta N_{\dot{x}})$$

$$= f(y) \frac{-mx}{2E + (k_1x^3/3) + (k_2x^4/2)} (\Delta\eta\dot{x} + \eta N_{\dot{x}})$$

$$[0, y][f(y), y]^{-1}\xi = y[0 \quad 1][f(y), y]^{-1} \begin{bmatrix} 0 \\ 1 \end{bmatrix} (\Delta\eta\dot{x} + \eta N_{\dot{x}})$$

$$= y \frac{\dot{x}}{\dot{x}^2 + (\frac{k_0}{m}x^2 + \frac{k_1}{m}x^3 + \frac{k_2}{m}x^4)} (\Delta\eta\dot{x} + \eta N_{\dot{x}})$$

$$= y \frac{m\dot{x}}{m\dot{x}^2 + (k_0x^2 + k_1x^3 + k_2x^4)} (\Delta\eta\dot{x} + \eta N_{\dot{x}})$$

$$= y \frac{m\dot{x}}{2E + (k_1x^3/3) + (k_2x^4/2)} (\Delta\eta\dot{x} + \eta N_{\dot{x}})$$

Define $E(x) = E + (k_1x^3/6) + (k_2x^4/4)$, we have

$$\begin{aligned}
\xi &= [f(y), 0][f(y), y]^{-1}\xi + [0, y][f(y), y]^{-1}\xi \\
&= f(y)[1 \quad 0][f(y), y]^{-1}\begin{bmatrix} 0 \\ 1 \end{bmatrix}(\Delta\eta\dot{x} + \eta N_{\dot{x}}) \\
&\quad + y[0 \quad 1][f(y), y]^{-1}\begin{bmatrix} 0 \\ 1 \end{bmatrix}(\Delta\eta\dot{x} + \eta N_{\dot{x}}) \\
&= \left[\frac{-mx}{2E + (k_1x^3/3) + (k_2x^4/2)} f(y) \right. \\
&\quad \left. + \frac{m\dot{x}}{2E + (k_1x^3/3) + (k_2x^4/2)} y \right](\Delta\eta\dot{x} + \eta N_{\dot{x}}) \\
&= [\Gamma(y)f(y) + H(y)y](\Delta\eta\dot{x} + \eta N_{\dot{x}})
\end{aligned}$$